Plasma-Surface Interactions in Hollow Cathode Discharges for Electric Propulsion

Thesis by

Angela Maria Capece

In Partial Fulfillment of the Requirements

for the Degree of

Doctor of Philosophy

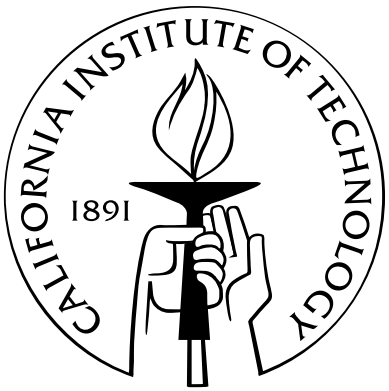

California Institute of Technology

Pasadena, California

2012

(Defended May 14, 2012)

To the student who struggles in the pursuit of knowledge

Acknowledgements

First and foremost I owe my deepest thanks to my advisors, Dr. Jay Polk and Prof. Joe Shepherd, who have provided me with a stimulating and multidisciplinary research project, endless support and encouragement, and much of their valuable time. They had the unfailing ability to believe in me at times when I felt at my lowest, and that has made all the difference. To Joe Shepherd, who very well understands the graduate student condition. His support and understanding were paramount. For the valuable advice he gave me on how to carve out a path in the woods when I felt completely lost in them, I am most indebted. I mark that conversation as the beginning of the end of this work. To Jay Polk, whose friendship and mentoring over the past six years have helped me grow not only as a scientist, but as a person. His ability to listen when I needed someone to talk to and especially when I needed to vent my frustrations is a testament to his extreme patience. I am most thankful for this.

I would like to thank my committee members for all the help they have provided me with throughout the years. To Prof. Paul Bellan, whose passion for plasma physics and approach to teaching it are inspiring. Working through his problem sets made me feel as though I was discovering plasma physics for the first time. The guided "self-discovery" I felt during his course is, in my opinion, the ultimate teaching method, and it had a great impact on me. To Dr. Dan Goebel, whose knowledge of cathodes and ion thrusters is profound. His advice and comments on cathode operation have been immensely helpful, and his ability to rattle off detailed facts, figures, and references at a moment's notice never ceases to impress. To Prof. Kostas Giapis, whose knowledge of ion-surface interactions has helped me considerably. Our conversations have been enlightening.

I would also like to thank Dr. Yiangos Mikellides, whose guidance with the transport model was invaluable. I am thankful for our many discussions about hollow cathode plasmas and numerical methods, and I am always impressed by his intuition in these areas. To Al Owens and Ray Swindlehurst, who have gotten me out of a jam more than once when things went awry in the lab. To Jim Kulleck from JPL and the graduate students in the XPS lab at Caltech, who helped me branch out into the world of materials science.

I extend my thanks to Cheer Los Angeles for welcoming me into their family and providing me with the opportunity to get out of the lab and make a difference in the world. From Cheer LA I

especially want to acknowledge Paul Lee, Kim Indelicato, Brooke Powers Wilson, Diana Ahumada, and Tiffany Deering for their constant support, advice, and wisdom on things beyond the world of science. I have learned much from them. I owe a very special thank you to Brooke Powers Wilson for always being there when I needed someone most and for constantly encouraging me to "face the dragon" throughout this endeavor.

I would also like to acknowledge Phil Boettcher, Leslie Lamberson, Veronica Eliasson, Tony Roy, Chris Kovalchick, Zach Lebo, Ashley Moore, Roseanna Zia, Paul Garry, and Angelo Grubisic for their friendship and support over the years. I extend a special heartfelt thanks to Phil Boettcher for his constant companionship throughout this process, and to Paul Garry for always providing me with mountains and canyons whenever I needed their refuge. To the students in Joe's lab whose humorous takes on grad student life helped lighten many a dark day, and to Remy Mevel for a delicious home-cooked meal that fueled quite a few bits of thesis text.

I would also like to thank my family for their constant love and understanding. To my siblings, Mary, Lisa, Dave, and Julie, with whom I have shared more laughs than with any other four people in the world. And especially to Julie, my littlest sister, who was always willing to play "coffee shop" with me when I came home to visit and needed to work.

I would like to thank the AIAA, the NASA Graduate Student Researchers Fellowship Program, and the JPL Year-Round Internship for funding me during my graduate studies. Finally, I would like to acknowledge all the people whom I never met, yet helped me tremendously with my thesis, including tech support and the multitude of internet forums. Most importantly, I would like to acknowledge all the scientists that came before me whose work has enabled me to tackle this problem. I truly stand on the shoulders of giants.

Abstract

Electric thrusters generate high exhaust velocities and can achieve specific impulses in excess of 1000 s. The low thrust generation and high specific impulse make electric propulsion ideal for interplanetary missions, spacecraft station keeping, and orbit raising maneuvers. Consequently, these devices have been used on a variety of space missions including Deep Space 1, Dawn, and hundreds of commercial spacecraft in Earth orbit. In order to provide the required total impulses, thruster burn time can often exceed 10,000 hours, making thruster lifetime essential.

One of the main life-limiting components on ion engines is the hollow cathode, which serves as the electron source for ionization of the xenon propellant gas. Reactive contaminants such as oxygen can modify the cathode surface morphology and degrade the electron emission properties. Hollow cathodes that operate with reactive impurities in the propellant will experience higher operating temperatures, which increase evaporation of the emission materials and reduce cathode life. A deeper understanding of the mechanisms initiating cathode failure will improve thruster operation, increase lifetime, and ultimately reduce cost.

A significant amount of work has been done previously to understand the effects of oxygen poisoning on vacuum cathodes; however, the xenon plasma adds complexity, and its role during cathode poisoning is not completely understood. The work presented here represents the first attempt at understanding how oxygen impurities in the xenon discharge plasma alter the emitter surface and affect operation of a 4:1:1 BaO-CaO-Al_2O_3 hollow cathode.

A combination of experimentation and modeling was used to investigate how oxygen impurities in the discharge plasma alter the emitter surface and reduce the electron emission capability. The experimental effort involved operating a 4:1:1 hollow cathode at various conditions with oxygen impurities in the xenon flow. Since direct measurements of the emitter surface state cannot be obtained because of the cathode geometry and high particles fluxes, measurements of the emitter temperature using a two-color pyrometer were used to determine the oxygen surface coverage and characterize the rate processes that occur during poisoning.

A model describing the material transport in the plasma discharge was developed and is used to predict the barium and oxygen fluxes to the emitter surface during cathode operation by solving the species continuity and momentum equations. The dominant ionization process for molecular oxygen

in the plasma gas is resonant charge exchange with xenon ions. Barium is effectively recycled in the plasma; however, BaO and O_2 are not. The model shows that the oxygen flux to the surface is not diffusion limited.

Experimental results indicate that the oxygen poisoning rate is slow and that the oxygen poisoning coverage on the emitter surface is less than 3%. A time-dependent model of the reaction kinetics of oxygen and barium at the tungsten surface was developed using the experimental results.

The experiments and kinetics model indicate that the dominant processes at the emitter surface are dissociative adsorption of O_2, sputtering of the O_2 precursor, and desorption of O. Ion sputtering of the weakly bound O_2 precursor state limits the poisoning rate and yields low oxygen coverage. Removal of chemisorbed atomic oxygen is dominated by thermal processes. Based on the low oxygen coverage and long poisoning transients, plasma cathodes appear to be able to withstand higher oxygen concentrations than vacuum cathodes.

Contents

List of Figures

List of Tables

Nomenclature

A	= pre-exponential factor; area, m^2
B	= depletion factor, $\mathrm{m} \cdot \mathrm{s}^{-1/2}$; magnetic field, T
$\bar{c}$	= mean thermal velocity, m/s
c_p	= specific heat capacity, $\mathrm{K} \cdot \mathrm{kg}^{-1} \cdot \mathrm{K}^{-1}$
D	= diffusion coefficient, m^2/s
d	= diameter, m
E	= electric field, N/C; energy, eV
E_b	= surface binding energy, eV
E_d	= desorption energy, eV
E_{th}	= sputtering threshold energy, eV
e	= electron charge, 1.60×10^{-19} J/eV
F_T	= thrust, N
g	= acceleration due to gravity, $9.81\ \mathrm{m/s}^2$
h	= Planck's constant, $6.626 \times 10^{-34}\ \mathrm{J} \cdot \mathrm{s}$
I_{sp}	= specific impulse, s
J_D	= discharge current, A
j	= current density, $\mathrm{A/cm}^2$
j_e	= electron current density, $\mathrm{A/cm}^2$
j_i	= ion current density, $\mathrm{A/cm}^2$
j_{rev}	= reverse electron current density, $\mathrm{A/cm}^2$
k	= Boltzmann constant, 1.38×10^{-23} J/K; thermal conductivity, $\mathrm{W} \cdot \mathrm{m}^{-1} \cdot \mathrm{K}^{-1}$
L	= length, m
m	= mass, kg
m_e	= mass of an electron, 9.11×10^{-31} kg
$\dot{m}$	= mass flow rate, kg/s
N_0	= density of surface sites initially available, m^{-2}
n	= number density, m^{-3}
n_e	= plasma density, m^{-3}
n_n	= neutral density, m^{-3}
P	= pressure, Pa
P_{O_2}	= oxygen partial pressure, Pa
P_v	= vapor pressure, Pa
Q	= scattering cross section, m^2

q = electron charge, 1.60×10^{-19} J/eV

r = radius, m

S = area of the emitting surface, m^2

s_0 = sticking coefficient

T = temperature, K

T_e = electron temperature, eV

T_h, T_p = heavy particle temperature, K

t = time, s

u = velocity, m/s

u_e = propellant exhaust velocity, m/s

V = potential, V; volume, m^3

v_{Bohm} = Bohm velocity, m/s

v_{Th} = thermal velocity, m/s

z = axial distance, m

α_p = polarizability, m^3

β = Richardson-Dushman factor, 120 $A \cdot cm^{-2} \cdot K^{-2}$

Γ = flux, $m^{-2} \cdot s^{-1}$

γ = energy transfer coefficient

δ = barium depletion depth, m

ϵ_a = apparent surface emittance

ϵ_0 = permittivity of free space, 8.854×10^{-12} F/m

ε = electric field, N/C

ζ = mass fraction of impregnant that liberates barium

θ = surface coverage

κ = thermal diffusivity, m^2/s

rate constant, $m^3 \cdot molecule^{-1} \cdot s^{-1}$

λ = wavelength, m

λ_{mfp} = mean free path, m

μ = reduced mass, kg

μ_D = dipole moment, $C \cdot m$

ν = collision frequency, s^{-1}

Π = porosity

ρ = density, kg/m^3

σ = collision diameter, m

σ_{iz} = ionization cross section, m^2

σ_m = momentum transfer cross section, m^2

τ = fraction of pore volume filled with impregnant

Φ = ionization potential, eV

ϕ = work function, eV; plasma potential, V

ϕ_s = Schottky potential, eV

Ω = collision integral

Chapter 1

Introduction

1.1 Electric Propulsion Overview

An electric thruster is any device that accelerates a gas by either electrically heating it or applying electrcomagnetic forces [1,2]. Electric propulsion systems derive energy from external power sources such as RTGs (radioisotope thermoelectric generators), solar panels, and nuclear reactors. This differs from conventional chemical thrusters, in which the energy is supplied by the chemical reaction between the fuel and oxidizer in the combustion chamber. Consequently, electric thrusters are limited by the power capability of the external supply, whereas chemical thrusters are limited by the energy of the reaction.

To understand how power-limited thrusters differ from energy-limited thrusters in terms of performance, first consider the definitions for thrust and specific impulse:

$$F_T = \dot{m} u_e, \tag{1.1.1}$$

$$I_{sp} = \frac{u_e}{g}, \tag{1.1.2}$$

where $\dot{m}$ is the propellant flow rate, u_e is the propellant exhaust velocity, and g is the acceleration due to gravity. For the chemical thruster, assume that all the energy produced during combustion is converted into the kinetic energy of the propellant:

$$\frac{E_{\text{rxn}}}{m} = \frac{u_e^2}{2}. \tag{1.1.3}$$

From Eqs. (1.1.2) and (1.1.3), it is evident that the specific impulse is dependent on the energy output per unit mass, E_{rxn}/m, which is constant for a given chemical reaction. The maximum specific impulse attained in a chemical thruster is approximately 450 s for reactions between hydrogen and oxygen. Although the exhaust velocity and specific impulse are constant in a chemical rocket, the thrust can be changed by altering the propellant flow rate as indicated by Eq. (1.1.1). Chemical

rockets, therefore, have high thrust levels (on the order of kN) and low specific impulse (on the order of 100 s).

Alternatively, since electric thrusters are not energy-limited, they are capable of achieving high specific impulse between 10^3 and 10^4 s, but at relatively low thrust levels (on the order of mN) for power levels between 10^2 and 10^4 W [1]. An expression for the jet kinetic power produced during thruster operation is obtained by multiplying Eq. (1.1.3) by the mass flow rate:

$$P = \frac{\dot{m}u_e^2}{2} = \frac{gF_T I_{sp}}{2}. \tag{1.1.4}$$

For electric thruster operation at constant power, the propellant flow rate can be changed to achieve different exhaust velocities and specific impulses. However, the trade-off for high specific impulse is a reduction in thrust as shown by Eq. (1.1.4). Electric thrusters can operate continuously at low thrust levels, and over long periods of time they can generate very high spacecraft velocities. This makes electric propulsion advantageous for interplanetary missions.

Electric thrusters also have good propellant utilization as a result of the high exhaust velocities they attain [1, 2]. Consider the rocket equation:

$$\frac{m_0}{m_f} = e^{\Delta v/u_e}, \tag{1.1.5}$$

where m_0 is the initial vehicle mass including propellant, and m_f is the burnout mass, which is the sum of the vehicle structure and payload only. For a given mission Δv, an increase in the exhaust velocity is accompanied by a reduction in the mass ratio, meaning that a larger percentage of the total vehicle mass can be dedicated to payload rather than propellant.

As a result of the high specific impulse they can achieve, electric thrusters are used for a variety of space applications such as interplanetary missions, spacecraft station keeping, and orbit raising maneuvers [2]. However, as a result of the low thrust generation, electric thrusters are required to operate in excess of 10,000 h, making thruster life very important. Examples of electric thrusters include resistojets, Hall thrusters, and ion thrusters. Ion thrusters were employed on Deep Space 1, a NASA technology demonstation mission launched in 1998, and Dawn, a NASA mission to study the asteroid Vesta and the dwarf planet Ceres launched in 2007. The focus of the next section will be on the operation of ion thrusters.

1.2 The Ion Thruster

An ion engine creates thrust by electrostatically accelerating ions. To accomplish this, an ion engine must create the plasma, extract and accelerate the ions, and neutralize the positively charged ion beam to prevent spacecraft charging [1]. A schemating drawing of the ion thruster is shown in Fig.

1.2.1. The diagram is axisymmetric about the centerline.

The plasma generator consists of three components: (1) the discharge cathode, which supplies the electrons, (2) the anode, which collects the electrons, and (3) the discharge chamber, which contains the plasma. During thruster operation, neutral propellant gas (typically xenon) is injected into the discharge chamber through the discharge cathode and separate feedlines as shown in Fig. 1.2.1. The cathode emits monoenergetic electrons that enter the discharge chamber and accelerate through the discharge voltage to the anode (i.e., the chamber walls). The discharge cathode is operated in current-controlled mode and is biased negative with respect to the anode by ∼25 V. Ionization of the xenon atoms occurs via electron bombardment in both the discharge cathode and discharge chamber. An external magnetic field is applied to provide electron confinement and increase the electron residence time in the discharge chamber, thereby improving the ionization efficiency [1, 2].

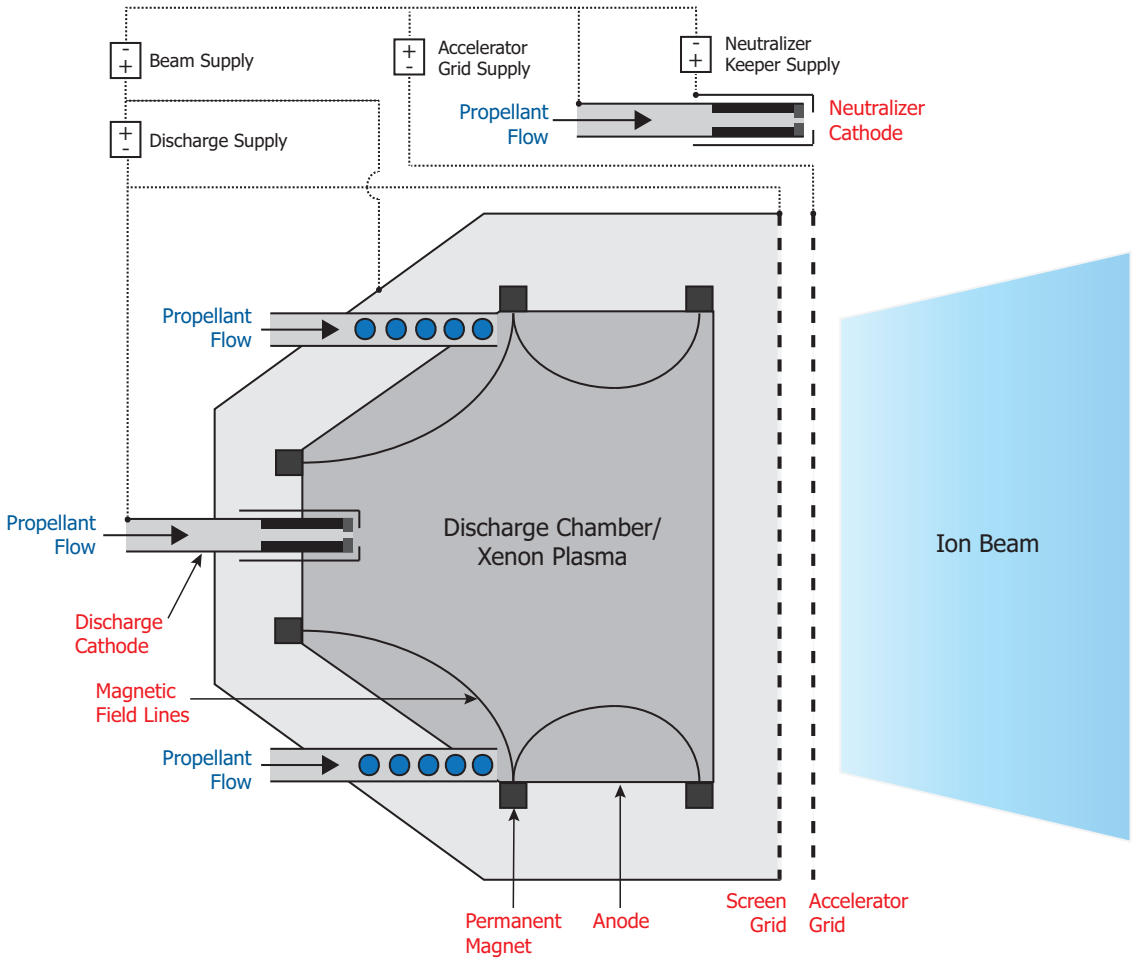

Figure 1.2.1: Ion thruster schematic.

The plasma is at high positive potential (∼1100 V) relative to the space plasma potential at infinity (ground). The ions accelerate through this potential difference and are extracted out of

the discharge chamber through a set of electrically-biased multi-aperature grids, which are referred to as the ion optics or ion accelerator [1]. Ion thrusters typically contain a screen grid and an accelerator grid. The screen grid is electrically tied to the cathode in order to provide electrostatic confinement of the electrons in the discharge chamber. The screen grid aperatures are larger than the accelerator grid aperatures to provide high ion transparency and low neutral transparency [1]. The relative sizing of the holes also allows the screen grid to focus the ions through the accelerator grid aperatures. This aids in minimizing beam divergence, which results in higher thrust values and reduces plume impact on the spacecraft [1].

The neutralizer cathode is external to the thruster and self-biases to produce the required number of electrons to neutralize the beam [2]. The coupling potential is approximately 15 V below ground. Therefore, the accelerator grid is biased negative with respect to ground in order to prevent electrons from backstreaming into the discharge chamber. Energetic electron bombardment can cause vital ion thruster components to overheat. Additionally, large electron currents consume power without providing thrust, thereby lowering the efficiency [1].

1.3 The Hollow Cathode

Cathodes are electron-emitting electrodes and are used in ion engines for propellant ionization and beam neutralization. Electrons are generated via thermionic emission by heating the cathode to emissive temperatures. The electron current density, j, produced during this process is a function of both the surface temperature, T, and the material work function, ϕ, as described by the Richardson-Dushman relation [3]:

$$j = \beta T^2 e^{-e\phi/kT}. \tag{1.3.1}$$

The theoretical constant, β, is defined as

$$\beta \equiv \frac{4\pi m_e q k^2}{h^3}, \tag{1.3.2}$$

where $m_e = 9.11 \times 10^{-31}$ kg is the electron mass, $q = 1.60 \times 10^{-19}$ C is the electron charge, $k = 1.38 \times 10^{-23}$ J/K is Boltzmann's constant, and $h = 6.626 \times 10^{-34}$ J $\cdot$ s is Planck's constant [3]. These values yield $\beta = 120$ A $\cdot$ cm^{-2} $\cdot$ K^{-2}.

Early thrusters initially employed cathodes made of tungsten filaments, which have a work function of 4.5 eV. In order to to achieve an emission current density of 5 A/cm^2 with these filaments, a temperature of 2500°C is required. High heater power on the order of hundreds of Watts is necessary to achieve such high temperatures. Additionally, cathode operation in a plasma environment at these conditions causes erosion due to ion sputtering and rapid evaporation of the tungsten, effectively limiting the lifetime of these cathodes to hundreds of hours. This is problematic because

typical flight cathodes, such as those on Deep Space 1 and Dawn, are required to operate for tens of thousands of hours.

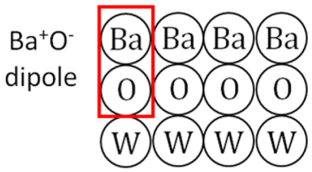

Figure 1.3.1: The $Ba^{+}O^{-}$ dipole reduces the work function to less than 2.1 eV.

In order to improve cathode life, it is crucial to maintain a low temperature for a given electron emission current density. Higher operating temperatures will accelerate evaporation of the tungsten material and will drive reaction rates in the cathode. It has been shown that barium oxide coatings deposited on the tungsten surface reduce the cathode operating temperature. When barium atoms are adsorbed on an oxygen monolayer on top of the tungsten substrate as shown in Fig. 1.3.1, a barium oxide dipole ($Ba^{+}O^{-}$) is formed that reduces the work function to less than 2.1 eV and decreases the temperature to 1100°C for a cathode operating at a current density of 5 A/cm^2 [4]. In order to maintain this low operating temperature, it is important to constantly replenish the tungsten surface with barium oxide at a rate sufficient to balance losses due to evaporation and ion sputtering.

This requirement led to the development of dispenser cathodes, in which porous tungsten material is impregnated with a reservoir of oxide material. The cathode considered in this work is made of porous tungsten containing impregnant material with a 4:1:1 molar ratio of barium oxide (BaO), calcium oxide (CaO), and alumina (Al_2O_3). Barium and barium oxide gases are generated internally via chemical reactions between the tungsten matrix and the impregnant material and then diffuse through the pores to the tungsten surface. The pores provide flow restriction, thus moderating the barium flow to the surface. An SEM image of the porous tungsten insert with 4:1:1 impregnant is shown in Fig. 1.3.2.

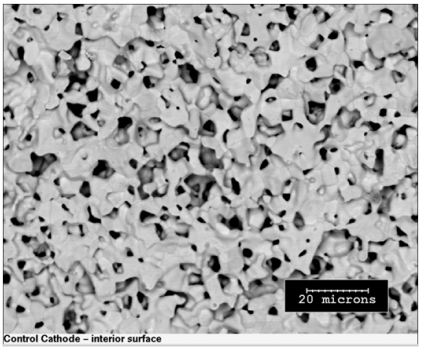

Figure 1.3.2: SEM image of the porous tungsten insert with 4 BaO:1 CaO:1 Al_2O_3 impregnant.

The porous tungsten material is fabricated into a hollow cylinder and is encased in a refractory metal tube typically made of molybdenum-rhenium (Mo-Re). The hollow tungsten cylinder is often referred to as both the "insert" (since it is inserted into the Mo-Re tube) and the "emitter" (since it is the electron source). The entire assembly is often referred to as the cathode. The hollow cathode is preheated using an external resistive heater until the insert reaches the temperature for thermionic emission. A small amount of neutral xenon propellant is injected into the cathode and is ionized via

electron impact creating a xenon plasma. Once the discharge is started, the heater is turned off and the insert is heated by the plasma via ion and/or electron bombardment. An orifice plate is located downstream of the insert and serves to increase the gas pressure inside the hollow cathode. The electrons exit the cathode through the orifice and accelerate toward the anode. Figure 1.3.3 shows a diagram of the hollow cathode configuration.

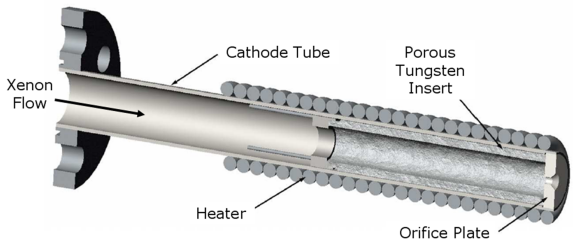

Figure 1.3.3: Diagram of the cathode configuration.

The hollow cathode discharge generates a cold, low-pressure, high-density plasma ($T_e \sim 1$ eV, $P \sim 1$ Torr, $n_e \sim 10^{20}$ m^{-3}) with a cylindrical geometry. The plasma internal to the cathode serves two main purposes: (1) to eliminate the space-charge effects between the cathode and anode surfaces, which helps to maintain the electron emission current density and (2) to heat the insert surface in order to maintain the temperature necessary for thermionic emission. The tubular geometry allows for a more efficient heater design and the addition of radiation shielding, which aids in reducing radiative heat losses. The enclosed design also allows for the redeposition of any tungsten and barium that desorb from the insert surface, helping to maintain the low surface work function.

1.4 Review of Cathode Chemistry

Tungsten cathodes impregnated with barium calcium aluminate compounds were developed by Levi [5,6], and a study of their chemistry began with Rittner, Rutledge, and Ahlert [7–10]. The cathode impregnant composition considered in this work is 4 $BaO \cdot 1\ CaO \cdot 1\ Al_2O_3$. Barium oxide reacts with air and water vapor, and therefore, the purpose of combining BaO with the aluminate is to stabilize it and minimize barium evaporation during impregnation [5, 7]. The addition of CaO lowers the Ba/BaO vapor pressure by forming barium calcium aluminate solid solutions, resulting in a lower barium evaporation rate and improved electron emission properties [7, 11]. This increases cathode life while maintaining a high current density [12].

The ternary phase diagram for the BaO–CaO–Al_2O_3 system at 1250°C has been reproduced here from Lipeles and Kan and is shown in Fig. 1.4.1 [11]. The letters A, B, and C denote Al_2O_3, BaO, and CaO, respectively, and the distance along each of the three edges represents the mole percent of compounds A, B, and C, where the composition at each corner is 100 mol% of the compound corresponding to that corner. Each circle in the diagram corresponds to a different composition with mole ratios given by B:C:A.

The ternary system is divided into smaller triangles, which are ternary systems in themselves, and any point within these subdivisions contains the compounds listed in each corner. For example, in Fig. 1.4.1 the 4:1:1 composition lies within the area bound by lines connecting the corners of B_4A, B, and C, and therefore, the 4:1:1 mixture is comprised of these compounds. It is important to note that as a result of the similar atomic configurations of barium and calcium, the barium oxide in B_4A can be replaced with calcium oxide to give mixed crystals, or solid solutions, i.e., $B_{4-x}C_xA$ [13, 14]. The substitutional solid solution limit of calcium in B_4A is $x = 1.1$, i.e., $Ba_{2.9}Ca_{1.1}Al_2O_7$ [15]. Using conservation of atomic species, the final composition of the 4:1:1 mixture can be found:

$$4\ \mathrm{BaO} + \mathrm{CaO} + \mathrm{Al_2O_3} \rightarrow \mathrm{Ba_{4-x}Ca_xAl_2O_7} + (1-x)\ \mathrm{CaO} + x\ \mathrm{BaO}. \tag{1.4.1}$$

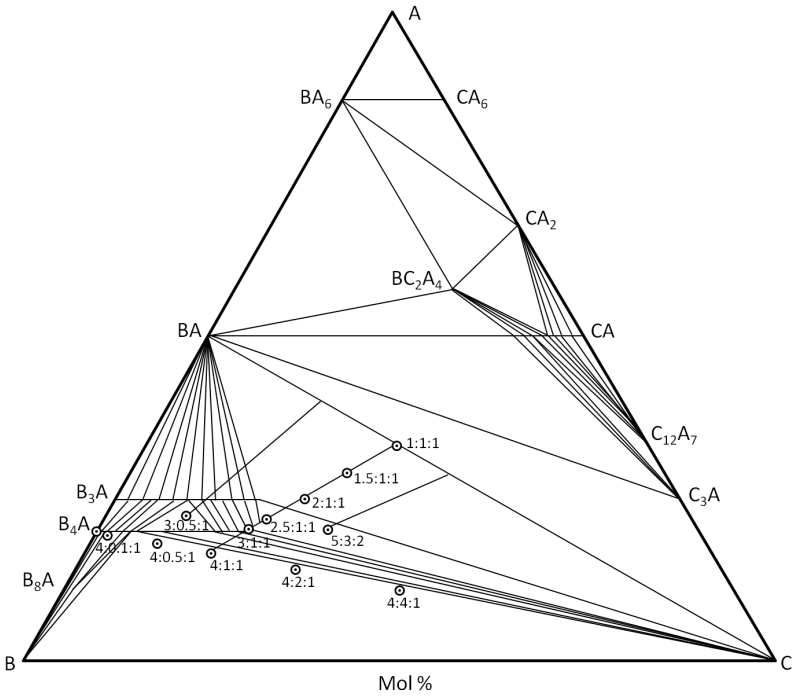

Figure 1.4.1: BaO–CaO–Al_2O_3 phase diagram at 1250°C [11]. B = BaO, C = CaO, A = Al_2O_3. Circles indicate compositions with mole ratios given by B:C:A.

The solid solution decomposes to produce BaO vapor, which is then reduced by the tungsten to produce free barium in the pores via the following reaction [11]:

$$6\ \mathrm{BaO}\ (\mathrm{g}) + \mathrm{W}\ (\mathrm{s}) \rightarrow \mathrm{Ba_3WO_6}\ (\mathrm{s}) + 3\ \mathrm{Ba}\ (\mathrm{g}). \tag{1.4.2}$$

The barium tungstate, Ba_3WO_6, further reduces to produce BaO vapor and another barium tungstate,

$BaWO_4$, according to

$$Ba_3WO_6\ (s) \rightarrow BaWO_4\ (s) + 2\ BaO\ (g). \tag{1.4.3}$$

Equation (1.4.3) is then following by Eq. (1.4.2) and the reduction process is continued [11].

Since BaO evaporates at a faster rate than CaO or $B_{4-x}C_xA$, the impregnant composition will change over time and the point representing the initial composition at 4:1:1 will move along the line toward 1:1:1 [14]. Since the loss of BaO will be greater near the surface, the composition will not be uniform and different phases may exist within the pores [13].

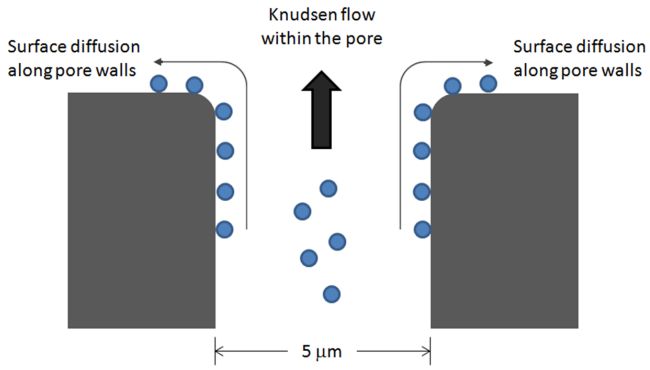

Figure 1.4.2: Ba and BaO are delivered to the surface via Knusdsen flow through the pores and surface diffusion along the pore walls.

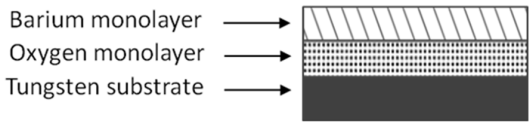

Figure 1.4.3: Tungsten surface with the dipole layer.

The barium pressure in the pores is so low that the mean free path is larger than the pore diameter, and therefore, gaseous barium and barium oxide migrate to the surface by Knudsen flow [9]. A second mechanism for the delivery of barium and barium oxide is surface diffusion along the pore walls. Figure 1.4.2 illustrates these two mechanisms. Once at the emitter surface, the barium diffuses across the tungsten surface thus activating it [8]. Rittner, Ahlert, and Rutledge have measured the electron emission density of these cathodes over the life and have shown that the tungsten surface is covered with a dipole layer, which is comprised of a nearly complete oxygen monolayer covered by a complete barium monolayer as depicted in Fig. 1.4.3, that reduces the tungsten work function [8, 10]. The presence of oxygen on the tungsten surface yields increased barium sticking times and enhanced electron emission [8]. Oxygen losses in the cathode are replenished by barium oxide vapor flow to the surface [8].

Rittner, Ahlert, and Rutledge measured the migration lengths for Ba and BaO diffusion over the

tungsten surface to be between 0.1 and 0.4 mm over cathode temperatures ranging between 1060°C and 1265°C [8]. They determined the activation energy for diffusion to be 0.7 eV and the diffusion coefficient to be $2 - 5 \times 10^{-8}$ cm^2/s over the given temperature range [8]. The cathode emitters considered in this work have pore density on the order of 10^4 pores/mm^2 and a pore diameter of 5 μm [16], which yields a pore separation distance of approximately 10 μm. Since the migration length is large compared with the pore separation, the entire tungsten surface is covered with barium and thus contributes to emission [8]. Note that the pore walls may contribute to emission under certain conditions.

1.5 Hollow Cathode Failure Modes

The lifetime of impregnated tungsten hollow cathodes is ultimately limited by the barium supply to the surface. During life, barium and barium oxide continuously evaporate from the cathode [11]. These species are replenished by the chemical reduction process in Eq. (1.4.2) and transport over the tungsten surface [11]. When the barium supply rate to the surface drops below the value needed to balance desorption losses, the surface coverage of barium decreases and the BaO dipole may no longer be maintained on the tungsten substrate. This results in an increase in both the surface work function and the cathode operating temperature. Termination of life occurs when the work function is too high to sustain the required emission [8]. Cathode failure can occur by three main mechanisms:

1. Exhaustion of the barium supply in the impregnant
2. Transport and deposition of volatile tungsten species
3. Poisoning by reactive gases

During cathode operation, the pores become depleted of barium and the reaction front generating Ba and BaO vapor recedes further into the pores, thus increasing the distance through which these species must flow to reach the surface. As a result, the arrival rate of barium to the surface through the pores will decrease for operation at constant temperature. This is observed as a decay in the barium evaporation rate. Rittner, Rutledge, and Ahlert studied a 5:0:2 vacuum cathode operated at 1190°C and observed a decrease in the barium evaporation rate that scaled with $t^{-1/2}$ for operation up to 2000 h [7]. At 7500 hr, the evaporation rate fell rapidly to zero. This event coincided with emission failure indicating that exhaustion of the barium supply corresponds to end of life.

High operating temperatures accelerate reaction rates in the cathode and increase the barium evaporation rate. Once the barium supply in the impregnant is exhausted, the BaO surface will no longer be replenished and the work function of the surface will increase, making the cathode is impossible to ignite or be heated to the temperatures needed for the required electron current density.

Figure 1.5.1 shows a plot of the end of life for a 4:1:1 vacuum cathode with a tungsten density of 82% [12]. The logarithm of the cathode lifetime drops linearly with operating temperature, making it important to maintain low cathode temperatures.

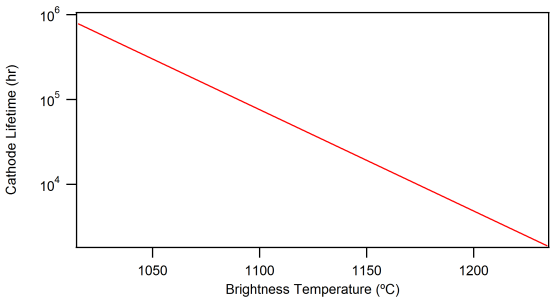

Figure 1.5.1: The effect of operating temperature on cathode lifetime [12].

Transport and deposition of volatile tungsten oxide species have been observed in several extended hollow cathode tests [17–20]. This results in deposits on the emitter surface, blocking the pores and preventing barium from reaching the surface. Deposits on the orifice will reduce the diameter and increase the internal cathode pressure and operating temperature. Polk et al. showed that for plasma cathodes, the barium is replenished to the surface via transport through the gas phase [21]. This transport mechanism can provide barium surface coverages greater than 0.6 in the emission region even if barium production through the pores at that location is inhibited [21]. This process will be discussed in detail in Chapter 3.

Contaminants such as oxygen and water vapor, which may be introduced into the xenon flow via leaks, propellant impurities, and residual chemicals in the feed system, can interact with the cathode substrate and impregnant material, altering the emitter surface structure and cathode chemistry. Excess oxygen in the gas feed system can adsorb on the emitter surface and disturb the $Ba^{+}O^{-}$ dipole, resulting in degradation of the electron emission properties. For cathodes operating at a fixed current density, the operating temperature will then increase and the cathode may become impossible to ignite or incapable of maintaining the required current density. Oxygen poisoning experiments have shown that exposures to high levels of oxygen in excess of hundreds of hours can result in oxidation of the tungsten substrate and the formation of stable barium tungstate surface layers [22]. Several post-test analyses have suggested the presence of barium tungstate ($BaWO_4$), dibarium calcium tungstate (Ba_2CaWO_6), barium oxides, and tungsten oxides on the emitter surface following oxygen exposure [17,20,23]. Thick solid tungstate layers may close off the pores and prevent the release of barium.

Rutledge and Rittner note that an L cathode containing Ba_3WO_6 source material does not reach thermionic emission even though barium is generated according to Eq. (1.4.3) [9]. (The L cathode was developed by H.J. Lemmens of the Philips Research Laboratory and contains a mixture of barium and strontium carbonates in a cavity behind a porous tungsten plug [9, 12, 24].) This result implies that the end of life occurs when the BaO reduction reaction in Eq. (1.4.2) ceases and the reaction in Eq. (1.4.3) becomes the dominant source of barium [9]. The reaction between Ba_3WO_6

and tungsten forms $BaWO_4$, which acts as a poisoning agent [9]. $BaWO_4$ is a stable product and has a high work function given by $\phi = 2.27 + 9.72 \times 10^{-4}T$, where ϕ is in eV and T is in K [25]. For a typical cathode operating temperature of 1400 K, $\phi = 3.63$ eV. Therefore, it will not act as an electron source or provide Ba or BaO to replenish tungsten surfaces in the emitter [26]. $BaWO_4$ and Ba_2CaWO_6 were initially observed in tests with leaky gas systems [17], and were not found on inserts from two long duration tests with carefully controlled gas feed systems [18, 19]. Thus, it appears that excess oxygen in the cathode may accelerate the formation of these layers over long periods of time. To avoid these contaminants, flight systems employ "propellant-grade" xenon with 99.9995% purity; however, the extensive propellant system purification process results in large cost burdens [1].

1.6 Review of Oxygen Poisoning in Vacuum Dispenser Cathodes

Figure 1.6.1 shows the effects of oxygen, water vapor, and air on the emission current for a barium-calcium-aluminate vacuum cathode [27]. The graph shows that the emission current drops rapidly at fixed temperature when the cathode is exposed to these reactive gases at partial pressures that exceed some critical value. Poisoning effects are observed at partial pressures above 10^{-7} Torr for oxygen, 10^{-6} Torr for water vapor, and 3×10^{-6} Torr for air. The graph also indicates that the cathode can tolerate higher partial pressures of these gases at higher cathode operating temperatures. The focus of this work will be on understanding the effects of oxygen poisoning on cathode operation, as the results shown here for vacuum cathodes indicate that the cathode is more sensitive to oxygen contamination than water vapor and air.

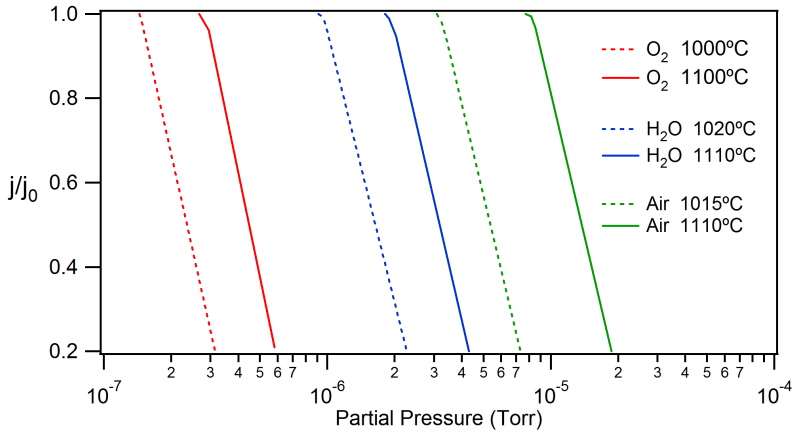

Figure 1.6.1: The effects of reactive gases on emission current for a BaO-CaO-Al_2O_3 cathode [27].

Haas et al. studied the effects of the adsorption of ambient gas residuals on the ignition of shelf-stored vacuum cathodes [28]. Low-energy Auger electron spectroscopy was used to determine the bond type between barium and oxygen on the tungsten surface. Barium oxide is generated by the impregnant during cathode heating and Haas et al. report that BaO appears on the surface at temperatures near 1100 K [28]. At these temperatures, the Ba-O bond breaks, the oxygen atom then attaches itself to the tungsten substrate, and the free barium either desorbs or migrates over the surface and reattaches to an oxygen atom [28]. This process leaves an oxygen-rich surface on top of the tungsten. Haas et al. report that for a vacuum cathode operating at a surface temperature of 1350 K, the barium surface coverage on top of the oxygen monolayer is approximately 90% [29].

Work completed by Shih et al. showed that the binding energy of barium on tungsten is 3.38 eV, whereas the binding energy of barium on tungsten increases to 3.65 eV when the barium is also bound to oxygen [30]. The latter configuration is desirable as it increases the sticking time of the barium on the tungsten surface. Forman independently measured the activation energy for barium desorption to be 4.8 eV from a Ba-O-W surface and approximately 1 eV less from a Ba-W surface [31]. Although a small amount of oxygen in the cathode is desirable, excess oxygen can increase the work function. Haas et al. showed that a 4:1:1 cathode exposed to 10 Langmuirs of O_2 had a work function as high as 2.9 eV [28]. A Langmuir (L) is a unit of exposure that corresponds to 10^{-6} Torr of exposure for 1 second.

Haas et al. adsorbed 10 L of O_2 onto an activated cathode surface and showed via Auger analysis that oxygen atoms adsorb on top of the Ba-O-W surface [29]. The excess oxygen disturbs the Ba-O-W dipole, effectively increasing the work function of the surface. A double layer of oxygen on tungsten results where there is no barium. After exposure, the cathode was then heated to 1180 K and the oxygen was allowed to thermally desorb. At $t = 0$, the surface coverage of oxygen on top of the barium was unity. After 40 s, the surface coverage was reduced to 0.5 [29]. Assuming first order desorption kinetics, $\Gamma_d = Ae^{-eE_d/kT}$, and calculating the pre-exponential factor from transition state theory as $A = kT/h$, a desorption energy of $E_d = 3.55$ eV is determined for oxygen on top of barium [32].

Much work has been done to understand poisoning in vacuum dispenser cathodes at low temperature (i.e., during storage) or at elevated temperatures for short oxygen exposures. The main conclusion that can be drawn from this body of work is that excess oxygen disturbs the BaO dipole on the tungsten surface, thereby increasing the work function.

1.7 Guide to the Thesis

The goal of this work is to understand how oxygen impurities in the xenon discharge plasma alter the emitter surface and affect operation of a 4:1:1 BaO-CaO-Al_2O_3 hollow cathode. A significant amount of work has been done previously to understand the effects of oxygen poisoning on vacuum cathodes; however, the plasma adds complexity, and its role during cathode poisoning is not completely understood. The work presented here represents the first attempt at understanding the plasma-surface interactions during short oxygen exposures in plasma cathodes.

There are two approaches to this problem that may be considered. The first approach involves experimentation with the actual hollow cathode operating under normal conditions. The drawback to this approach is that the cathode geometry and the high particle densities in the plasma prevent direct measurement of the surface state. To circumvent this issue, we may consider an approach that involves model experiments that reproduce the conditions experienced by the cathode during poisoning. During normal operation, the cathode contains a high-density plasma with current densities on the order of 1 A/cm^2 and ion energies less than 15 eV. Such an environment is not easily reproduced in simple model experiments. For example, ion beam experiments may be used to understand how energetic ions interact with an oxygen-covered surface; however, because of space charge limitations, it is not possible to reproduce the particles fluxes and low ion energies in the cathode using these experiments. Additionally, barium recycling has a significant effect on cathode operation, and it would be challenging to implement this process in a simple model experiment.

In consideration of these difficulties, the approach taken in this work involves the use of numerical modeling tools and indirect measurements of the cathode surface state in the proper environment. The hollow cathode was operated at various conditions with oxygen impurities in the xenon flow and temperature measurements were collected along the emitter length using optical pyrometry. A discussion of the experimental set up and results is presented in Chapter 2. Measurements of the emitter temperature and discharge potential were used to extract information regarding the surface state, and a correlation between emitter temperature and oxygen surface coverage was employed using data from the surface science community. The data were then used to characterize the rate processes that occur during oxygen poisoning. These results are presented in Chapter 4.

In vacuum dispenser cathodes, barium and barium oxide are lost during evaporation; however, in plasma discharges, species that desorb from the surface may be ionized in the plasma and transported back to the emitter surface. To understand how the discharge plasma affects recycling of this material, a minor species transport model was developed. The model predicts the barium and oxygen fluxes to the emitter surface during cathode operation by solving the species continuity and momentum equations in a background xenon plasma. A discussion of the model equations, boundary conditions, method of solution, and significant results will be presented in Chapter 3.

A time-dependent model of the adsorption/desorption processes of oxygen and barium on the tungsten surface was developed and is presented in Chapter 4. This model was used with the minor species transport model to give the surface coverage of each species and can be used to explain the cathode response to oxygen impurities. Finally, the major conclusions of this research and suggested future work are discussed in Chapter 5.

Bibliography

[1] D. Goebel and I. Katz, *Fundamentals of Electric Propulsion: Ion and Hall Thrusters*. John Wiley & Sons, 2008.

[2] J. Polk, "Space propulsion," May 2007, Class Lecture. California Institute of Technology.

[3] A. Da Rosa, *Fundamentals of Renewable Energy Processes*. Elsevier, 2009.

[4] P. Palluel and A. M. Schroff, "Experimental study of impregnated-cathode behavior, emission, and life," *J. Appl. Phys.*, vol. 51, no. 5, pp. 2894–2902, 1980.

[5] R. Levi., "New dispenser type thermionic cathode," *J. Appl. Phys.*, vol. 24, p. 233, 1953.

[6] R. Levi, "Improved impregnated cathode," *J. Appl. Phys.*, vol. 26, p. 639, 1955.

[7] E. Rittner, W. Rutledge, and R. Ahlert, "On the mechanism of operation of the barium aluminate impregnated cathode," *J. Appl. Phys.*, vol. 28, no. 12, pp. 1468–1473, 1957.

[8] E. Rittner, R. Ahlert, and W. Rutledge, "Studies on the mechanism of operation of the L cathode. I," *J. Appl. Phys.*, vol. 28, no. 2, pp. 156–166, 1957.

[9] W. Rutledge and E. Rittner, "Studies on the mechanism of operation of the L cathode. II," *J. Appl. Phys.*, vol. 28, no. 2, pp. 167–173, 1957.

[10] E. Rittner, "On the mechanism of operation of the type B impregnated cathode," *J. Appl. Phys.*, vol. 48, no. 10, pp. 4344–4346, 1977.

[11] R. Lipeles and H. Kan, "Chemical stability of barium calcium aluminate dispenser cathode impregnants," *Appl. of Surf. Sci.*, vol. 16, pp. 189–206, 1983.

[12] J. Cronin, "Modern dispenser cathodes," *Proc. IEEE*, vol. 128, no. 1, pp. 19–32, 1981.

[13] M. Coletti and S. Gabriel, "A model for barium oxide depletion from hollow cathode inserts," *IEEE Transactions on Plasma Science*, vol. 37, no. 1, pp. 58–66, 2009.

[14] G. Wolten, "An appraisal of the ternary system BaO–CaO–Al_2O_3," Space Division, Air Force Systems Command, Los Angeles, CA, SD-TR-80-67, 1980.

[15] L. Schoenbeck, "Investigation of reactions between barium compounds and tungsten in a simulated reservoir hollow cathode environment," Ph.D. dissertation, Georgia Institute of Technology, 2005.

[16] S. Kovaleski, "Life model of hollow cathodes using a barium calcium aluminate impregnated tungsten emitter," in *27th International Electric Propulsion Conference*, Pasadena, CA, 2001, IEPC-2001-276.

[17] T. Verhey, "Microanalysis of extended-test xenon hollow cathodes," in *27th AIAA Joint Propulsion Conference*, Sacramento, CA, 1991, AIAA-91-2123.

[18] J. Polk, J. Anderson, J. Brophy, V. Rawlin, M. Patterson, and J. Sovey, "The results of an 8200 hour wear test of the NSTAR ion thruster," in *35th AIAA Joint Propulsion Conference*, Los Angeles, CA, 1999, AIAA-99-2446.

[19] A. Sengupta, "Destructive physical analysis of hollow cathodes from the Deep Space 1 flight spare ion engine 30,000 hr life test," in *29th International Electric Propulsion Conference*, Princeton, NJ, 2005, IEPC-2005-026.

[20] T. Sarver-Verhey, "Destructive evaluation of a xenon hollow cathode after a 28,000 hour life test," in *34rd AIAA Joint Propulsion Conference*, Cleveland, OH, 1998, AIAA-98-3482.

[21] J. Polk, I. Mikellides, I. Katz, and A. Capece, "Tungsten and barium transport in the internal plasma of hollow cathodes," *J. Appl. Phys.*, vol. 105, p. 113301, 2009.

[22] J. Polk, "Long and short term effects of oxygen exposure on hollow cathode operation," in *43rd AIAA Joint Propulsion Conference*, Cincinnati, OH, 2007, AIAA-2007-5191.

[23] J. Brophy and C. Garner, "A 5,000 hour xenon hollow cathode life test," in *27th AIAA Joint Propulsion Conference*, Sacramento, CA, 1991, AIAA-91-2122.

[24] H. Casimir, *Haphazard Reality*. Harper &Row, 1983.

[25] M. Coletti and S. Gabriel, "A model for low work function compound deposition on hollow cathode insert surface," in *46th AIAA Aerospace Sciences Meeting*, Reno, NV, 2008, AIAA-2008-1084.

[26] P. Suitch, "Thermochemical reactions in tungsten-matrix dispenser cathodes impregnated with various barium-calcium-aluminates," Ph.D. dissertation, Georgia Institute of Technology, 1987.

[27] J. Cronin, "Practical aspects of modern dispenser cathodes," *Microwave J.*, vol. 22, pp. 57–62, 1979.

[28] G. Haas, R. Thomas, C. Marrian, and A. Shih, "Rapid turn-on of shelf-stored tubes: An update," *IEEE Transactions on Electron Devices*, vol. 38, no. 10, pp. 2244–2251, 1991.

[29] G. Haas , R. Thomas, C. Marrian, and A. Shih, "Surface characterization of BaO on W, II. Impregnated cathodes," *Appl. Surf. Sci.*, vol. 40, pp. 277–286, 1989.

[30] A. Shih, J. Yater, and R. Abrams, "Thermal desorption of Ba from tungsten," *Appl. Surf. Sci.*, vol. 146, pp. 1–6, 1999.

[31] R. Forman, "Correlation of electron emission with changes in the surface concentration of barium and oxygen on a tungsten surface," *Appl. of Surf. Sci.*, vol. 17, pp. 429–462, 1984.

[32] V. Zhdanov, *Elementary Physicochemical Processes on Solid Surfaces.* Plenum Press, 1991.

Chapter 2

The Effects of Oxygen on Cathode Operation

2.1 Introduction

Cathode poisoning experiments were conducted at the Jet Propulsion Laboratory, California Institute of Technology, under a contract with the National Aeronautics and Space Administration. These experiments have been used for collecting temperature measurements along the cathode emitter surface during operation at various conditions and with oxygen impurities in the xenon flow. These data are used to understand how excess oxygen in the xenon plasma affects cathode operation. The experimental setup along with the methodology and results will be presented here.

2.2 Experimental System

A diagram of the experimental system is shown in Fig. 2.2.1. The cathode is operated with xenon gas and is biased negative with respect to a water-cooled cylindrical anode. A separate feedline is used to inject oxygen into the xenon flow. The emitter temperature is measured with a two-color optical pyrometer and the orifice plate temperature is measured with two type B thermocouples. Further detail on each component and the method of experimental operation will be given in the following sections.

The cathode experiments were conducted under vacuum at a pressure ranging from 10^{-6} to 10^{-5} Torr depending on expellant flow rate. See Table 4.1 for values. The pressure was monitored by an ion gauge calibrated with xenon gas. The vacuum facility was 1 m in diameter and 2 m long, and its pressure was maintained by two CTI-Cryogenics Cryo-Torr 10 High Vacuum Pumps each with a pumping speed of 3000 L/s.

The cathode used in these experiments is of the standard configuration shown in the drawing in Fig. 2.2.2. The cathode tube is made of molybdenum-rhenium and incorporates a tungsten orifice

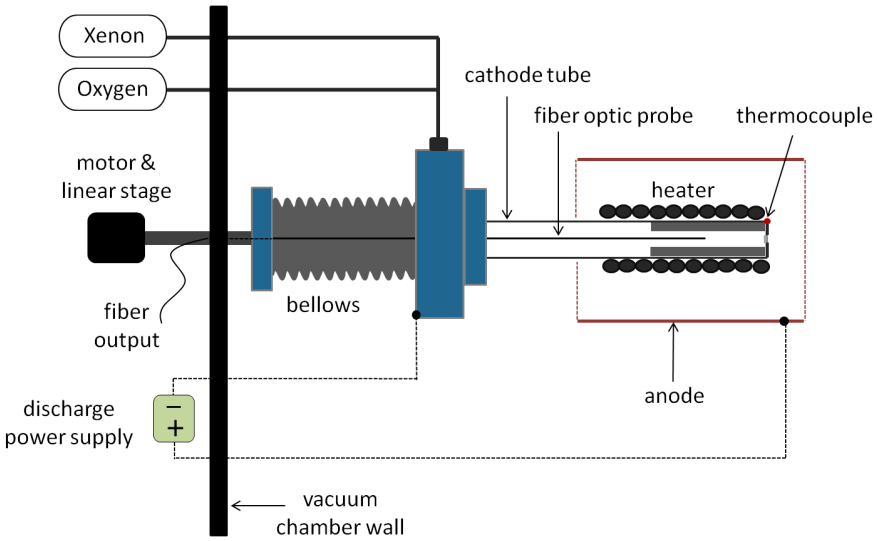

Figure 2.2.1: Schematic of the experimental system.

plate with a 2.25 mm diameter orifice. The cathode houses a porous tungsten electron emitter (also called the insert) impregnated with a 4:1:1 molar ratio of BaO-CaO-Al_2O_3. The insert has a length of 25.4 mm, an inner diameter of 3.81 mm, and an outer diameter of 5.38 mm.

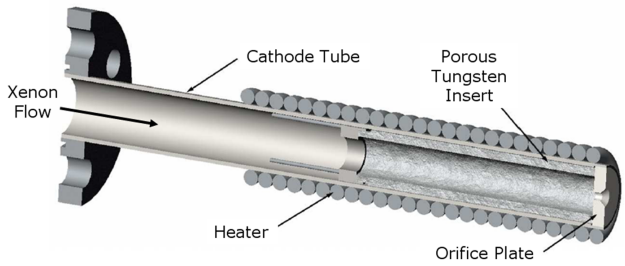

Figure 2.2.2: Sectioned view of the cathode.

A swaged coaxial heater is wrapped around the cathode at the downstream end. Radiation shielding made of tantalum foil is wrapped around the heater coil to improve its efficiency. The heater is used to "condition" the emitter (i.e., bake out any impurities) and preheat it prior to ignition. The cathode conditioning sequence used in this experiment is listed in Table 2.1 [1,2]. The cathode is operated with a water-cooled cylindrical anode, and a water-cooled solenoid surrounding the cathode is used to produce a magnetic field of 80 G at the cathode orifice. The cylindrical anode and applied field improve ionization efficiency and allow the cathode to be operated over the range of flow rates and discharge currents typical for ion or Hall thrusters.

Propellant-grade xenon (99.9995% pure) is used as the cathode expellant. The flow rate is controlled using an MKS 250 controller in combination with a UNIT Model 1661 Metal Z-Seal

thermal mass flow meter and solenoid valve located inside the vacuum chamber. The volumetric flow rate of xenon through the cathode was calibrated using a BIOS Met Lab 500, yielding flow rate measurements with an uncertainty of less than 2%. The calibration curve for the xenon flow rate is shown in Fig. 2.2.3a.

Table 2.1: Cathode Conditioning Sequence

Xe Flow Rate	Heater Current	Duration
3 sccm	3.85 A	180 min
3 sccm	7.20 A	60 min
3 sccm	0 A	10 min

Research grade oxygen (99.999%) at a regulated pressure of up to 100 psia is used as the poisoning gas. The oxygen feed system is designed to control and measure oxygen flow rates ranging from less than 5×10^{-7} to 5×10^{-4} sccm, producing oxygen concentrations in the xenon flow ranging from 0.1 to over 100 parts per million. A fused silica capillary tube 9 m in length with an inner diameter of 20 μm is used as a flow restrictor. The oxygen pressure upstream of the capillary tube is measured using a Baratron 890B pressure transducer.

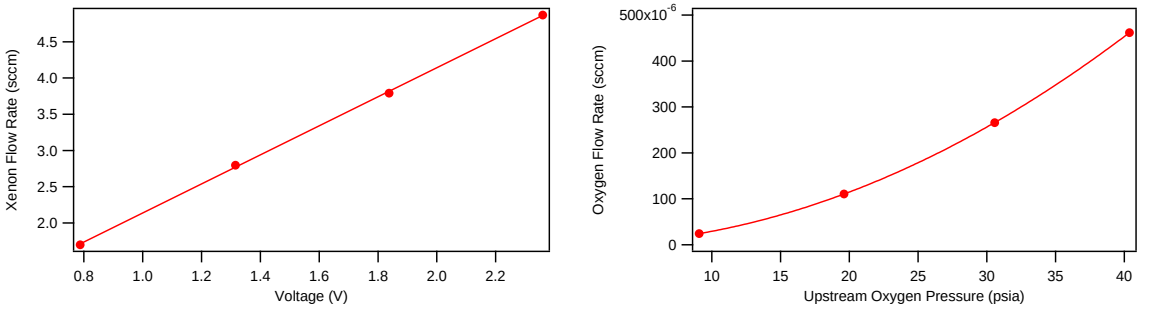

(a) Xenon flow rate calibration curve.

(b) Oxygen calibration curve for the 20 μm capillary.

Figure 2.2.3: Flow rate calibrations for xenon and oxygen.

The flow rate is sensitive to the kinematic viscosity, and therefore, the coiled tube is routed through an enclosure maintained at a constant temperature of 40°C. The volumetric flow rate of oxygen was calibrated by measuring the rate of pressure rise in a known volume using a Baratron 690A Manometer. The calibration volume is contained inside the vacuum chamber to minimize the possibility of air leaks. The calibration curve for the oxygen flow rate versus upstream oxygen pressure is shown in Fig. 2.2.3b.

Three pneumatically actuated valves inside the vacuum chamber are used to vent the calibration volume into the vacuum chamber and to control the flow of oxygen into the manifold and to the cathode. A schematic of the cathode flow system is shown in Fig. 2.2.4. More information on the oxygen flow system is given in Appendix C.

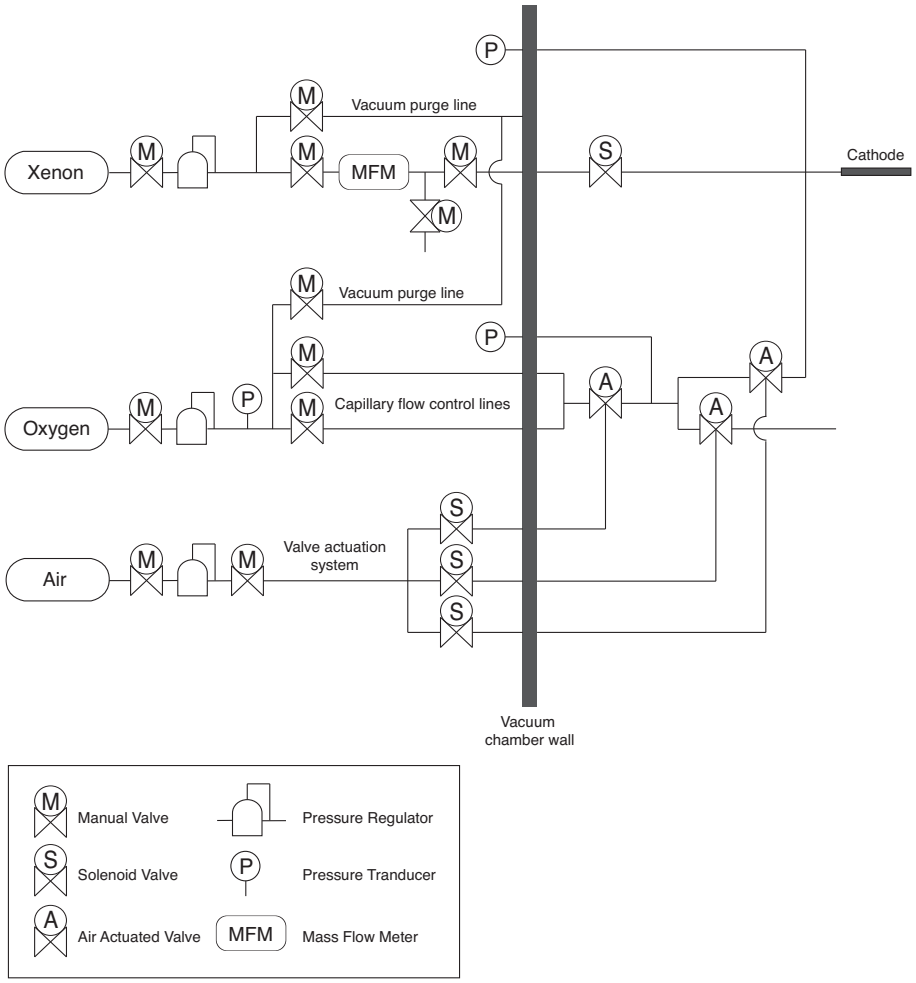

Figure 2.2.4: Schematic of the cathode flow system.

The emitter temperature profile is measured using an optical pyrometer system described in detail by Polk et al. [3]. The use of the optical pyrometer is necessitated because contact measurements on the emitter surface cannot be made as this would disturb the surface state, altering the electron emission. The pyrometer consists of a high-temperature sapphire probe is connected to a fast linear positioning system that enables the probe to scan the length of the emitter in 400 ms at a distance between 0.3 and 1.0 mm from the surface. The probe stops 1.5 mm upstream of the orifice plate and then retracts. The linear positioning system is monitored using a rotary encoder with a resolution of 0.031 mm. Lateral motion of the probe is prevented by the use of two fiber guides. The output from the rotary encoder is used as the timing signal for the data acquisition so that the voltage signal from the probe is coordinated with the motion.

The sapphire probe is 425 μm in diameter and collects light radiated by the cathode emitter surface. One end of the probe is cut and polished at a 45° angle, which rotates the fiber acceptance cone by 90° and collects light from a region that is approximately 2 mm in axial length and 180°

azimuthally. The other end has a standard SubMiniature version A connector and is attached to a flexible fiber optic cable that transmits the light signal to a fiber optic feedthrough. The light is collimated onto a dichroic beam splitter, which transmits wavelengths of 1500 nm with 85% efficiency and reflects wavelengths around 1260 nm with 97% efficiency. The reflected and transmitted beams are filtered using 10 nm bandpass interference filters centered on 1200 and 1500 nm. The beams are then focused onto Hammamatsu InGaAs photodiodes. A picture of the optical system is shown in Fig. 2.2.5.

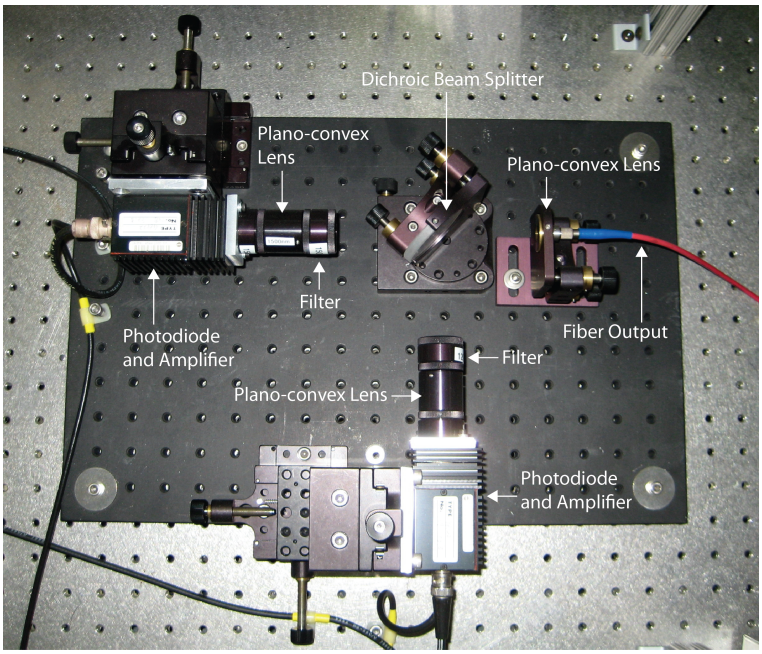

Figure 2.2.5: Optical setup for the two-color pyrometer.

The photodiode voltage signal can be expressed as

$$V_i = \epsilon_a(\lambda_i) A_i(\lambda_i) F_g e^{-B_i/T}, \tag{2.2.1}$$

where ϵ_a is the apparent surface emittance, A_i is a constant that depends on the wavelength, and F_g is the geometric factor, which is a function of the acceptance angle and the distance between the fiber and the surface [3]. By obtaining measurements at two wavelengths and taking the ratio of the voltage signals, the geometric factor, F_g, cancels out. Therefore, the relationship between the voltage ratio and the insert temperature is independent of variations in the distance between the probe and the surface:

$$\frac{V_1}{V_2} = \frac{\epsilon_a(\lambda_1) A_1}{\epsilon_a(\lambda_2) A_2} e^{(B_2 - B_1)/T}, \tag{2.2.2}$$

where $B_2 - B_1 = 2398$ K for the chosen wavelengths [3].

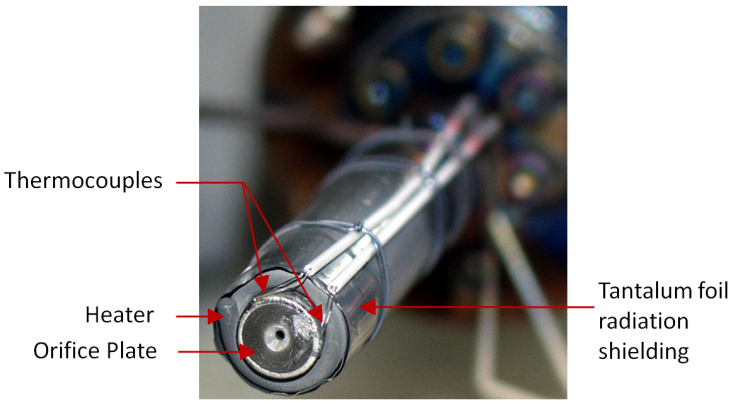

Figure 2.2.6: Cathode assembly used in this experiment.

The optical pyrometer is calibrated prior to ignition using two type B platinum-rhodium thermocouples. Each thermocouple has a diameter of 0.20 mm and is rated for continuous use up to 1704°C in oxidizing or inert atmospheres and under vacuum. The thermocouple leads are insulated with alumina shielding and the junction is then spot welded to the edge of the orifice plate, as shown in Fig. 2.2.6. The cathode heater is operated at currents between 6 and 7 A in order to simulate typical cathode operating temperatures, and a cylindrical tantalum cup made with multi-layer tantalum radiation shields is placed over the cathode to create isothermal conditions along its length. A picture of the cathode assembly and the insulating cup is shown in Fig. 2.2.7.

The probe voltage signal is compared to the thermocouple reading at each heater current set point. Temperature calibration curves are shown in Fig. 2.2.8. The natural logarithm of the ratio of the probe voltage varies linearly with the inverse of the temperature, according to the following relation resulting from Eq. (2.2.2):

$$\ln(V_1/V_2) = \ln[(\epsilon_a(\lambda_1)A_1)/(\epsilon_a(\lambda_2)A_2)] + (B_2 - B_1)/T. \tag{2.2.3}$$

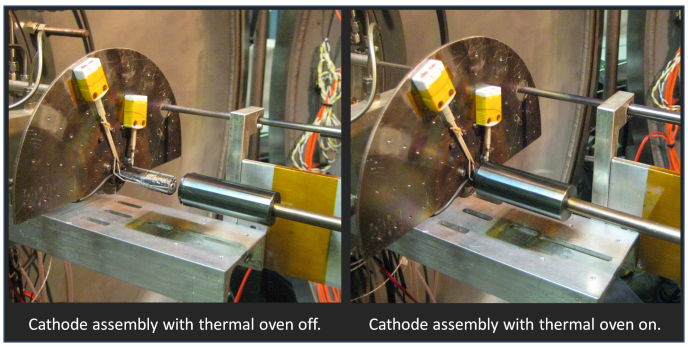

Figure 2.2.7: The cathode assembly and insulating cup.

As the probe becomes contaminated with barium from the cathode, the voltage signals are reduced and the calibration curve shifts. The probe is calibrated often to ensure accurate temperature measurements and is replaced when it becomes too contaminated. The uncertainty in orifice plate temperature measurements is ±1% of the temperature reading. The uncertainty in the emitter temperature measurements, which is based on statistical errors, thermocouple measurement errors in calibration, and uncertainty in the effective emittance of the hollow cathode cavity, is approximately $\pm 12 - 15°C$. However, errors in thermocouple and optical pyrometer measurements are dominated by systematic effects, so the uncertainties in temperature differences are only $\pm 2 - 3°C$ [3].

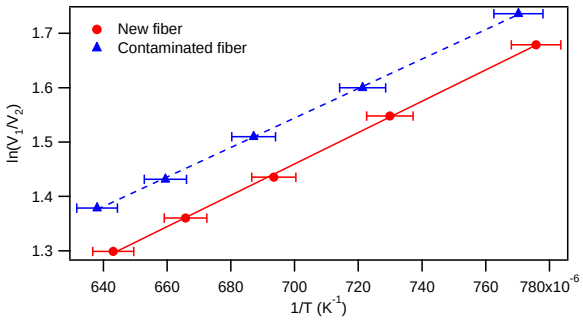

Figure 2.2.8: Temperature calibration curves. The voltage signal is reduced when the probe becomes contaminated and the calibration curve shifts as a result.

An Optomux data system was used with Labview software for set point control and data logging. The data acquisition system records the time, flow rate, tank pressure, discharge current and potential, and cathode heater current and potential. Current and potential are measured to within 1% by the data system using calibrated shunts and voltage dividers.

2.3 Methodology and Results

As discussed in §1.6, the surface temperature was held constant in experiments involving vacuum cathodes and poisoning was indicated by a drop in the emission current density as shown in Fig. 1.6.1. In the experiments presented in this work, however, the temperature was allowed to vary while the discharge current was held constant. The experiments were conducted in this manner as cathodes for electric thrusters are generally operated in current-controlled mode. Poisoning is therefore marked by an increase in temperature, which occurs as the surface work function is increased according to Eq. (1.3.2).

The cathode was operated at discharge currents and xenon flow rates that correspond to the operating conditions of the NASA Solar Electric Propulsion Technology Application Readiness (NSTAR) cathode for comparison purposes [4]. The orifice plate temperature, emitter temperature, and discharge voltage were monitored as oxygen was introduced into the propellant flow at varying concentrations. Thermocouple measurements at the orifice plate were recorded at a rate of one data point per second, while the fiber optic probe measurements of the emitter temperature were taken sparingly in order to prevent probe contamination. Each oxygen exposure lasted no more than four hours. The results of these tests quantify the short term effects caused by oxygen poisoning of the

emitter surface.

Experimental results are displayed in Fig. 2.3.1 for a discharge current 6.0 A and a xenon flow rate of 2.5 sccm. Time is on the abscissa, and the discharge voltage and orifice plate temperature are shown on the ordinate. The oxygen concentration is shown by the bar graph. The bar heights give the level of oxygen concentration, and the bar widths give the duration of the exposure. In this experiment, the cathode is exposed to oxygen concentrations of 1, 10, and 100 ppm.

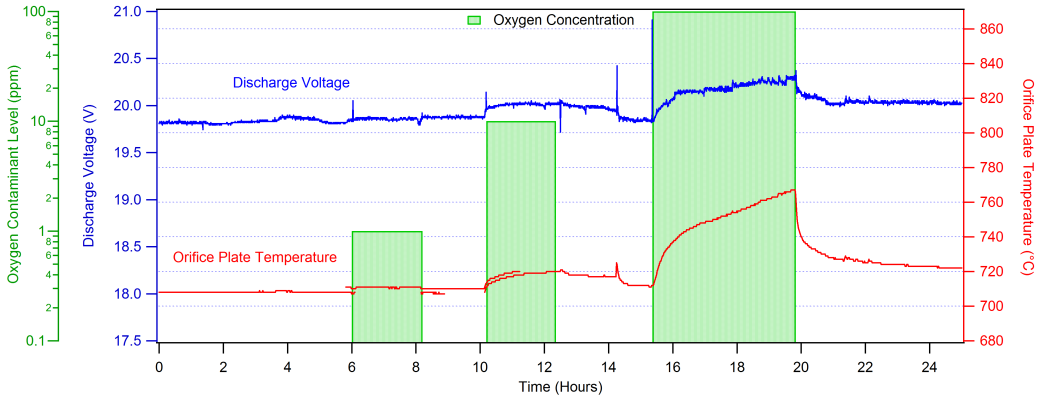

Figure 2.3.1: Results of oxygen poisoning in the cathode at 6.0 A and 2.5 sccm. Orifice plate temperature and discharge voltage increase during exposure to oxygen concentrations of 10 and 100 ppm, but then recover following the exposure.

The temperature and discharge voltage increase when the cathode is exposed to oxygen concentrations of 10 and 100 ppm and then decay when the oxygen flow ceases. This phenomenon is not observed at 1 ppm. The temperature results shown in Fig. 2.3.1 are the thermocouple measurements taken at the orifice plate. Fiber optic temperature measurements of the emitter surface were taken at the start and end of each oxygen exposure. The emitter temperature profiles are shown in Fig. 2.3.2. The blue curves show the temperature profile before the cathode was exposed to oxygen; the red curves show the temperature profile immediately after the oxygen flow was turned off. Typical emitter temperatures for a cathode operated at 6 A of discharge current vary between 1200 and 1325 K depending on the axial location.

The results shown in Fig. 2.3.1 indicate that poisoning begins to occur at at an oxygen concentration between 1 and 10 ppm, corresponding to oxygen partial pressures between 10^{-6} and 10^{-5} Torr. Recall from Fig. 1.6.1 that for vacuum dispenser cathodes at 1000°C, poisoning occurred at oxygen partial pressures as low as 10^{-7} Torr. The results presented here indicate that plasma cathodes may be more resistant to oxygen poisoning than vacuum dispenser cathodes.

Figure 2.3.3 shows the experimental results of poisoning at 100 ppm of oxygen at three different discharge currents: 12, 10, and 6 A. The xenon flow rate at 12 A was set at 3.35 sccm in order to avoid plume mode, which occurs at high discharge currents and low xenon flow rates and results

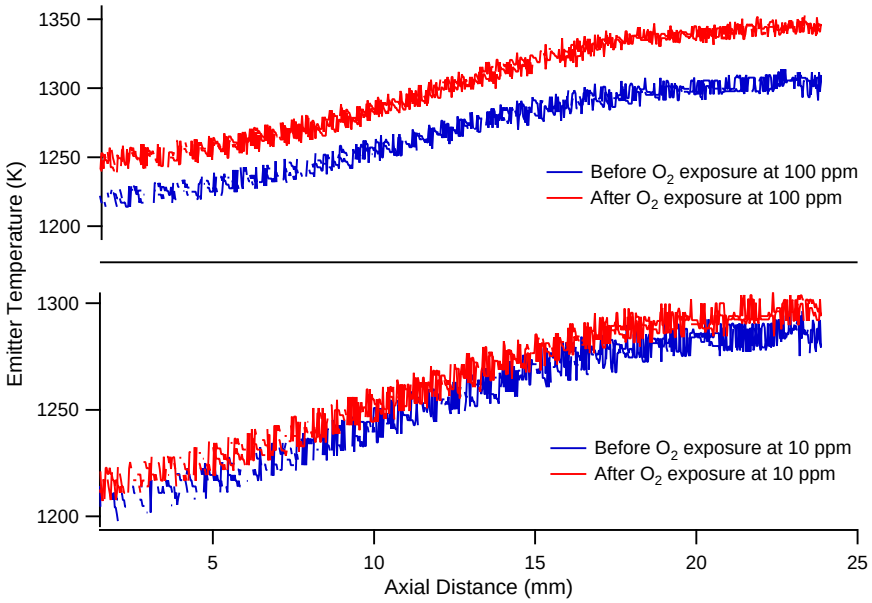

Figure 2.3.2: Temperature profile along the emitter surface before and after poisoning for oxygen concentrations of 10 and 100 ppm.

in high-frequency oscillations in the cathode plume [5]. The 10 and 6 A cases were operated at a xenon flow rate of 2.5 sccm. The oxygen flow rate is 1×10^{-4} lower than the xenon flow rate for an oxygen concentration of 100 ppm. The oxygen exposure began at $t = 0$ and lasted approximately 30 minutes. Note that all three cases exhibit a rise in the temperature during exposure, indicating that poisoning occurs for all discharge currents. Note that in Figs. 2.3.1 and 2.3.3 the cathode temperature decays to a value close to its pre-poisoning value once the oxygen flow is turned off. This indicates that short exposures to oxygen do not permanently damage the cathode.

2.4 Insert Temperature Characterization

Although it is convenient to obtain temperature measurements at the orifice plate using thermocouples, it is the emitter temperature that is of primary interest. However, the fiber optic probe can only withstand approximately 100 scans before needing to be replaced as a result of barium contamination, and therefore, fiber optic temperature measurements of the emitter are taken infrequently. In order to install a new probe, the chamber must be vented and the experimental apparatus disassembled. Once the new probe is installed and aligned, the chamber is placed under vacuum and the cathode must be conditioned again to bake out any impurities resulting from the air exposure. Since this process is time-consuming and interrupts the experiment, it is important to limit the number of probe replacements needed. One way to achieve this is to determine a relationship between the orifice plate temperature and the emitter surface.

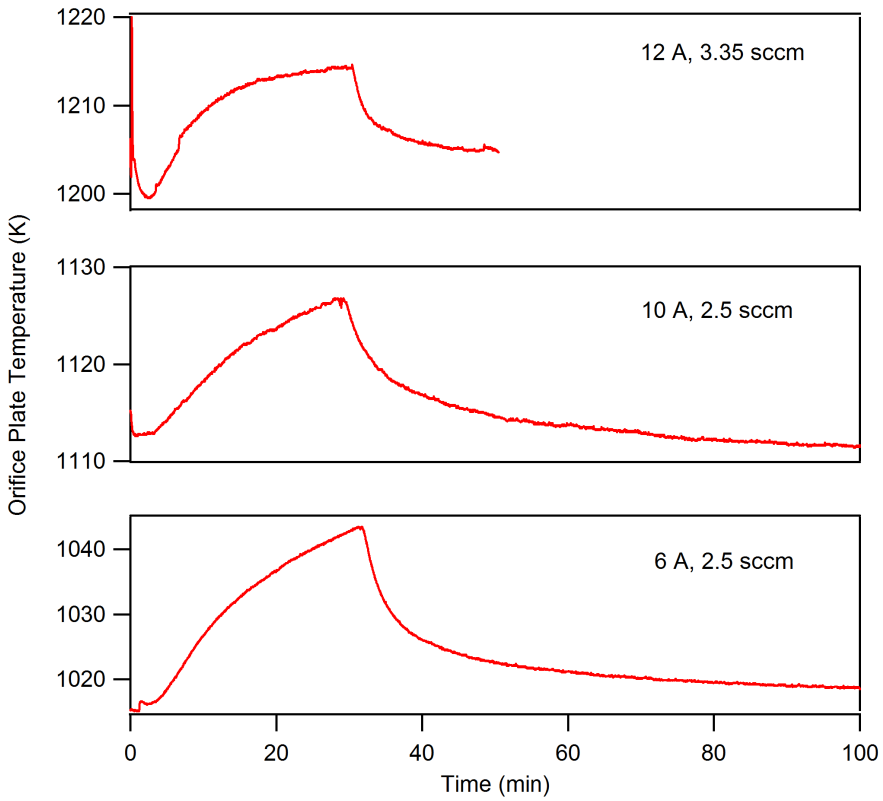

Figure 2.3.3: Results of oxygen poisoning in the cathode at a concentration of 100 ppm for discharge currents of 12, 10, and 6 A. Poisoning is observed at each discharge current.

Figure 2.4.1 shows how the emitter temperature (measured by the fiber optic probe) varies with the orifice plate temperature (measured by the thermocouples) during a poisoning event at a xenon flow rate of 2.5 sccm and discharge currents of 6 and 10 A. The points along the dashed curves are measurements taken during oxygen exposure; the points along the solid curves are measurements taken during the recovery period following oxygen exposure. Note that the temperatures vary linearly with each other. The slope during the recovery period is close to unity; however, the emitter temperature appears to lag behind the orifice plate temperature during poisoning.

From Figs. 2.3.1 and 2.3.3, the temperature rise and decay occur over timescales on the order of several minutes. The time constant for heat conduction along the length of the insert can be calculated from the heat equation as

$$\tau = \frac{L^2}{\kappa}, \tag{2.4.1}$$

where L is the insert length and κ is the thermal diffusivity given by

$$\kappa = \frac{k}{\rho c_p}, \tag{2.4.2}$$

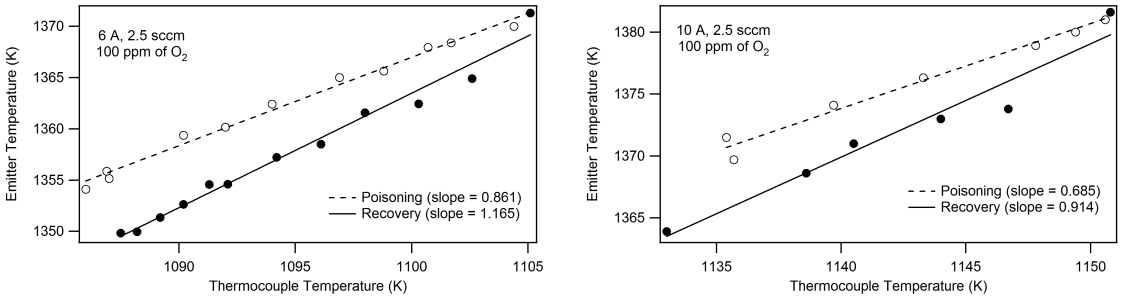

(a) Poisoning at a discharge current of 6 A.

(b) Poisoning at a discharge current of 10 A.

Figure 2.4.1: Comparison between the emitter temperature and the orifice place temperature during poisoning at 6 and 10 A.

where k is the conductivity, ρ is the density, and c_p is the specific heat capacity. Assume the insert is composed of solid tungsten in order to obtain a conservative estimate for the time constant. For tungsten at 1000°C, $\kappa = 0.380$ cm^2/s [6]. Given an insert length of 2.54 cm, the time constant is $\sim$17 s, which is fast compared with the timescale over which the processes of interest occur. The emitter surface temperature can be determined from the orifice plate temperature using the slopes given in Fig. 2.4.1 and the offset, which can be determined by making a measurement of the emitter temperature at the start and conclusion of the oxygen exposure.

The work presented here is for oxygen poisoning over short timescales; however, other studies have been done to understand the effects of long-duration oxygen exposures in excess of several hundred hours [4]. Poisoning over such long exposures may cause the formation of stable tungstate products with poor emission qualities [4]. Tungsten inserts that have been exposed to 100 ppm of oxygen for 480 hours have been examined using energy dispersive spectroscopy (EDS) and a scanning electron microscope (SEM) [4]. Through elemental analysis, these tests have suggested the presence of $BaWO_4$ and Ba_2CaWO_6 on the emitter surface, but it has not been proven conclusively [4]. An alternative to EDS/SEM is x-ray photoelectron spectroscopy (XPS), which is a surface chemical analysis technique that determines elemental composition, chemical state, and electron configuration. An investigation of the XPS spectra of these compounds, which is presented in Appendix A, show that it may be difficult to distinguish between these two species and other barium compounds.

2.5 Conclusions

Poisoning manifests itself as an increase in temperature for cathodes operating at a fixed discharge current. The cathode temperature begins to decay following oxygen exposure, indicating that the changes made to the surface state during poisoning are not permanent. It is important to note that in these experiments the total current is held fixed and not the current density; therefore, it is possible that both the temperature and the emission area may adjust to maintain the current

set point. Most of the electron emission occurs over a region approximately 2 mm wide at the downstream end of the emitter called the emission zone. The area may expand during poisoning to achieve the desired emission.

The effects of poisoning are observed over a range of discharge currents varying between 6 and 12 A. Since an increase in the discharge current is also accompanied by an increase in operating temperature as shown in Fig. 2.3.3, further work must be completed to understand how poisoning is related to the discharge current while keeping temperature constant. This will be discussed in §4.8.

The results presented here show that the cathode is susceptible to poisoning at oxygen concentrations as low as 10 ppm and partial pressures as low as 10^{-6} Torr for emitter temperatures between 930°C and 1050°C. The emitter temperature was shown to vary linearly with the orifice plate temperature, and therefore, the orifice plate temperature may be to used to understand how the emitter surface temperature changes during oxygen exposure. Further experimental work will be motivated in Chapter 4 and presented in §4.5.

Bibliography

[1] "NASA Lewis Research Center Inspection Process Document," NASA Solar Electric Propulsion Technology Applications Readiness (NSTAR) Program, IPD-NSTAR-520, Neutralizer Cathode Assembly Conditioning (01/24/97).

[2] "NASA Lewis Research Center Inspection Process Document," NASA Solar Electric Propulsion Technology Applications Readiness (NSTAR) Program, IPD-NSTAR-525, Discharge Cathode Assembly Conditioning (01/24/97).

[3] J. Polk, C. Marrese-Reading, B. Thornber, L. Dang, L. Johnson, and I. Katz, "Scanning optical pyrometer for measuring temperatures in hollow cathodes," *Rev. Sci. Instrum.*, vol. 78, p. 093101, 2007.

[4] J. Polk, "Long and short term effects of oxygen exposure on hollow cathode operation," in *43rd AIAA Joint Propulsion Conference*, Cincinnati, OH, 2007, AIAA-2007-5191.

[5] D. Goebel and I. Katz, *Fundamentals of Electric Propulsion: Ion and Hall Thrusters.* John Wiley & Sons, 2008.

[6] E. Lassner and W. Schubert, *Tungsten: Properties, Chemistry, Technology of the Element, Alloys, and Chemical Compounds.* Springer, 1999.

Chapter 3

Transport of Barium and Oxygen Species in the Internal Plasma

3.1 Introduction

The xenon discharge plasma is primarily comprised of xenon neutrals, xenon ions, and electrons. However, gas phase barium, oxygen, and tungsten species may also be found in small concentrations. The densities of these minor species are small compared with the plasma and xenon neutral densities, and thus, their presence in the discharge does not significantly alter the xenon plasma parameters. It is important, however, to consider the transport of these minor species as they may deposit on the emitter surface, changing the electron emission properties.

The flow of these particles in the discharge is governed by the conservation equations and interactions with the xenon plasma. Key physical interaction processes include collisions with electrons, xenon ions, and xenon neutrals resulting in momentum transfer, charge exchange, recombination, and ionization. Ionized minor species are also accelerated due to the potential gradients in the plasma. In order to compute the distribution of minor species, the physical interactions and transport processes have been implemented in a numerical simulation of the hollow cathode geometry. The hollow cathode transport model was first developed and presented by Polk et al. to describe the diffusion of barium through the xenon discharge [1–3]. Polk et al. have shown that barium is supplied to the emitter surface through the gas phase and is recycled within the cathode. Barium evaporates from the insert, is ionized in the plasma, and is transported back to the surface via the electric field and xenon ion drag [3]. The barium deposited on the emitter provides enough coverage to sustain the low work function surface even in regions where the pores may be blocked and barium supply from the interior is inhibited. This conclusion is significant as it shows that barium depletion is not as crucial to the lifetime of plasma cathodes as it is to vacuum cathodes.

The goal of the work presented here is to expand the transport model of Polk et al. to include BaO in addition to atomic barium and to model the dynamics during oxygen poisoning. The minor

species considered in this work include: Ba, Ba^+, BaO, BaO^+, O_2, O_2^+, O, and O^+. The conservation equations governing the minor species transport are solved using inputs from a xenon plasma model developed separately by Mikellides et al. [4]. A review of this plasma model will be presented in §3.2. The addition of minor species is assumed to not significantly affect the results of the xenon plasma solution, so that the xenon plasma and minor species transport models may be solved sequentially. The conservation equations describing the minor species transport are presented in §3.3, and the collision processes and selected gas phase reactions are considered in §3.4.

The results of the transport model for normal cathode operation considering only Ba and BaO neutrals and ions are presented in §3.5. Ba and BaO are introduced into the gas via evaporation from the emitter pores, and ions are generated via electron impact ionization. The addition of BaO in the model does not change the Ba solution presented previously by Polk et al. [1]; however, the Ba results are reproduced here for completeness. Once the Ba/BaO solution reaches equilibrium, molecular oxygen is introduced into the discharge to simulate oxygen poisoning. The results of the transport model for oxygen poisoning are presented in §3.6. The transport of tungsten oxide species in the discharge is not modeled as the densities of these species are expected to be small compared with barium and oxygen. A calculation of the desorption rates of seven different tungsten oxide species is presented in Appendix B.

3.2 Review of the Theoretical Model of a Hollow Cathode Plasma

Mikellides et al. have developed a two-dimensional numerical model of the weakly ionized, highly collisional xenon plasma inside the hollow cathode emitter region [4]. Figure 3.2.1 shows the computational mesh, which is 2 cm long, has an inner radius of 0.189 cm, and is axisymmetric about $r = 0$. Although the emitter is 2.54 cm in length, only the downstream 2 cm are modeled as this domain size is sufficient to accurately model the plasma [5]. The xenon plasma model simulates the plasma and neutral gas dynamics in the emitter region by solving a system of eight coupled conservation equations. The xenon neutral gas solution is solved using the full form of the Navier-Stokes equation [6], and the ions and electrons are modeled with species continuity and momentum conservation. The inertia terms were neglected in both the electron and ion momentum equations as it was assumed that no high-frequency phenomena occur and that the dominant processes in the emitter plasma are slow. The model also includes an electron energy equation and a single energy equation for all heavy species under the assumption that the xenon ions and neutrals are in thermal equilibrium. Quasi-neutrality, i.e., $n_e \approx n_i$, single ionization, and classical resistivity were assumed. The dominant transport mechanisms in the plasma are classical collisions between electrons and neutrals, electrons and ions, and ions and neutrals. See Mikellides et al. for the conservation equations

and the functional form of the collision frequencies [4].

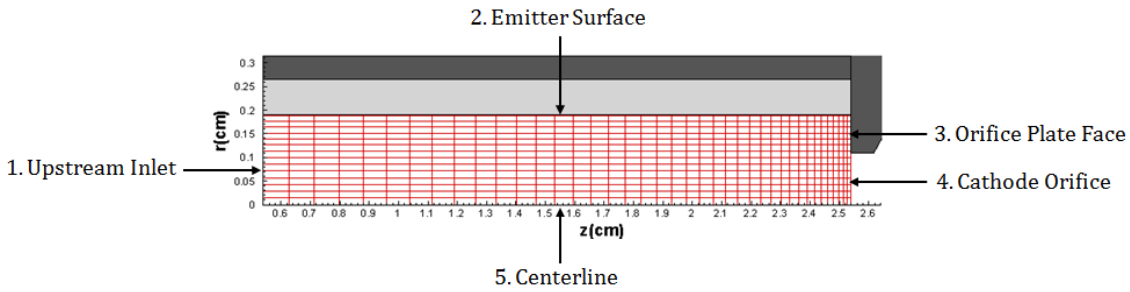

Figure 3.2.1: Computational mesh and boundary surfaces for the xenon plasma model.

The boundary conditions for the emitter surface, orifice plate and conductive walls, orifice entrance, cathode inlet, and symmetry boundary are summarized here. At the emitter surface ($r = 0.189$ cm): the potential is set to zero, the electron current density is given by thermionic emission according to the Richardson equation, electrons with sufficient energy can penetrate the sheath and flow to the walls, ions are assumed to flow into the conducting walls at the Bohm velocity, the electron thermal conduction flux normal to the wall is set to zero, and the heavy species temperature is set equal to the wall temperature, which is determined by measurement. At the orifice plate ($z = 2.54$ cm): zero electron emission is assumed, the potential is set to zero, and the heavy species temperature is set equal to the maximum wall temperature. At the orifice entrance ($z = 2.54$ cm): Dirichlet boundary conditions are used for the plasma particle density and an adiabatic condition is set for the electron temperature. At the cathode inlet ($z = 0$): there is no net electron flux, ions flow out at the ion thermal speed, and the temperature is assumed to be uniform and equal to the value of the emitter temperature at $z = 0$. Symmetry boundary conditions are implemented along the axis of symmetry ($r = 0$).

The five inputs to the numerical model are: (1) the total discharge current, (2) the internal cathode pressure, which is assumed to be uniform, (3) the plasma density at the orifice boundary, which is based on experimental measurements, (4) the plasma potential at the orifice boundary, which is varied during each iteration until the total discharge current is reached, and (5) the emitter temperature as a function of position, which is obtained via optical pyrometry [3, 4].

The conservation equations are discretized using the finite-volume approach. The model yields steady-state values of the plasma density, n_e, electron temperature, T_e, ion current density, j_i, electron current density, j_e, electric field, E, plasma potential, ϕ, heavy particle temperature, T_h, and neutral xenon density, n_n.

The solution to the xenon plasma model for a discharge current of 15 A and a xenon flow rate of 3.7 sccm is shown in Fig. 3.3.1. The cathode generates a cold, high density, low temperature plasma. The neutral density is on the order of 10^{21} m^{-3}, and the heavy particle temperature is

between 1300 and 1750 K. Typical electron temperatures are between 1.6 and 2.2 eV, the plasma potential is as high as 10 V, and the plasma density is on the order of 10^{20} m^{-3} in the emission region.

Xenon neutral density contours and streamlines are shown in Fig. 3.3.1a. Neutral xenon enters the cathode upstream and accelerates through the orifice. The density decreases near the downstream end of the computational region as neutrals exit through the orifice or become ionized.

Most of the ionization occurs in regions where electron temperatures are highest. Figure 3.3.1b shows the electron temperatures and electron current streamlines. Electrons are emitted thermionically from a region along the insert surface approximately 10 mm long and escape through the orifice. Some electrons are able to reach the insert further upstream in regions where the plasma potential is lower. Figure 3.3.1c shows plasma potential contours and ion current streamlines.

High plasma densities occur between $z = 1.9$ and 2.2 cm as shown in Fig. 3.3.1d. Ions flow radially out of this region and either strike the insert surface or escape through the orifice or upstream inlet. Ions that strike the insert surface recombine and are emitted as neutrals. This process accounts for the neutral xenon streamlines seen to originate at the emitter surface in Fig. 3.3.1a. Figure 3.3.1e shows the heavy particle gas temperature contours. The gas is heated by Xe-Xe$^+$ collisions, and therefore, the high temperature region between $z = 1.9$ and 2.2 cm coincides with the region containing high plasma densities.

3.3 Minor Species Transport Equations

The transport model presented here describes the diffusion of the minor species through the xenon plasma using conservation equations. The conservation of mass for species j in a gas mixture is expressed by

$$\frac{\partial}{\partial t}(n_j m_j) + \nabla \cdot (n_j m_j \mathbf{u}_j) = m_j \dot{n}_{j,\text{gen}}, \tag{3.3.1}$$

where n_j is the density of species j, m_j is the mass, $\mathbf{u}_j$ is the mean species velocity, and $\dot{n}_{j,\text{gen}}$ is the generation rate of species j. Langevin [7] derives the species momentum transfer equation for a nonreactive gas containing a mixture of two species as

$$\frac{\partial}{\partial t}(n_j m_j \mathbf{u}_j) + \nabla \cdot (n_j m_j \mathbf{u}_j \mathbf{u}_j) = -\nabla P_j + n_j m_j \mathbf{F}_j + \boldsymbol{\beta}_{jk}, \tag{3.3.2}$$

where $P_j = n_j kT$ is the partial pressure of species j, $\mathbf{F}_j$ accounts for an external applied force, $\boldsymbol{\beta}_{jk}$ is the momentum transferred to species j during collisions with species k, and classical, i.e., continuum, viscous momentum transfer is neglected.

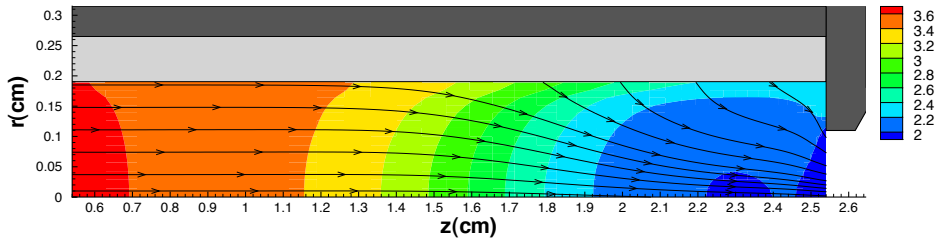

(a) Xenon neutral density, n_n (10^{21} m^{-3}), with neutral streamlines

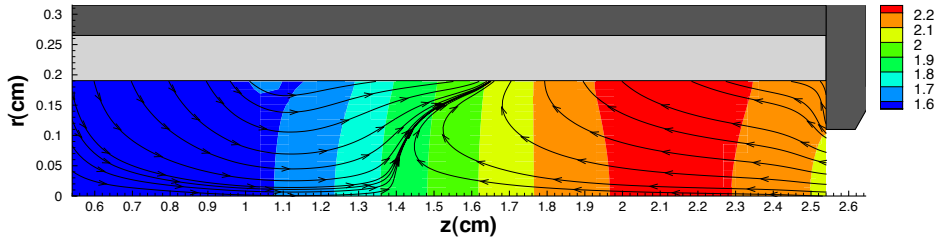

(b) Electron temperature, T_e (eV), with electron current streamlines

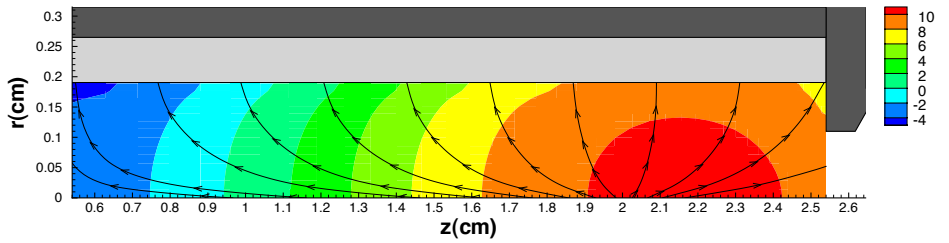

(c) Plasma potential, ϕ (V), with ion current streamlines

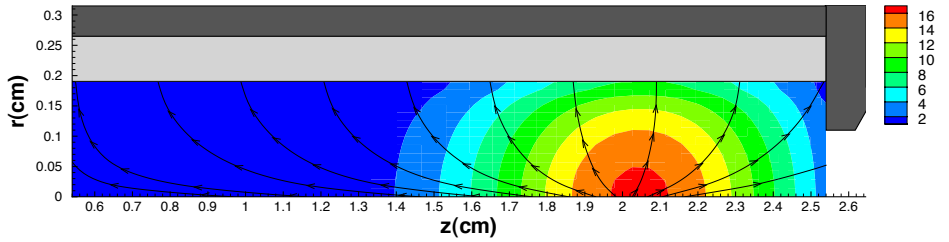

(d) Plasma density, n_e (10^{19} m^{-3}, with ion current streamlines)

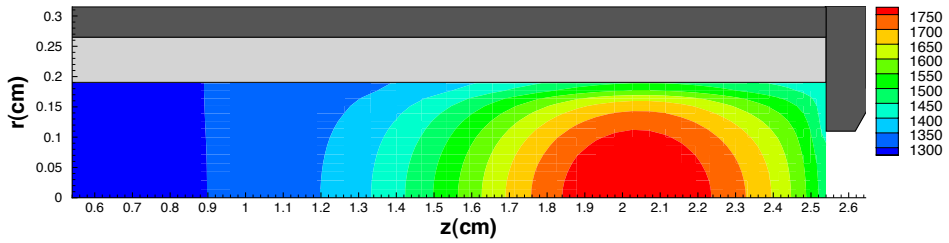

(e) Heavy particle temperature, T_h (K)

Figure 3.3.1: Xenon plasma solution for a discharge current of 15 A and a xenon flow rate of 3.7 sccm [4].

The collision term, $\boldsymbol{\beta}_{jk}$, is approximated by

$$\boldsymbol{\beta}_{jk} = n_j \nu_{jk} \mu_{jk} (\mathbf{u}_k - \mathbf{u}_j), \tag{3.3.3}$$

where ν_{jk} is the collision frequency between j and k particles, and $\mu_{jk} = m_j m_k/(m_j + m_k)$ is the reduced mass. For a reactive mixture, an additional source term must be added to the right-hand side of Eq. (3.3.2) to account for the change in the total momentum by the creation or annihilation of species j particles. This term can be expressed as

$$m_j (S_j \mathbf{u}_{j,\text{birth}} - R_j \mathbf{u}_{j,\text{death}}), \tag{3.3.4}$$

where S_j is the rate at which j particles are created, $\mathbf{u}_{j,\text{birth}}$ is the average velocity of newly created j particles, R_j is the rate at which j particles are lost, and $\mathbf{u}_{j,\text{death}}$ is the mean velocity when they are lost. The difference between S_j and R_j is equivalent to the generation rate of species j, i.e., $\dot{n}_{j,\text{gen}} = S_j - R_j$. We assume that $\mathbf{u}_{j,\text{birth}} = \mathbf{u}_{j,\text{death}} = \mathbf{u}_j$, such that $S_j \mathbf{u}_{j,\text{birth}} - R_j \mathbf{u}_{j,\text{death}} = \dot{n}_{j,\text{gen}} \mathbf{u}_j$.

For neutral particles, there are no externally applied forces and Eq. (3.3.2) can be written as

$$\frac{\partial}{\partial t}(n_j m_j \mathbf{u}_j) + \nabla \cdot (n_j m_j \mathbf{u}_j \mathbf{u}_j) = -\nabla P_j + n_j \nu_{jk} \mu_{jk} (\mathbf{u}_k - \mathbf{u}_j) + \dot{n}_{j,\text{gen}} \mathbf{u}_j. \tag{3.3.5}$$

The following relation is obtained after expanding the terms on the left hand side of Eq. (3.3.5) and combining the result with Eq. (3.3.1):

$$n_j m_j \frac{\partial}{\partial t} \mathbf{u}_j + n_j m_j \left(\mathbf{u}_j \cdot \nabla\right) \mathbf{u}_j = -\nabla P_j + n_j \nu_{jk} \mu_{jk} (\mathbf{u}_k - \mathbf{u}_j). \tag{3.3.6}$$

We assume that the bulk motion of species j is slow enough to neglect the acceleration terms on the left hand side of Eq. (3.3.6). This yields the following equation:

$$-n_j \nu_{jk} \mu_{jk} (\mathbf{u}_k - \mathbf{u}_j) = -\nabla P_j. \tag{3.3.7}$$

Langevin arrives at the expression above in Eq. (3.3.7) and rewrites it in the form of a diffusion equation

$$\mathbf{u}_j - \mathbf{u}_k = -\frac{kT}{\nu_{jk} \mu_{jk}} \frac{1}{P_j} \nabla P_j, \tag{3.3.8}$$

where $(\mathbf{u}_j - \mathbf{u}_k)$ is the differential motion due to diffusion and $D_{jk} = kT/\nu_{jk}\mu_{jk}$ can be identified as the conventional binary diffusion coefficient [7]. In this formulation of momentum transport, the collisions term, $\boldsymbol{\beta}_{jk}$, is a molecular-level representation of diffusive species transport.

This model proposed by Langevin can be extended to a system with more than two particles. In this case, we consider eight minor species: Ba, Ba^+, O, O^+, O_2, O_2^+, BaO, and BaO^+ diffusing

through a gas mixture containing three major species: e^-, Xe, and Xe^+. Since the density of each minor species in the gas is several orders of magnitude lower than the xenon densities, it has been assumed that the minor species only experience momentum exchange with the major species and drag between minor species is neglected. The collision frequency between each of the minor species and each major species is a function of temperature and number density as given below in Eqs. (3.3.9)–(3.3.14), where the subscripts j^n and j^i are used to differentiate between minor neutral species and minor ion species, respectively. Note that $n_e \approx n_{Xe^+}$ due to assuming charge neutrality of the plasma. A detailed discussion of the collision processes between the minor and major species will be presented in §3.4.

$$\nu_{j^n,Xe} = f(n_{Xe}, T_h) \tag{3.3.9}$$

$$\nu_{j^n,Xe^+} = f(n_e, T_h) \tag{3.3.10}$$

$$\nu_{j^n,e^-} = f(n_e, T_e) \tag{3.3.11}$$

$$\nu_{j^i,Xe} = f(n_{Xe}, T_h) \tag{3.3.12}$$

$$\nu_{j^i,Xe^+} = f(n_e, T_h) \tag{3.3.13}$$

$$\nu_{j^i,e^-} = f(n_e, T_e) \tag{3.3.14}$$

The collision term in Eq. (3.3.6) must be modified to account for collisions with each of the three major species and may be written as

$$\boldsymbol{\beta}_{jk} = \sum_k n_j \nu_{jk} \mu_{jk} (\mathbf{u}_k - \mathbf{u}_j), \tag{3.3.15}$$

where the subscript j refers to each of the minor species and the subscript k refers to each of the major species. Note that the collisions between different species must conserve the total momentum, so that the collision terms cancel out when the individual species momentum equations are summed, i.e.,

$$\sum_{\alpha=1}^{11} \sum_{\gamma=1}^{11} \boldsymbol{\beta}_{\alpha\gamma} = \sum_{\alpha=1}^{11} \sum_{\gamma=1}^{11} n_j \nu_{\alpha\gamma} \mu_{\alpha\gamma} (\mathbf{u}_\gamma - \mathbf{u}_\alpha) = 0, \tag{3.3.16}$$

where α and γ represent each of the eleven species in the mixture.

Accounting for the Lorentz force, which acts on the ions, Eq. (3.3.6) can be written as

$$n_j m_j \frac{\partial}{\partial t} \mathbf{u}_j + n_j m_j \left(\mathbf{u}_j \cdot \nabla\right) \mathbf{u}_j = -\nabla P_j + n_j q_j (\mathbf{E} + \mathbf{u}_j \times \mathbf{B}) + \sum_k n_j \nu_{jk} \mu_{jk} (\mathbf{u}_k - \mathbf{u}_j), \tag{3.3.17}$$

where q_j is the particle charge, $\mathbf{E}$ is the electric field, and $\mathbf{B}$ is the magnetic field. Neglecting the

acceleration terms and the magnetic field yields

$$0 = -\nabla P_j + n_j q_j \mathbf{E} + \sum_k n_j \nu_{jk} \mu_{jk} (\mathbf{u}_k - \mathbf{u}_j). \tag{3.3.18}$$

We expand the final term on the right-hand side of Eq. (3.3.18) and solve for the flux, $\mathbf{\Gamma}_j = n_j \mathbf{u}_j$, to obtain

$$\mathbf{\Gamma}_j = n_j \mathbf{u}_j = \frac{1}{\sum_k \nu_{jk} \mu_{jk}} \left(-\nabla P_j + n_j q_j \mathbf{E} + n_j \sum_k \nu_{jk} \mu_{jk} \mathbf{u}_k \right). \tag{3.3.19}$$

Equations (3.3.1) and (3.3.19) represent a set of sixteen equations, where the unknown quantities are the velocity, $\mathbf{u}_j$, and number density, n_j, of each minor species. All other quantities are pre-calculated in the xenon plasma simulation. The inputs to the transport model are calculated from the xenon plasma solution and are assumed to be independent of the dynamics of the barium and oxygen plasma. The seven inputs are: (1) electron temperature, (2) heavy particle temperature, (3) plasma potential, (4) plasma density, (5) xenon neutral density, (6) xenon ion velocity, and (7) pressure. The outputs of the transport model are the minor species densities, velocities, and fluxes. It is assumed that all minor species have thermalized with the xenon, and therefore, all heavy particles in the plasma possess temperature, T_h.

Equations (3.3.1) and (3.3.19) for the minor species are discretized using a finite volume approach and are solved on a two-dimensional axisymmetric mesh 2 cm long with a radius 0.189 cm. The domain has five boundary surfaces as shown in Fig. 3.2.1: (1) the upstream inlet to the cathode, (2) the emitter surface, (3) the face of the orifice plate, (4) the entrance to the cathode orifice, and (5) the centerline.

All vector quantities are edge-centered; all scalar quantities are cell-centered. The minor species fluxes were calculated via Eq. (3.3.19). The initial densities of Ba and BaO were assumed to be uniform throughout the cathode. The flux values were substituted into Eq. (3.3.1), which was then evolved in time until the densities and fluxes achieved steady-state values. Since oxygen was introduced at the cathode inlet, the densities of O, O^+, O_2, and O_2^+ were initially assumed to be zero everywhere. Using the divergence theorem, the discretized form of the continuity equation given in Eq. (3.3.1) is

$$n_{\text{new}} = n_{\text{old}} + dt \left(\dot{n}_{\text{gen}} - \frac{1}{V} \sum_{\alpha=1}^{4} \mathbf{\Gamma}_\alpha \cdot \mathbf{A}_\alpha \right), \tag{3.3.20}$$

where V is the cell volume, dt is the time step and is on the order of 1 ns, $\mathbf{\Gamma}_\alpha$ represents the flux across edge α, and $\mathbf{A}_\alpha$ is the area of edge α.

3.4 Gas Phase Reactions in the Xenon Plasma

The focus of this section is on the collision processes and gas phase reactions that occur in the xenon plasma. The reactions considered in this work are listed in Table 3.1 along with their corresponding rate constants, κ. The reactions are broken down into four main types: (1) momentum transfer between the major and minor species, (2) electron impact ionization, (3) charge exchange, and (4) chemical reactions between barium and oxygen. All temperatures are given in eV and n_e is given in m^{-3}. Each reaction and the method for calculating the rate constant are discussed in further detail in the following text.

Note that three-body electron attachment to O_2 molecules was not considered here. The rate constant for this reaction considering Xe as the third body is on the order of 10^{-44} m^6/s [8]. Given an electron density of $n_e = 10^{19}$ m^{-3} and a xenon neutral density of $n_{\mathrm{Xe}} = 10^{21}$ m^{-3}, the frequency for this reaction is 10^{-4} s^{-1}, which is many orders of magnitude lower than the reactions provided in Table 3.1.

3.4.1 Momentum Transfer by Collisions with Electrons

Electron-neutral collisions. The rate constants for electron-neutral collisions, which correspond to reactions (1), (3), (5), and (7) in Table 3.1, were obtained by integrating momentum transfer cross sections over a Maxwellian velocity distribution [9, 10]:

$$\kappa = \langle \sigma_m \mathbf{u}_e \rangle = \int_0^\infty \chi(c)\sigma_m(c)\, c\, dc. \tag{3.4.1}$$

The distribution of particle speeds within the population derived from Maxwell-Boltzmann statistics is [9]

$$\chi(c) = 4\pi \left(\frac{m}{2\pi k T_m} \right)^{3/2} c^2 e^{-(m/2kT_m)c^2}, \tag{3.4.2}$$

where T_m is the Maxwellian electron temperature and c is the electron velocity. Momentum transfer cross sections for collisions between electrons and atomic oxygen, molecular oxygen, and barium are plotted in Fig. 3.4.1. Momentum transfer cross section measurements for collisions between electrons and barium oxide molecules are not available, and therefore, the rate constant for reaction (3) is not listed in Table 3.1. The rate constant for reaction (5) is also not listed as the momentum cross sections for collisions between electrons and atomic oxygen were measured over a small energy range insufficient for accurate calculations of the integral in Eq. (3.4.1).

Table 3.1: Selected Gas Phase Reactions in the Xenon Discharge

No.	Reaction	Rate Constant, κ (m^3/molecules/s)	Notes
Momentum Transfer Collisions			
1	$e + Ba \rightarrow e + Ba$	$1\times10^{-16}(-1058.5+3333T_e-1520.3T_e^2+357.47T_e^3-43.67T_e^4+2.1874T_e^5)$	a, b
2	$e + Ba^+ \rightarrow e + Ba^+$	$1.1554\times10^{-17}\left(23-\ln\left(1\times10^{-3}\sqrt{n_e/T_e^3}\right)\right)T_e^{-3/2}$	c
3	$e + BaO \rightarrow e + BaO$		d
4	$e + BaO^+ \rightarrow e + BaO^+$	$1.0349\times10^{-17}\left(23-\ln\left(1\times10^{-3}\sqrt{n_e/T_e^3}\right)\right)T_e^{-3/2}$	c
5	$e + O \rightarrow e + O$		d
6	$e + O^+ \rightarrow e + O^+$	$9.9150\times10^{-17}\left(23-\ln\left(1\times10^{-3}\sqrt{n_e/T_e^3}\right)\right)T_e^{-3/2}$	c
7	$e + O_2 \rightarrow e + O_2$	$1\times10^{-17}(1404.7+3824.5T_e-1318T_e^2+386.06T_e^3-60.129T_e^4+3.6594T_e^5)$	a, b
8	$e + O_2^+ \rightarrow e + O_2^+$	$4.9576\times10^{-17}\left(23-\ln\left(1\times10^{-3}\sqrt{n_e/T_e^3}\right)\right)T_e^{-3/2}$	c
9	$Xe + Ba \rightarrow Xe + Ba$	$7.65\times10^{-16}\sqrt{T}$	e
10	$Xe + Ba^+ \rightarrow Xe + Ba^+$	4.05×10^{-16}	f
11	$Xe + BaO \rightarrow Xe + BaO$	$1.87\times10^{-15}\sqrt{T}$	e
12	$Xe + BaO^+ \rightarrow Xe + BaO^+$	3.95×10^{-16}	f
13	$Xe + O \rightarrow Xe + O$	$1.637\times10^{-15}(0.54165T^{-0.1561}+0.193e^{-35.22T}+1.03587e^{-113.13T}+1.76474e^{-287.94T})\sqrt{T}$	e
14	$Xe + O^+ \rightarrow Xe + O^+$	8.79×10^{-16}	f
15	$Xe + O_2 \rightarrow Xe + O_2$	$1.366\times10^{-15}(0.54165T^{-0.1561}+0.193e^{-35.22T}+1.03587e^{-113.13T}+1.76474e^{-287.94T})\sqrt{T}$	e
16	$Xe + O_2^+ \rightarrow Xe + O_2^+$	6.55×10^{-16}	f
17	$Xe^+ + Ba \rightarrow Xe^+ + Ba$	1.27×10^{-15}	f
18	$Xe^+ + Ba^+ \rightarrow Xe^+ + Ba^+$	$4.06\times10^{-15}\left(23-\ln\left(1\times10^{-3}\sqrt{n_e/T^3}\right)\right)T^{-3/2}$	g
19	$Xe^+ + BaO \rightarrow Xe^+ + BaO$	$1\times10^{-16}(17.66837+4.64088T^{-1/2})$	f
20	$Xe^+ + BaO^+ \rightarrow Xe^+ + BaO^+$	$3.73\times10^{-15}\left(23-\ln\left(1\times10^{-3}\sqrt{n_e/T^3}\right)\right)T^{-3/2}$	g
21	$Xe^+ + O \rightarrow Xe^+ + O$	3.92×10^{-16}	f
22	$Xe^+ + O^+ \rightarrow Xe^+ + O^+$	$1.60\times10^{-14}\left(23-\ln\left(1\times10^{-3}\sqrt{n_e/T^3}\right)\right)T^{-3/2}$	g
23	$Xe^+ + O_2 \rightarrow Xe^+ + O_2$	4.08×10^{-16}	f
24	$Xe^+ + O_2^+ \rightarrow Xe^+ + O_2^+$	$1.08\times10^{-14}\left(23-\ln\left(1\times10^{-3}\sqrt{n_e/T^3}\right)\right)T^{-3/2}$	g

Table 3.1: Selected Gas Phase Reactions (continued)

No.	Reaction	Rate Constant, κ (m^3/molecules/s)	Notes
Electron Impact Ionization			
25	$e + Ba \rightarrow Ba^+ + 2e$	$1\times10^{-17}(2447.6-5868.7T_e+4425.4T_e^2-973.82T_e^3+100.91T_e^4-4.1057T_e^5)$	a, h
26	$e + BaO \rightarrow BaO^+ + 2e$	$1\times10^{-18}(326.3-250.95T_e-512.64T_e^2+565.22T_e^3-112.42T_e^4+7.2535T_e^5)$	a, h
27	$e + O \rightarrow O^+ + 2e$	$1 \times 10^{-19}(-587.67 + 1251.9T_e - 851.07T_e^2 + 156.83T_e^3 + 25.828T_e^4 - 3.4624T_e^5)$	a, h
28	$e + O_2 \rightarrow O_2^+ + 2e$	$1 \times 10^{-19}(-570.07 + 1228.3T_e - 834.65T_e^2 + 135.59T_e^3 + 38.381T_e^4 - 4.2665T_e^5)$	a, h
Charge Exchange Processes			
29	$Xe^+ + O_2 \rightarrow Xe + O_2^+$	$1\times10^{-17}(-6.8829+1003.6T-9094.6T^2+54145T^3-169150T^4+212840T^5)$	i, j
30	$O_2^+ + Xe \rightarrow O_2 + Xe^+$	$1\times10^{-17}(-6.8337+961.27T-8296.7T^2+48913T^3-151260T^4+187790T^5)$	i, k
Chemical Reactions			
31	$Ba + O_2 \rightarrow BaO + O$	$2.82 \times 10^{-16}e^{-0.529/T}$	l
32	$Ba^+ + O_2 \rightarrow BaO^+ + O$	$1\times10^{-20}(-2.4545+152.34T-3419.4T^2+30199T^3-55723T^4+32527T^5)$	i
33	$Ba + O_2^+ \rightarrow BaO^+ + O$	2.04×10^{-15}	f

[a] Valid for $1 \leq T_e \leq 5$ eV.

[b] Calculated using Eq. (3.4.1).

[c] Calculated for electron-ion Coulomb collisions using Eqs. (3.4.3) and (3.4.4).

[d] Insufficient data available to calculate rate constant.

[e] Calculated using Eq. (3.4.5).

[f] Calculated using Eq. (3.4.14).

[g] Calculated for ion-ion Coulomb collisions using Eqs. (3.4.15) and (3.4.16).

[h] Calculated using Eq. (3.4.18).

[i] Valid for $0.05 \leq T \leq 0.2$ eV.

[j] Calculated using $O_2^+ + O_2$ charge exchange cross sections and Eq. (3.4.18).

[k] Calculated using $Xe^+ + Xe$ charge exchange cross sections and Eq. (3.4.18).

[l] Determined from Kashireninov et al. [11]

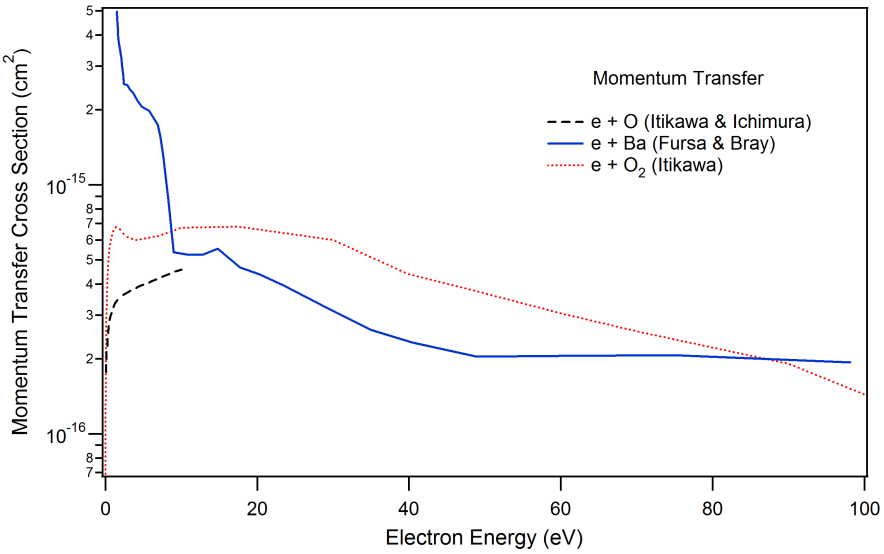

Figure 3.4.1: Momentum transfer cross sections for electrons colliding with atomic oxygen [12], molecular oxygen [13], and barium [14].

Electron-ion collisions. The rate constant for Coulomb collisions between electrons and ions is given by [15]

$$\kappa = \frac{\nu_{j^i,e}}{n_e} = \frac{\sqrt{2}}{3\sqrt{\pi}} \left(\frac{e^2}{4\pi\epsilon_0} \right)^2 \frac{4\pi}{(eT_e)^{3/2}} \frac{\mu_{j^i,e}^{1/2}}{m_{j^i}} \ln \Lambda. \tag{3.4.3}$$

The Coulomb logarithm for electron-ion collisions is given by [15]

$$\ln \Lambda_{ei} = 23 - \ln \left(1 \times 10^{-3} n_e^{1/2} Z T_e^{-3/2} \right), \tag{3.4.4}$$

which is valid for $T_i m_e/m_i < T_e < 10Z^2$ eV. T_e and T_i are the electron and ion temperatures, respectively, and are given in units of eV. n_e is the electron density in m^{-3}, eZ is the particle charge, and m_e and m_i are the electron and ion masses, respectively. The rate constants for these collisions are listed in Table 3.1 and correspond to reactions (2), (4), (6), and (8).

3.4.2 Momentum Transfer by Collisions with Xenon Neutrals and Ions

Neutral-neutral collisions. The rate constant for collisions between two neutral species is given by [9]

$$\kappa = \frac{\nu_{j^n,Xe}}{n_{Xe}} = Q \sqrt{\frac{8eT_h}{\pi \mu_{j^n,Xe}}}, \tag{3.4.5}$$

where Q is the scattering cross section and can be calculated via the following equation for a binary gas mixture [16]:

$$Q = \pi \sigma_{jk}^2 \Omega_{jk}. \tag{3.4.6}$$

The collision diameter for the $j-k$ species pair, denoted by σ_{jk}, is estimated using the collision diameter of each species via the following combining rule [16]:

$$\sigma_{jk} = \frac{\sigma_j + \sigma_k}{2}. \tag{3.4.7}$$

The collision integral for the Lennard-Jones interaction potential, denoted by Ω_{jk}, can be expressed using the following empirical fit [16]:

$$\Omega_{jk} = A(T^*)^{-B} + Ce^{-DT^*} + Ee^{-FT^*} + Ge^{-HT^*}, \tag{3.4.8}$$

where the dimensionless temperature, T^*, is given by $T^* = eT/\varepsilon_{jk}$ for T in eV. ε_{jk} is determined for the $j-k$ pair using the combining rule [16]:

$$\varepsilon_{jk} = \sqrt{\varepsilon_j \varepsilon_k}. \tag{3.4.9}$$

The values of the fit coefficients for Eq. (3.4.8) are given in Table 3.2 [16]. The Lennard-Jones parameters, ϵ and σ, can be estimated using either viscosity data or critical properties. The values used here for oxygen and xenon are: $\sigma_{O_2} = 3.467$ Å, $\sigma_O = 3.050$ Å, $\sigma_{Xe} = 4.047$ Å, $\varepsilon_{O_2}/k = \varepsilon_O/k = 106.7$ K, $\varepsilon_{Xe}/k = 231.0$ K [16, 17]. Since neither viscosity data nor critical properties are available for barium, the Ba-Xe scattering cross section was taken to be constant at $Q_{Ba-Xe} = 40$ Å^2 based on diffusion measurements of barium in xenon [3, 18]. The scattering cross section for barium oxide and xenon was calculated using the hard-sphere model [9]:

$$Q_{BaO-Xe} = \pi \left(r_{BaO} + r_{Xe}\right)^2, \tag{3.4.10}$$

where r is the van der Waals radius. The radius of the BaO molecule was taken to be half that of the sum of the bond length and the atomic radii of Ba and O. Given a Ba–O bond length of 2.76 Å [19] and the following van der Waals radii, $r_{Ba} = 2.70$ Å and $r_O = 1.55$ Å [20], the BaO radius was estimated to be $r_{BaO} = 3.50$ Å. For $r_{BaO} = 3.50$ Å [20] and $r_{Xe} = 2.16$ Å [21], the BaO-Xe scattering cross section is $Q_{BaO-Xe} = 100.64$ Å^2. The rate constants for these collisions are listed in Table 3.1 and correspond to reactions (9), (11), (13), and (15).

Table 3.2: Empirical Coefficients of Ω_{jk} [16]

$A = 1.06036$	$E = 1.03587$
$B = 0.15610$	$F = 1.52996$
$C = 0.19300$	$G = 1.76474$
$D = 0.47635$	$H = 3.89411$

Ion-neutral collisions. During ion-neutral scattering, a dipole moment may be induced in the neutral particle by the ion's electric field as given by [22]

$$\mu_D = \alpha_p \epsilon_0 E = \alpha_p \frac{e}{4\pi r^2}, \tag{3.4.11}$$

where μ_D is the dipole moment, α_p is the polarizability of a neutral atom or molecule, E is the electric field, and r is the distance between the interacting particles. The induced dipole moment exerts a force on the incoming particle, which leads to Langevin polarization capture [23]. The critical impact parameter, b, is determined via conservation of energy and angular momentum to yield

$$\sigma_L = \pi b^2 = \sqrt{\frac{\pi \alpha_p e^2}{\epsilon_0 \mu v_{\text{rel}}^2}}, \tag{3.4.12}$$

where μ is the reduced mass of the pair and v_{rel} is the relative velocity between the two particles [23]. The rate constant is therefore

$$\kappa = \frac{\nu_L}{n} = \sigma_L v_{\text{rel}} = \sqrt{\frac{\pi \alpha_p e^2}{\epsilon_0 \mu}}. \tag{3.4.13}$$

The Langevin cross section given in Eq. (3.4.12) is enhanced for interactions with molecules that have a permanent dipole [23, 24]:

$$\kappa = \frac{\nu_L}{n} = \sqrt{\frac{\pi \alpha_p e^2}{\epsilon_0 \mu}} + c \frac{q \mu_D}{\sqrt{2\pi \epsilon_0^2 \mu e T}}, \tag{3.4.14}$$

where c is a parameter between 0 and 1 that accounts for the effectiveness of the ion locking in the dipole, i.e., $c = 0$ corresponds to free rotation of the dipole and $c = 1$ corresponds to a locked dipole where $\theta = 0$ with respect to vector between the two particles [24, 25]. The dipole moment, μ_D, is calculated as the product of the total positive or negative charge and the distance between the charge centroids. The BaO dipole moment was calculated to be 8.843×10^{-29} C $\cdot$ m for a Ba–O bond length of 2.76 Å [19]. Note that O_2 does not have a permanent dipole moment as the molecule is symmetric. Values for the polarizability of various atomic and molecular species of interest to this work are given in Table 3.3.

Table 3.3: Ionization Potentials and Polarizabilities

Species	Φ (eV) [26]	α_p (Å^3)
Xe	12.13	4.044 [27]
Ba	5.21	39.7 [27]
BaO	6.91	40.5[a]
O	13.62	0.802 [27]
O_2	12.07	1.57 [23]

[a] Estimated by adding the polarizabilities of the constituent atoms.

Mixed ion-ion collisions. The rate constant for Coulomb collisions between minor species ions and xenon ions is given by [15]

$$\kappa = \frac{\nu_{j^i,Xe+}}{n_e} = \frac{\sqrt{2}}{3\sqrt{\pi}} \left(\frac{e^2}{4\pi\epsilon_0}\right)^2 \frac{4\pi}{(eT_h)^{3/2}} \frac{\mu_{j^i,Xe}^{1/2}}{m_{j^i}} \ln\Lambda. \tag{3.4.15}$$

The Coulomb logarithm for mixed ion-ion collisions is given by [15]

$$\ln\Lambda_{ii'} = 23 - \ln\left[1\times10^{-3}\frac{ZZ'(m+m')}{mT_{i'}+m'T_i}\left(\frac{n_iZ^2}{T_i}+\frac{n_{i'}Z'^2}{T_{i'}}\right)^{1/2}\right], \tag{3.4.16}$$

where eZ is the particle charge, T_i is the heavy particle temperature in eV, and $n_e = n_i$ is the plasma density in m^{-3}. The following assumptions are employed: all ions are singly charged, i.e., $Z_i = Z_{i'} = 1$, the minor species ions have thermalized with the xenon ions, i.e., $T_i \approx T_{i'}$, and the Xe^+ density is much greater than the minor species ion density, i.e., $n_{i'} \gg n_i$. The rate constants for these collisions are listed in Table 3.1 and correspond to reactions (18), (20), (22), and (24).

3.4.3 Electron Impact Ionization

The ion generation rate of species j is determined by the product of the neutral density of species j and the ionization rate:

$$\dot{n}_{j^+,\text{gen}} = n_j\nu_{j^n,e}^{iz}. \tag{3.4.17}$$

The ionization rate constant was obtained by integrating electron impact ionization cross sections over a Maxwellian velocity distribution:

$$\kappa = \frac{\nu_j^{iz}}{n_e} = \langle\sigma_{iz}\mathbf{u}_e\rangle = \int_0^\infty \chi(c)\sigma_{iz}(c)\,c\,dc, \tag{3.4.18}$$

where $\chi(c)$ was given in Eq. (3.4.2).

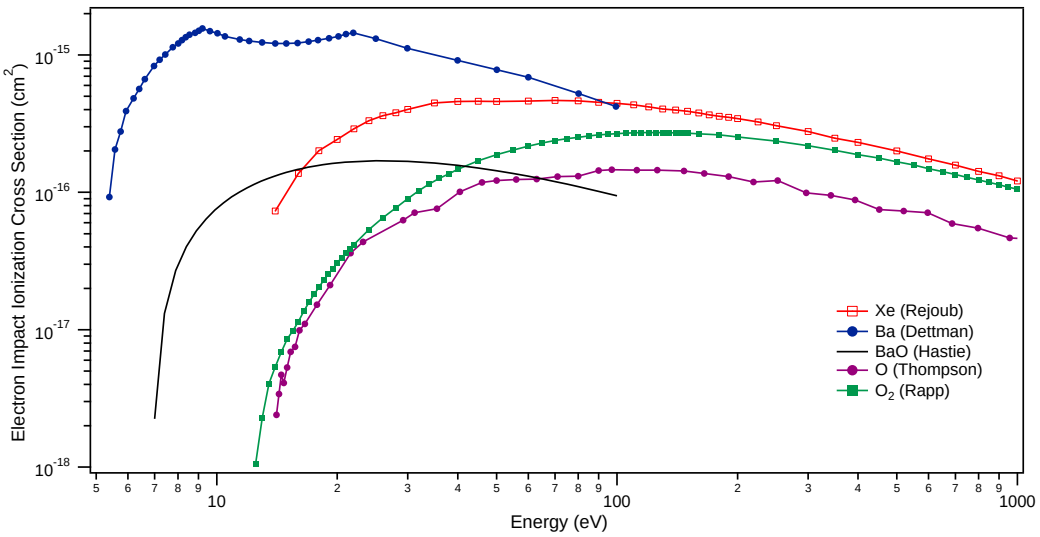

Figure 3.4.2: Electron impact ionization cross sections for xenon [28], barium [29], barium oxide [30, 31], atomic oxyen [32], and molecular oxygen [33].

The electron impaction ionization cross sections plotted in Fig. 3.4.2 for Xe, Ba, O, and O_2 were obtained directly from the literature cited in the figure. For the ionization of BaO, Hastie, Bonnell, and Schenck measured a single maximum cross section of $\sigma_m = 1.7 \times 10^{-16}$ cm^2 at an electron energy of $E_m = 26$ eV [30]. This value of σ_m is scaled over a range of energy values using the following analytical model [31]:

$$\sigma(E) = \frac{3.86\sigma_m \left(\dfrac{E-\Phi}{E_m-\Phi}\right)^{1.127}}{\left(0.8873 + \dfrac{E-\Phi}{E_m-\Phi}\right)^{2.127}}, \tag{3.4.19}$$

where Φ is the ionization potential. The resulting BaO ionization cross sections are plotted in Fig. 3.4.2. The rate constants for electron impact ionization are listed in Table 3.1 and correspond to reactions (25)–(28). Note that the rate constants for electron impact ionization of O and O_2 are several orders of magnitude lower than the rate constants for ionization of Ba and BaO as shown in Fig. 3.4.3. Electron-ion recombination of the minor species occurs at the cathode surfaces, but is not considered in the plasma since the electron-ion collision frequencies are several orders of magnitude lower than the electron-neutral collisions frequences.

3.4.4 Charge Exchange Processes

Consider the following reaction in which an ion collides with an atom and captures a valence electron:

$$A^+ + B \rightarrow A + B^+ + \Delta E. \tag{3.4.20}$$

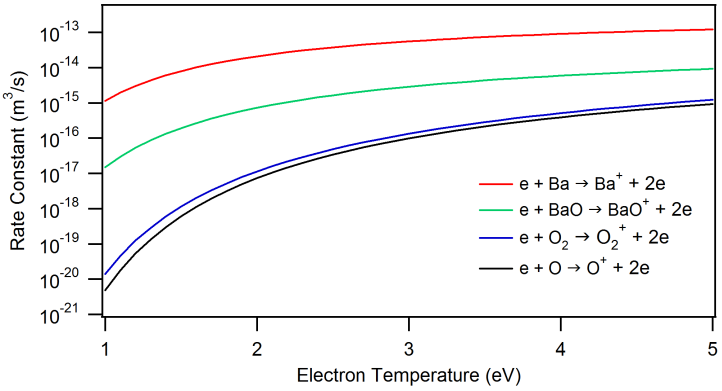

Figure 3.4.3: Rate constants for electron impact ionization of barium, barium oxide, atomic oxyen, and molecular oxygen.

An energy defect, ΔE, occurs when the energy level of the valence electron in particle B is not equal to the energy level of the electron after capture by particle A, i.e., $\Delta E = \Phi_B - \Phi_A$, where Φ is the ionization potential [23]. When $\Delta E = 0$, the process is called resonant charge exchange and is characterized by a large cross section. Classical charge exchange cross sections depend only on the ionization potential and are independent of the kinetic energy of the ion. However, actual charge exchange cross sections are much higher at low energies when electron tunneling is considered [22].

Figure 3.4.4 shows the charge exchange cross sections for O_2^++O_2 resonant charge exchange and Xe^++Xe resonant charge exchange. Data from Stebbings et al. [34] is extrapolated to lower ion energies using the following equation from Rapp and Francis, which is valid for ion energies greater than 0.052 eV [35]:

$$\sigma = (-k_1 \ln v + k_2)^2, \tag{3.4.21}$$

where k_1 and k_2 are fit constants.

Xenon and molecular oxygen can exchange charges during collisions, and because their ionization potentials are so similar (Φ_{Xe} = 12.13 eV and Φ_{O_2} = 12.07 eV), this process can be considered resonant. Ionization potentials are listed in Table 3.3. Since cross section data for Xe^++O_2 and O_2^++Xe charge exchange are not available, these processes are respectively modeled as O_2^++O_2 and Xe^++Xe resonant charge exchange. That is, the O_2^++O_2 cross section data extrapolated from Stebbings et al. [34] is used to describe Xe^++O_2 charge exchange, and the Xe^++Xe cross section data from Miller et al. [36] is used to describe O_2^++Xe charge exchange. From Table 3.3, xenon has a larger polarizability than molecular oxygen, and therefore, the charge exchange cross sections for O_2^++Xe charge exchange should be higher than the reverse reaction. The Xe^++Xe charge exchange cross sections are approximately twice as large as the O_2^++O_2 charge exchange cross sections as shown in Fig. 3.4.4.

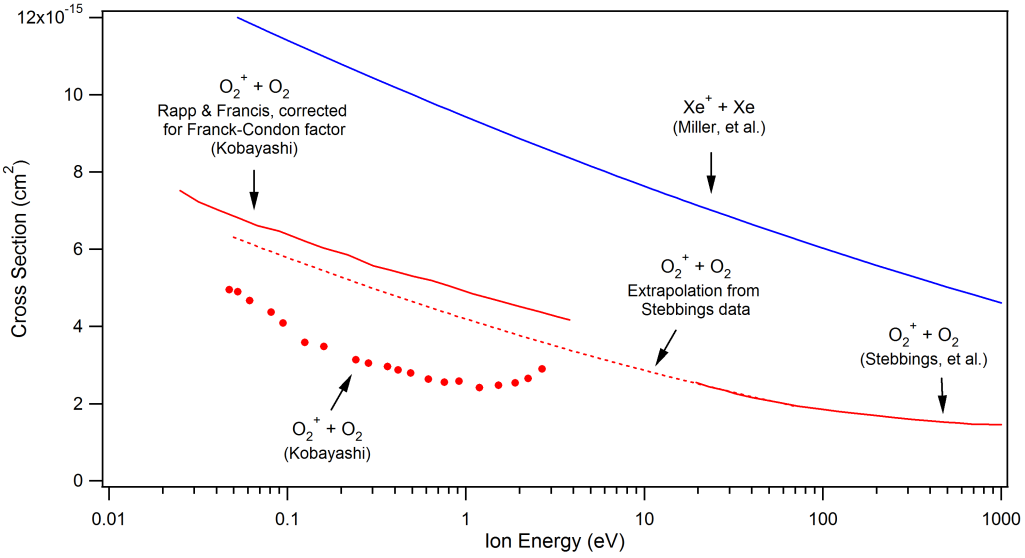

Figure 3.4.4: Charge exchange cross sections for Xe^++Xe [36] and O_2^++O_2 [34, 37]

.

Charge exchange between Xe^+ and O was not considered here as the reaction is endothermic and has an energy defect of 1.49 eV. For endothermic reactions (i.e., where $\Delta E > 0$) the threshold energy is equal to the energy defect and the rate constant for these charge exchange collisions is small for the heavy particle temperatures in the cathode [23].

The rate constants for Xe^++O_2 and O_2^++Xe charge exchange, which correspond to reactions (29) and (30) in Table 3.1, were calculated from Eq. (3.4.18) and the data given in Fig. 3.4.4 for ion temperatures between 0.05 and 0.2 eV.

3.4.5 Chemical Reactions

Barium oxide and atomic oxygen are generated via reactions between barium and molecular oxygen according to the reaction:

$$\mathrm{Ba} + \mathrm{O_2} \rightarrow \mathrm{BaO} + \mathrm{O}, \quad \Delta H_R^\circ = -0.557\,\mathrm{eV}. \tag{3.4.22}$$

The rate constant for this reaction was measured by Kashireninov et al., for temperatures between 970 and 1180 K and fits to an Arrhenius equation [11]. The rate constant is extrapolated out to typical cathode operating temperatures. Ion-neutral collisions may also occur, resulting in the following possible reactions:

$$Ba^+ + O_2 \rightarrow BaO^+ + O, \qquad \Delta H_R^\circ = 1.143\,\text{eV}, \tag{3.4.23}$$

$$Ba^+ + O_2 \rightarrow BaO + O^+, \qquad \Delta H_R^\circ = 7.853\,\text{eV}, \tag{3.4.24}$$

$$Ba + O_2^+ \rightarrow BaO^+ + O, \qquad \Delta H_R^\circ = -5.717\,\text{eV}, \tag{3.4.25}$$

$$Ba + O_2^+ \rightarrow BaO + O^+, \qquad \Delta H_R^\circ = 0.993\,\text{eV}. \tag{3.4.26}$$

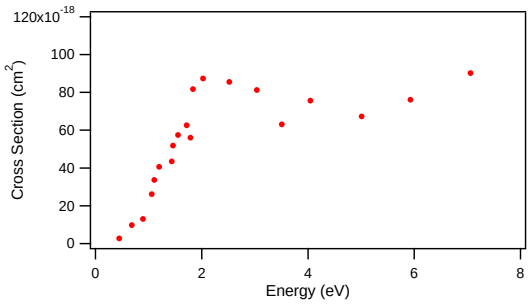

Figure 3.4.5: Cross sections for the reaction, $Ba^+ + O_2 \rightarrow BaO^+ + O$ [38].

The most favorable reactions for Ba^+ reacting with O_2 and Ba reacting with O_2^+ are those given in Eqs. (3.4.23) and (3.4.25), respectively. The reactions in Eqs. (3.4.24) and (3.4.26) will subsequently be neglected. Since the reaction in Eq. (3.4.25) is exothermic, a reasonable assumption is that the reaction proceeds to completion every time Ba and O_2^+ collide. Therefore, the reaction rate constant for Eq. (3.4.25) is assumed to be equal to the Langevin rate constant given in Eq. (3.4.13). The cross sections for the reaction given in Eq. (3.4.23) have been measured by Murad and are reproduced in Fig. 3.4.5. A comparison between the rate constants of the three reactions considered here are presented in Fig. 3.4.6. The reverse reactions for Eqs. (3.4.22), (3.4.23) and (3.4.25) are not considered here as the densities of BaO and O are much smaller than the densities of Ba and O_2.

Note that the dissociation energy of O_2 is 5.12 eV [39], and the dissociation energy of BaO is 5.42 eV [40]. Since these energies are relatively high, dissociation of these molecules will be neglected in this work.

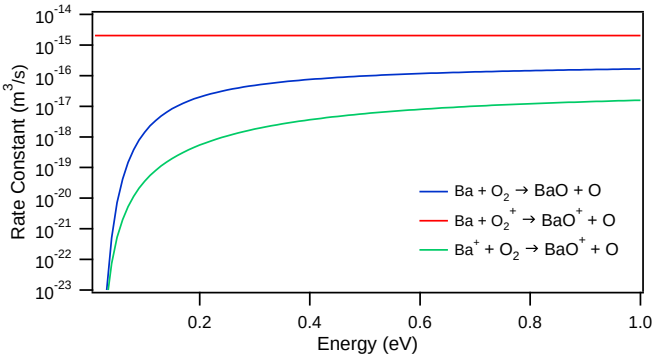

Figure 3.4.6: The rate constants for the formation of BaO.

3.5 Transport Model with Ba and BaO: No Oxygen Poisoning

The results of the transport model for normal cathode operation considering only Ba and BaO neutrals and ions are presented here. In this case, Ba and BaO are introduced into the gas via evaporation from the emitter pores, and ions are generated via electron impact ionization. Equations (3.3.1) and (3.3.19) are solved for Ba, Ba^+, BaO, and BaO^+ on a background xenon plasma.

The collision processes included in Eq. (3.3.19) are momentum transfer collisions with electrons, xenon neutrals, and xenon ions. These processes correspond to reactions (1)–(4), (9)–(12), and (17)–(20) of Table 3.1. Note that momentum transfer between electrons and BaO is not included here as there were insufficient data to determine the rate constant for this reaction. In the momentum equation for Ba, the electron drag term is several orders of magnitude lower than the xenon drag terms, and therefore it appears safe to neglect the electron drag term for collisions with BaO. Electron impact ionization of Ba and BaO, which correspond to reactions (25) and (26) in Table 3.1, is included in the model.

Conservation of barium atoms in the discharge plasma is described by

$$\dot{n}_{Ba} + \dot{n}_{Ba^+} + \dot{n}_{BaO} + \dot{n}_{BaO^+} = 0, \tag{3.5.1}$$

and conservation of oxygen atoms is described by

$$\dot{n}_{BaO} + \dot{n}_{BaO^+} = 0, \tag{3.5.2}$$

where the generation terms are expressed as

$$\dot{n}_{Ba} = -n_{Ba} n_e \kappa_{25}, \tag{3.5.3}$$

$$\dot{n}_{Ba^+} = n_{Ba} n_e \kappa_{25}, \tag{3.5.4}$$

$$\dot{n}_{BaO} = -n_{BaO} n_e \kappa_{26}, \tag{3.5.5}$$

$$\dot{n}_{BaO^+} = n_{BaO} n_e \kappa_{26}. \tag{3.5.6}$$

Note that the subscript on the rate constant, κ, refers to the reaction number in Table 3.1. The boundary conditions for this case are described in the following section, and the results of the simulation are presented in §3.5.2.

3.5.1 Boundary Conditions

The domain has five boundary surfaces as shown previously in Fig. 3.2.1 and below in Fig. 3.5.1. The net flux is prescribed at each boundary and is defined as

$$\mathbf{\Gamma}_{\text{net}} = \mathbf{\Gamma}_{\text{in}} + \mathbf{\Gamma}_{\text{out}}, \tag{3.5.7}$$

where $\mathbf{\Gamma}_{\text{in}}$ and $\mathbf{\Gamma}_{\text{out}}$ refer to the flux into and out of the plasma control volume, respectively. The direction of the flux vectors and a summary of the boundary conditions are shown in Fig. 3.5.1. A detailed discussion of the boundary conditions at each surface is presented in the following text.

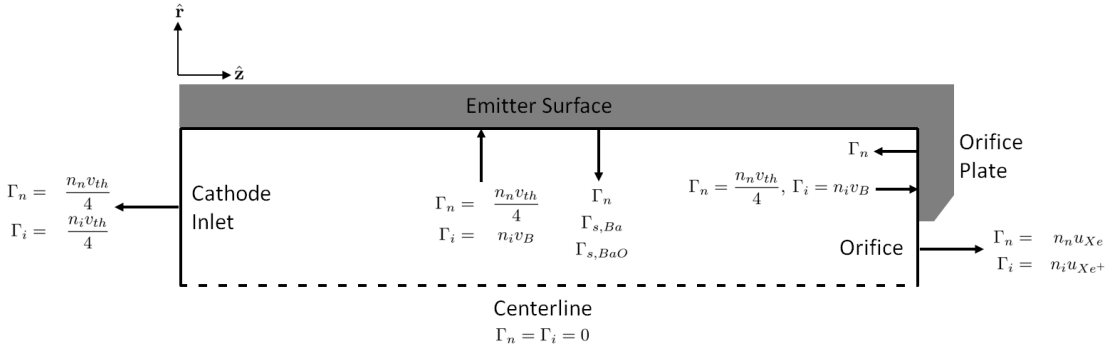

Figure 3.5.1: Diagram of the transport model boundary conditions.

Upstream inlet to the cathode. Ions and neutrals flow out of the plasma control volume and upstream across this boundary at the thermal velocity. There is no source of Ba or BaO at this boundary, and therefore, the net fluxes at the cathode inlet boundary are given by

$$\mathbf{\Gamma}_{Ba} = -\frac{n_{Ba}}{4}\left(\frac{8kT_h}{\pi m_{Ba}}\right)^{1/2}\hat{\mathbf{z}}, \tag{3.5.8}$$

$$\mathbf{\Gamma}_{Ba^+} = -\frac{n_{Ba^+}}{4}\left(\frac{8kT_h}{\pi m_{Ba}}\right)^{1/2}\hat{\mathbf{z}}, \tag{3.5.9}$$

$$\mathbf{\Gamma}_{BaO} = -\frac{n_{BaO}}{4}\left(\frac{8kT_h}{\pi m_{BaO}}\right)^{1/2}\hat{\mathbf{z}}, \tag{3.5.10}$$

$$\mathbf{\Gamma}_{BaO^+} = -\frac{n_{BaO^+}}{4}\left(\frac{8kT_h}{\pi m_{BaO}}\right)^{1/2}\hat{\mathbf{z}}. \tag{3.5.11}$$

Emitter surface. Gaseous Ba and BaO are generated in the emitter via reactions between the impregnant material and the tungsten matrix. These products then flow through the emitter pores and enter the plasma control volume across this boundary. The supply rate of Ba and BaO is driven by the difference between the pressure at the reaction front and the barium partial pressure at the surface [2]. As discussed in Chapter 1, during cathode operation the insert pores become depleted

of barium over time. The reaction front recedes further into the pores, thus increasing the distance through which these species must flow to reach the surface. Therefore, the arrival rate of barium to the surface must also depend on the depletion depth and subsequently, the operating time.

Roquais et al. [41] measured the barium depletion depth with time for vacuum dispenser cathodes containing 4:1:1 impregnant over a range of temperatures. Polk et al. [2] use these data to derive an expression for the barium supply flux, $\Gamma_{s,Ba}$. Polk's derivation is presented here and the results are used in this transport model. It has been observed that the evaporants from a 4:1:1 dispenser cathode consist of a molar ratio of Ba to BaO of 13.3:1 [42], and therefore, the supply rate of BaO from the emitter surface is taken to be $\Gamma_{s,BaO} = \Gamma_{s,Ba}/13.3$.

The barium vapor flow through the emitter pores is assumed to be Knudsen flow [2], in which the mean free path for collisions with other gas molecules is much larger than the pore dimensions. The flux of particles through a unit surface perpendicular to the x axis determined from kinetic theory [9] is given by

$$\Gamma = \frac{v_{th}\lambda}{3}\frac{dn}{dx}, \tag{3.5.12}$$

where $v_{th} = \sqrt{8kT/\pi m}$ is the thermal velocity for temperature measured in K, λ is the mean free path of the particles in m, and n is the particle number density in m^{-3}. Substitution of $n = P/kT$ into the above equation yields

$$\Gamma = \frac{1}{3}\frac{v_{th}\lambda}{kT}\frac{dP}{dx} = \frac{4}{3}\lambda(2\pi mkT)^{-1/2}\frac{dP}{dx}. \tag{3.5.13}$$

Since the tungsten emitter contains a series of pores that may be interconnected, tortuous, and of varying radii, the mean free path in Eq. (3.5.13) must be replaced by an effective mean free path that accounts for these geometric factors [41]. Additionally, the pressure gradient may be approximated as the difference between the vapor pressure at the reaction front and the barium partial pressure at the surface divided by the depletion depth [41]. Note that for vacuum cathodes, the barium partial pressure at the surface is negligible compared with the vapor pressure. Accounting for the above considerations, the barium flux through the pores of Roquais' vacuum cathodes can be written as [41]

$$\Gamma^{R}_{s,Ba} = \frac{4}{3}\frac{\lambda_{\mathrm{eff,R}}}{(2\pi m_{Ba}kT)^{1/2}}\frac{P_v}{\delta}, \tag{3.5.14}$$

where P_v is the barium vapor pressure. The wall temperature, T_w, can be used to determine the vapor pressure in Torr via the following relation [43]:

$$\log P_v = 8.56 - 20360T_w^{-1}. \tag{3.5.15}$$

An expression for the barium flux to the surface similar to Eq. (3.5.14) can be derived for the plasma cathodes studied in this work and is given below in Eq. (3.5.16). The most significant

difference between Eqs. (3.5.14) and (3.5.16) is that in plasma cathodes the barium partial pressure, $P_{Ba} = n_{Ba}kT$, is no longer negligble.

$$\Gamma_{s,Ba} = \frac{4}{3}\frac{\lambda_{\text{eff,HC}}}{(2\pi m_{Ba}kT)^{1/2}}\left(\frac{P_v - P_{Ba}}{\delta}\right). \tag{3.5.16}$$

The porosity of Roquais' vacuum dispenser cathode is different from the porosity of the hollow cathodes used in this work, although the substrate and impregnant materials are the same [2]. The ratio of the effective mean free paths for the two different cathodes is reported as $C = \lambda_{\text{eff,R}}/\lambda_{\text{eff,HC}} = 1.2$ [2]. Combining Eqs. (3.5.14) and (3.5.16) gives

$$\Gamma_{s,Ba} = \frac{\Gamma^R_{s,Ba}}{C}\left(\frac{P_v - P_{Ba}}{P_v}\right). \tag{3.5.17}$$

The term $\Gamma^R_{s,Ba}$ in Eq. (3.5.17) can be expressed in terms of the mass flow rate through the pores by

$$\Gamma^R_{s,Ba} = \frac{dm_{Ba}}{dt}\frac{1}{m_{Ba}\,S}\,, \tag{3.5.18}$$

where dm_{Ba}/dt is the mass flow rate, m_{Ba} is the mass of a barium atom ($m = 2.29\times10^{-25}$ kg), and S is the area of the surface that is emitting barium. The barium mass flow rate can be expressed in terms of the barium depletion rate, $d\delta/dt$, as follows:

$$\frac{dm_{Ba}}{dt} = \rho S\,\Pi_R\tau\zeta\frac{d\delta}{dt}\,, \tag{3.5.19}$$

where ρ is the density of the impregnant, $\Pi_R = 0.185$ is the porosity of Roquais' cathode [41], τ is the fraction of the pore volume filled with impregnant, ζ is the mass fraction of the impregnant that liberates barium, and δ is the barium depletion depth. Note that the reaction is inhibited if the barium partial pressure in the plasma exceeds the vapor pressure of the reaction front.

Roquais et al. determined that the depletion depth varies with time according to the relation [41]

$$\delta = Bt^{1/2}, \tag{3.5.20}$$

and that the depletion factor, B, varies with temperature via the following relation:

$$B(T) = \left(1.0414\times10^{-4}e^{-3.17e/kT}\right)^{1/2}, \tag{3.5.21}$$

where B is in units of m s$^{-1/2}$ and T is in K. Combining the time derivative of Eq. (3.5.20) with Eqs. (3.5.17)–(3.5.19) yields

$$\Gamma_{s,Ba} = \frac{\rho\Pi_R\tau\zeta}{m_{Ba}C}\frac{B^2}{2\delta}\left(\frac{P_v - P_{Ba}}{P_v}\right). \tag{3.5.22}$$

The density of the mixture was calculated as 4730 kg/m^3 using

$$\rho = \sum_i x_i \rho_i, \tag{3.5.23}$$

where x_i is the mass fraction of each species in the mixture. The following densities were used for each species: $\rho_{\mathrm{BaO}} = 5720$ kg/m^3, $\rho_{\mathrm{CaO}} = 3350$ kg/m^3, and $\rho_{\mathrm{Al_2O_3}} = 4000$ kg/m^3. We assume that $\tau = 1$ and that the mass fraction of the impregnant that releases barium is $\zeta = 0.39$ [2]. A depletion depth of 2 μm was chosen to simulate beginning of life conditions. Note that the transport model is relatively insensitive to changes in the depletion depth.

It has been shown that the build-up of multiple barium layers is unstable at normal cathode operating temperatures [44], and therefore, the emitter surface is assumed to be in steady state so that no particles are allowed to accumulate on the surface. Ions leave the plasma control volume and strike the surface at the Bohm velocity. The ions then recombine at the surface according to

$$\mathrm{A}^+ + \mathrm{e} \rightarrow \mathrm{A} \tag{3.5.24}$$

and leave as neutrals at the thermal velocity. No ions are released from the surface back into the gas, and therefore, the net ion fluxes at the emitter surface are

$$\mathbf{\Gamma}_{Ba^+} = n_{Ba^+} \left(\frac{kT_e}{m_{Ba}} \right)^{1/2} \hat{\mathbf{r}}, \tag{3.5.25}$$

$$\mathbf{\Gamma}_{BaO^+} = n_{BaO^+} \left(\frac{kT_e}{m_{BaO}} \right)^{1/2} \hat{\mathbf{r}}. \tag{3.5.26}$$

Since the surface is in steady state, the total flux of barium and barium oxide must be zero at the surface. This means that flux of barium and barium oxide to the surface (either through the pores or via adsorption from the gas phase) must be balanced by desorption of these species from the surface. Therefore, the net neutral flux at the surface is

$$\mathbf{\Gamma}_{Ba} = -\left[n_{Ba^+} \left(\frac{kT_e}{m_{Ba}} \right)^{1/2} + \Gamma_{s,Ba} \right] \hat{\mathbf{r}}, \tag{3.5.27}$$

$$\mathbf{\Gamma}_{BaO} = -\left[n_{BaO^+} \left(\frac{kT_e}{m_{BaO}} \right)^{1/2} + \Gamma_{s,BaO} \right] \hat{\mathbf{r}}. \tag{3.5.28}$$

If the reactions supplying Ba and BaO are inhibited, the net neutral flux simply balances the ion flux to the surface.

Orifice plate. The orifice plate is a non-emitting surface and is assumed to be in steady state so that no particles are allowed to accumulate on the surface. Ions leave the plasma control volume

and strike this surface at the Bohm velocity. The ions then recombine at the surface and leave as neutrals—no ions are released from the surface back into the gas. The net ion fluxes at the orifice plate boundary are therefore

$$\mathbf{\Gamma}_{Ba^+} = n_{Ba^+} \left(\frac{kT_e}{m_{Ba}} \right)^{1/2} \hat{\mathbf{z}}, \tag{3.5.29}$$

$$\mathbf{\Gamma}_{BaO^+} = n_{BaO^+} \left(\frac{kT_e}{m_{BaO}} \right)^{1/2} \hat{\mathbf{z}}. \tag{3.5.30}$$

Since the surface is in steady state, the total flux of each species must be zero at the surface, i.e.,

$$\mathbf{\Gamma}_{Ba} + \mathbf{\Gamma}_{Ba^+} = 0, \tag{3.5.31}$$

$$\mathbf{\Gamma}_{BaO} + \mathbf{\Gamma}_{BaO^+} = 0. \tag{3.5.32}$$

Therefore, the net neutral fluxes at these surfaces are

$$\mathbf{\Gamma}_{Ba} = -\mathbf{\Gamma}_{Ba^+}, \tag{3.5.33}$$

$$\mathbf{\Gamma}_{BaO} = -\mathbf{\Gamma}_{BaO^+}. \tag{3.5.34}$$

Entrance to cathode orifice. In the Polk et al. version of the transport model, the neutrals are assumed to flow out of the plasma control volume through the cathode orifice at the thermal velocity [3]. Imposing this boundary condition for BaO causes steep gradients in the BaO neutral densities near the orifice, which is unphysical. In this work, it is assumed that all neutrals flow out of the plasma control volume at the xenon neutral velocity. This assumption does not significantly alter the results of Polk's barium simulation since the barium density is so low near the orifice. Ions are assumed to flow out of the plasma control volume with the xenon ion velocity. The solution appears to be relatively insensitive to changes in this boundary condition, with the exception of the BaO neutrals as noted above. The fluxes at this boundary are given by

$$\mathbf{\Gamma}_{Ba} = n_{Ba} u_{Xe} \, \hat{\mathbf{z}}, \tag{3.5.35}$$

$$\mathbf{\Gamma}_{Ba^+} = n_{Ba^+} u_{Xe^+} \hat{\mathbf{z}}, \tag{3.5.36}$$

$$\mathbf{\Gamma}_{BaO} = n_{BaO} u_{Xe} \hat{\mathbf{z}}, \tag{3.5.37}$$

$$\mathbf{\Gamma}_{BaO^+} = n_{BaO^+} u_{Xe^+} \, \hat{\mathbf{z}}. \tag{3.5.38}$$

Centerline. This is a symmetry boundary and the ion and neutral fluxes are set to zero:

$$\mathbf{\Gamma}_{Ba^+} = \mathbf{\Gamma}_{Ba} = 0 \, \hat{\mathbf{r}}, \tag{3.5.39}$$

$$\mathbf{\Gamma}_{BaO^+} = \mathbf{\Gamma}_{BaO} = 0\,\hat{\mathbf{r}}. \tag{3.5.40}$$

3.5.2 Results and Discussion

The transport model considering Ba and BaO neutrals and ions was run for a discharge current of 15 A and a xenon flow rate of 3.7 sccm. This condition was initially chosen as it corresponds to an operating condition of the NSTAR discharge cathode and can be used for comparison purposes. The model was not run for lower current densities because of convergence issues; however, the results presented here can still provide a qualitative understanding of the minor species dynamics in the cathode.

The transport model was run for 2×10^6 cycles at a time step of $dt = 3\times10^{-9}$ s until the densities reached equilibrium. Plots of the densities versus number of cycles are shown in Fig. 3.5.2. Contour plots of the transport model solution are shown in Figs. 3.5.3 and 3.5.4.

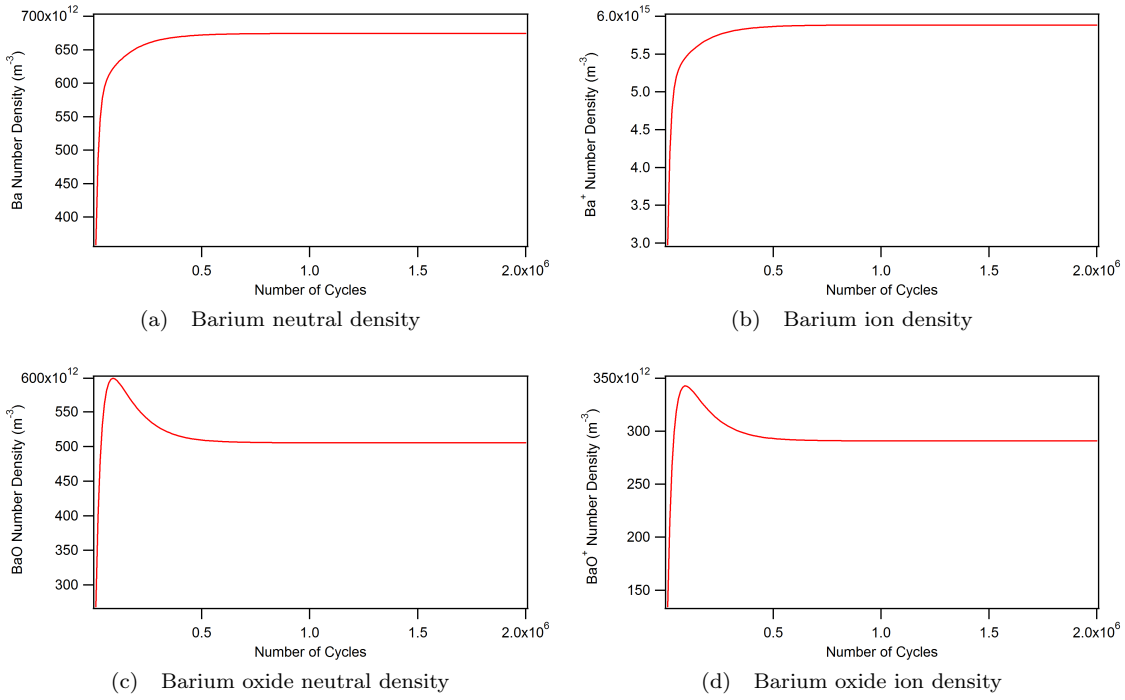

(a) Barium neutral density

(b) Barium ion density

(c) Barium oxide neutral density

(d) Barium oxide ion density

Figure 3.5.2: Barium number densities are shown for a cell in the computational mesh at $r = 0.1069$ cm, $z = 1.8643$ cm. The barium solution reaches equilibrium at approximately 5×10^5 cycles. This corresponds to 1.5 ms for a time step of $dt = 3\times10^{-9}$ s.

Barium neutral density contours and streamlines are shown in Fig. 3.5.4a. Barium neutrals are supplied from the emitter interior, evaporate from the emitter surface, and enter the discharge. Neutrals that are emitted from the insert at axial locations of $z < 1$ cm escape through the upstream inlet. (The barium thermal velocity at the cathode inlet is 440 m/s whereas the xenon flow velocity is 10 m/s.) However, neutrals emitted from the surface downstream of $z = 1$ cm are swept into the

ionization zone by the neutral xenon flow and are ionized before they can escape through the orifice exit. A low density region, which encompasses the last 10 mm of the insert, forms as a result of intense ionization of the barium. Recall from Fig. 3.4.2 that the barium ionization cross sections are large and the ionization potential is relatively low at 5.2 eV. The mean free path for barium ionization in this region is approximately 0.2 mm as shown in Fig. 3.5.3a. Note that the ionization region for barium coincides with the high plasma density region shown in Fig. 3.3.1d as expected.

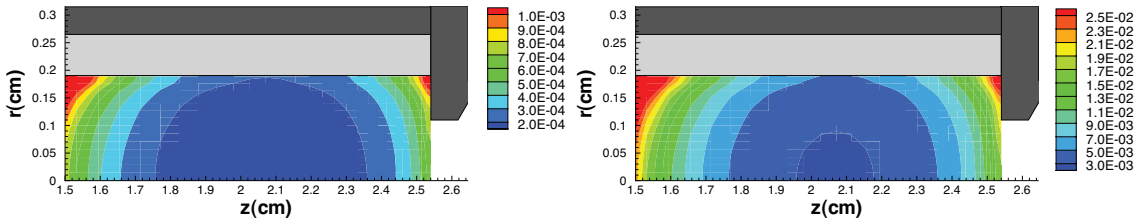

(a) Ba ionization mean free path, λ_{mfp} (m). (b) BaO ionization mean free path, λ_{mfp} (m).

Figure 3.5.3: Ionization mean free path, λ_{mfp} (m), for the 15 A, 3.7 sccm case.

Figure 3.5.4b shows the barium ion density contours and streamlines. There is a high flux of neutral barium from the emitter surface between $z = 1.3$ and 1.5 cm. Neutrals that leave the emitter in this region and flow toward the ionization zone are ionized in the periphery as shown by the yellow and light green area in Fig. 3.5.4b. The barium ions formed there are pushed back to the surface via the electric field.

BaO neutral density contours and streamlines are shown in Fig. 3.5.4c. BaO neutrals evaporate from the emitter, enter the discharge, and are pushed downstream by the xenon neutral gas flow. Note that BaO is not as readily ionized as Ba. The BaO ionization rate constant is approximately an order of magnitude lower than the rate constant for Ba ionization, and the ionization potential for BaO is 6.9 eV. Therefore, Fig. 3.5.4c shows that some BaO escapes ionization and exits the cathode through the orifice. Some BaO does get ionized and is transported back to the surface in the same way that barium ions are. Figure 3.5.4d shows the BaO ion density contours and streamlines. The BaO mean free path for ionization is approximately 3 mm as shown in Fig. 3.5.3b.

The terms in the expression for momentum conservation given in Eq. (3.3.17) are plotted in Fig. 3.5.5 along the axis of symmetry, i.e., for $r = 0$. In the solution for Ba^+ and BaO^+ shown in Figs. 3.5.5a and 3.5.5c, the two dominant terms are the electric field term and the xenon ion drag. The convective acceleration term, $nm(\mathbf{u} \cdot \nabla)u_z$, which appears on the left-hand side of Eq. (3.3.17) is much smaller than the other terms. Therefore, the assumption made previously to neglect this term in the transport model is justified.

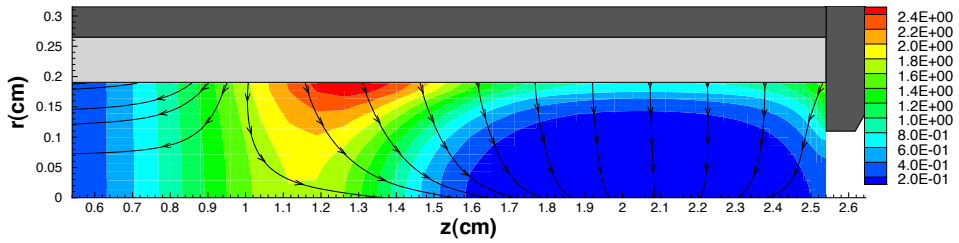

(a) Barium neutral density, n_{Ba} (10^{16} m^{-3}), and Ba streamlines.

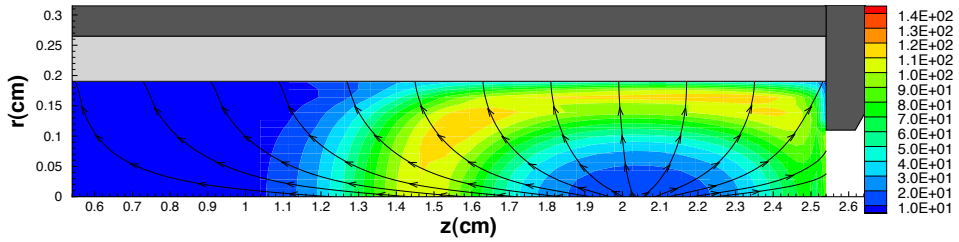

(b) Barium ion density, n_{Ba^+} (10^{14} m^{-3}), and Ba$^+$ streamlines.

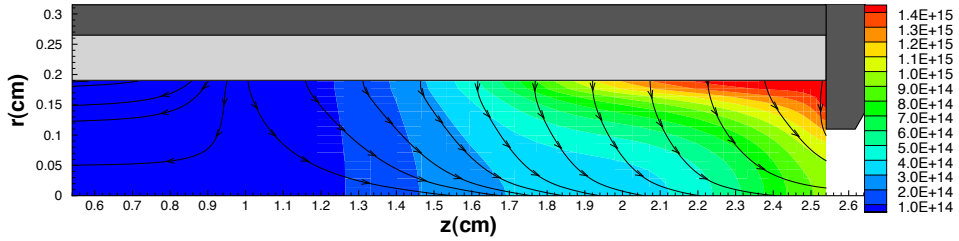

(c) Barium oxide neutral density, n_{BaO} (m^{-3}), and BaO streamlines.

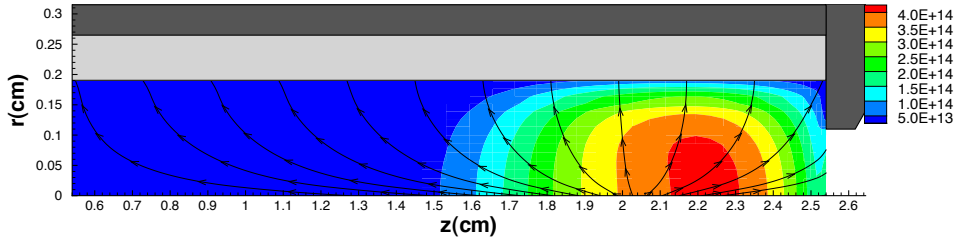

(d) Barium oxide ion density, n_{BaO^+} (m^{-3}), and BaO$^+$ streamlines.

Figure 3.5.4: Barium plasma solution for a discharge current of 15 A and a xenon flow rate of 3.7 sccm.

In the solution for neutral Ba and BaO shown in Figs. 3.5.5b and 3.5.5d, the xenon neutral drag and the pressure gradient are the two dominant terms throughout much of the discharge. The convective acceleration term dominates at the orifice where the velocities increase, but is small everywhere else in the discharge. For the purpose of this work, which is primarily to understand the dynamics that occur in the discharge upstream of the orifice, it appears safe to neglect this term.

In the BaO solution, the xenon ion drag term is also important and becomes large at axial locations near $z = 2$ cm. The plasma densities are high in this region, and since BaO has a high polarizability and a permanent dipole, the frequency for Xe^+–BaO collisions is probably high at these locations. Note that electron drag acting on BaO was not included in the model because of insufficient data to determine the reaction rate. The electron drag term was included in the Ba solution, but is small compared with the other terms in the momentum equation as seen in Fig. 3.5.5b. Although the reaction rate for electron momentum transfer is of the same order of magnitude as the other collision processes, the electron mass is so much smaller than the other species. Therefore, the electron-neutral collision frequency is too low to be significant and it is safe to neglect this term.

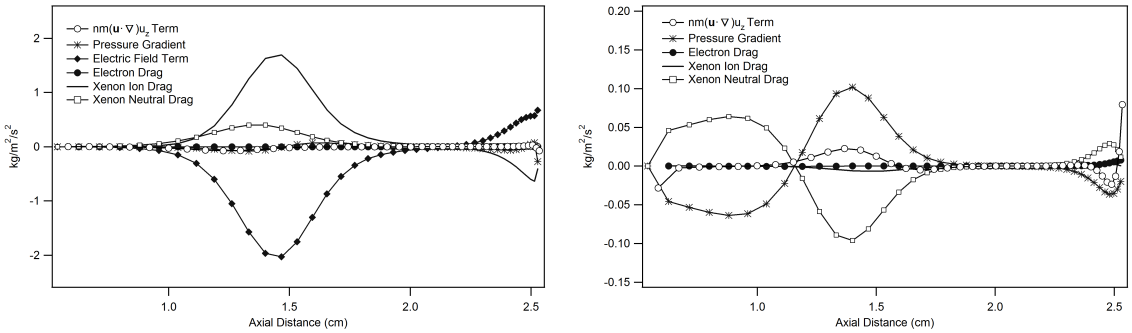

(a) Comparison of terms in the Ba^+ momentum equation (b) Comparison of terms in the Ba momentum equation

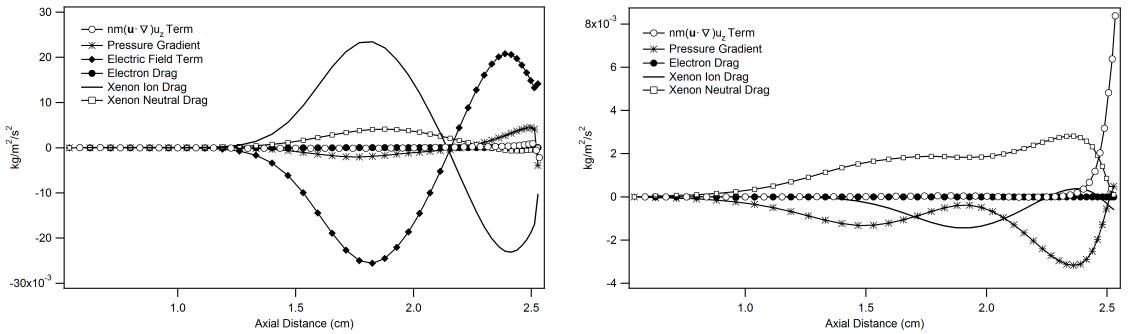

(c) Comparison of terms in the BaO^+ momentum equa-(d) Comparison of terms in the BaO momentum equation tion

Figure 3.5.5: Comparison of the terms in the momentum equation given in Eq. (3.3.17) along the axis of symmetry.

3.6 Transport Model with Oxygen Poisoning

The results of the transport model for cathode operation at 15 A, 3.7 sccm with oxygen poisoning at concentration levels of 100 ppm are presented here considering the following eight minor species: Ba, Ba^+, BaO, BaO^+, O_2, O_2^+, O, and O^+. Barium and barium oxide are introduced into the gas via vapor flow through the emitter pores, and Ba and BaO ions are generated via electron impact ionization. The oxygen densities are initially assumed to be zero everywhere. During poisoning, molecular oxygen is introduced into the xenon flow through the upstream inlet to the cathode at the xenon neutral velocity. The oxygen number density at the inlet is taken to be 100 ppm of the xenon neutral density. The xenon neutral gas flows into the cathode at a velocity of 10 m/s. For a domain length of 2 cm, it takes the oxygen 2 ms to fill the computational region.

The oxygen may charge exchange with xenon ions to form O_2^+ and may react with barium to form BaO, BaO^+, and O according to reactions (31)–(33) given in Table 3.1. Once in the discharge, the oxygen will deposit on the emitter surface until it is saturated and can no longer accumulate additional oxygen. This means that the emitter boundary conditions change over time from a largely absorbing surface to a nonabsorbing surface once steady state is reached. A detailed discussion of the emitter surface and the reaction kinetics that take place at the plasma-surface boundary during oxygen poisoning will be presented in Chapter 4.

Since the focus of this chapter is on the gas phase dynamics, the two bounding cases will be considered here. Two models of surface interaction for minor species are considered in order to bound the behavior. First, consider the case in which there is no accumulation of oxygen on the emitter surface—this case is referred to as the nonabsorbing boundary condition and will be discussed in §3.6.1. Second, consider that the emitter surface is perfectly absorbing, i.e., all oxygen ions and neutrals that reach the surface remain on the surface. In reality, some fraction of the oxygen ions and neutrals will stick onto the surface, i.e., be absorbed by the surface, and the remainder will reflect from the surface, i.e., not be absorbed. This case is referred to as the perfectly absorbing boundary condition and will be discussed in §3.6.2.

Equations (3.3.1) and (3.3.19) are solved for the eight minor species listed above. The collision processes included in Eq. (3.3.19) are momentum transfer collisions with electrons, xenon neutrals, and xenon ions. These processes correspond to reactions (1)–(24) of Table 3.1. Note that e–BaO and e–O momentum transfer collisions are not included here as there was insufficient data to determine the rate constant for these reactions. In the momentum equation for the other neutral species, the electron drag term is several orders of magnitude lower than the xenon drag terms, and therefore, it appears safe to neglect the electron drag term for collisions with BaO and O. Electron impact ionization of Ba and BaO, which corresponds to reactions (25) and (26) in Table 3.1, is included in the model. Electron impact ionization of O and O_2 are neglected since the rate constants are

several orders of magnitude lower than the ionization rate constants for Ba and BaO as shown in Fig. 3.4.3. Charge exchange collisions between Xe^+–O_2 and O_2^+–Xe, which correspond to reactions (29) and (30) in Table 3.1, are considered.

For both cases, barium atom and oxygen atom conservation must hold. Conservation of barium atoms in the discharge plasma is described by

$$\dot{n}_{Ba} + \dot{n}_{Ba^+} + \dot{n}_{BaO} + \dot{n}_{BaO^+} = 0. \tag{3.6.1}$$

Conservation of oxygen atoms in the discharge plasma is described by

$$\dot{n}_O + \dot{n}_{O^+} + 2\dot{n}_{O_2} + 2\dot{n}_{O_2^+} + \dot{n}_{BaO} + \dot{n}_{BaO^+} = 0. \tag{3.6.2}$$

The generation terms are expressed as

$$\begin{aligned}
\dot{n}_{Ba} &= -n_{Ba}n_e\kappa_{25} - n_{Ba}n_{O_2}\kappa_{31} - n_{Ba}n_{O_2^+}\kappa_{33}, && (3.6.3)\\
\dot{n}_{Ba^+} &= n_{Ba}n_e\kappa_{25} - n_{Ba^+}n_{O_2}\kappa_{32}, && (3.6.4)\\
\dot{n}_{BaO} &= -n_{BaO}n_e\kappa_{26} + n_{Ba}n_{O_2}\kappa_{31}, && (3.6.5)\\
\dot{n}_{BaO^+} &= n_{BaO}n_e\kappa_{26} + n_{Ba^+}n_{O_2}\kappa_{32} + n_{Ba}n_{O_2^+}\kappa_{33}, && (3.6.6)\\
\dot{n}_{O_2} &= -n_{O_2}n_e\kappa_{29} + n_{O_2^+}n_{Xe}\kappa_{30} - n_{Ba}n_{O_2}\kappa_{31} - n_{Ba^+}n_{O_2}\kappa_{32}, && (3.6.7)\\
\dot{n}_{O_2^+} &= n_{O_2}n_e\kappa_{29} - n_{O_2^+}n_{Xe}\kappa_{30} - n_{Ba}n_{O_2^+}\kappa_{33}, && (3.6.8)\\
\dot{n}_O &= n_{Ba}n_{O_2}\kappa_{31} + n_{Ba^+}n_{O_2}\kappa_{32} + n_{Ba}n_{O_2^+}\kappa_{33}, && (3.6.9)\\
\dot{n}_{O^+} &= 0, && (3.6.10)
\end{aligned}$$

where the subscripts on the rate constant, κ, refer to the reaction number in Table 3.1.

3.6.1 Case A: Emitter Surface is Nonabsorbing

The results of the transport model for the case where nonabsorbing boundary conditions for oxygen are imposed at the emitter surface are presented here. The boundary conditions for Ba, Ba^+, BaO, and BaO^+ are the same in this case as those presented in §3.5.1. The oxygen boundary conditions are summarized below.

Upstream inlet to the cathode. In order to model an oxygen concentration of 100 ppm, it is assumed that O_2 enters the plasma control volume through the upstream inlet at the neutral xenon velocity and that the O_2 flux at this boundary is four orders of magnitude lower than the xenon neutral flux:

$$\mathbf{\Gamma}_{O_2} = 100 \times 10^{-6}\, \Gamma_{Xe}\, \hat{\mathbf{z}}. \tag{3.6.11}$$

O, O^+, and O_2^+ are generated inside the plasma discharge and are assumed to flow out of the plasma control volume through this boundary at the thermal velocity. The net fluxes at this boundary are therefore given by

$$\mathbf{\Gamma}_O = -\frac{n_O}{4}\left(\frac{8kT_h}{\pi m_O}\right)^{1/2}\hat{\mathbf{z}}, \tag{3.6.12}$$

$$\mathbf{\Gamma}_{O^+} = -\frac{n_{O^+}}{4}\left(\frac{8kT_h}{\pi m_O}\right)^{1/2}\hat{\mathbf{z}}, \tag{3.6.13}$$

$$\mathbf{\Gamma}_{O_2^+} = -\frac{n_{O_2^+}}{4}\left(\frac{8kT_h}{\pi m_{O_2}}\right)^{1/2}\hat{\mathbf{z}}. \tag{3.6.14}$$

Emitter surface and orifice plate. Both the emitter surface and orifice plate are assumed to be in steady state so that no particles are allowed to accumulate on these surfaces. Ions leave the plasma control volume and strike these surfaces at the Bohm velocity. The ions then recombine at the surface and leave as neutrals—no ions are released from these surfaces back into the gas. The net ion fluxes at the emitter surface boundary are

$$\mathbf{\Gamma}_{O^+} = n_{O^+}\left(\frac{kT_e}{m_O}\right)^{1/2}\hat{\mathbf{r}}, \tag{3.6.15}$$

$$\mathbf{\Gamma}_{O_2^+} = n_{O_2^+}\left(\frac{kT_e}{m_{O_2}}\right)^{1/2}\hat{\mathbf{r}}, \tag{3.6.16}$$

and the net ion fluxes at the orifice plate boundary are

$$\mathbf{\Gamma}_{O^+} = n_{O^+}\left(\frac{kT_e}{m_O}\right)^{1/2}\hat{\mathbf{z}}, \tag{3.6.17}$$

$$\mathbf{\Gamma}_{O_2^+} = n_{O_2^+}\left(\frac{kT_e}{m_{O_2}}\right)^{1/2}\hat{\mathbf{z}}. \tag{3.6.18}$$

Since the surfaces are in steady state, the total flux of atomic and molecular oxygen must be zero at the surfaces, i.e.,

$$\mathbf{\Gamma}_O + \mathbf{\Gamma}_{O^+} = 0, \tag{3.6.19}$$

$$\mathbf{\Gamma}_{O_2} + \mathbf{\Gamma}_{O_2^+} = 0. \tag{3.6.20}$$

Therefore, the net neutral fluxes at these surfaces are

$$\mathbf{\Gamma}_O = -\mathbf{\Gamma}_{O^+}, \tag{3.6.21}$$

$$\mathbf{\Gamma}_{O2} = -\mathbf{\Gamma}_{O_2^+}. \tag{3.6.22}$$

Entrance to cathode orifice. It is assumed that all neutrals flow out of the plasma control volume through the cathode orifice at the xenon neutral velocity and that all ions flow out of plasma

control volume at the xenon ion velocity. Therefore, the fluxes at this boundary are given by

$$\mathbf{\Gamma}_O = n_O u_{Xe}\,\hat{\mathbf{z}}, \tag{3.6.23}$$

$$\mathbf{\Gamma}_{O^+} = n_{O^+} u_{Xe^+}\,\hat{\mathbf{z}}, \tag{3.6.24}$$

$$\mathbf{\Gamma}_{O_2} = n_{O_2} u_{Xe}\,\hat{\mathbf{z}}, \tag{3.6.25}$$

$$\mathbf{\Gamma}_{O_2^+} = n_{O_2^+} u_{Xe^+}\,\hat{\mathbf{z}}. \tag{3.6.26}$$

Centerline. This is a symmetry boundary and the ion and neutral fluxes are set to zero:

$$\mathbf{\Gamma}_{O^+} = \mathbf{\Gamma}_O = 0\,\hat{\mathbf{r}}, \tag{3.6.27}$$

$$\mathbf{\Gamma}_{O_2^+} = \mathbf{\Gamma}_{O_2} = 0\,\hat{\mathbf{r}}. \tag{3.6.28}$$

Case A results. The solution to the transport model assuming nonabsorbing boundary conditions at the emitter surface is shown in Figs. 3.6.1–3.6.3. The ion and neutral density contours for barium and barium oxide are shown in Fig. 3.6.1. These solutions are unchanged from the results presented in §3.5 with no oxygen. The dominant process for producing BaO^+ is via electron impact ionization of BaO. Very little BaO^+ is generated by reactions between barium and oxygen as the densities of these species are relatively low.

O_2 density contours and streamlines are shown in Fig. 3.6.2a. The oxygen enters the domain through the upstream inlet and is pushed downstream by the xenon neutral gas flow where it exits through the orifice. Note the similarity between the O_2 neutral density contours shown here and the Xe neutral density contours shown in Fig. 3.3.1a. The results show that the O_2 neutral density is everywhere about four orders of magnitude lower than the Xe neutral density, which is consistent with the prescribed oxygen concentration of 100 ppm at the cathode inlet. The density decreases near the downstream end of the computational region as neutrals exit through the orifice or become ionized.

Figure 3.6.2b shows the O_2^+ density contours and streamlines. Since the only mechanism for O_2 ionization considered in the model is charge exchange with Xe^+, the ionization rate depends on the plasma density and heavy particle temperature. The results show that the high O_2^+ density region between $z = 1.9$ and 2.2 cm coincides with the high plasma density region as shown in Fig. 3.3.1d as expected. The mean free path for O_2 ionization is approximately 15 mm in this region as shown in Fig. 3.6.3. The ions generated in this zone are transported back toward the insert via the electric field. Ions that hit the emitter surface recombine and leave the surface as neutrals. This process accounts for the streamlines originating at the emitter surface in Fig. 3.6.2a.

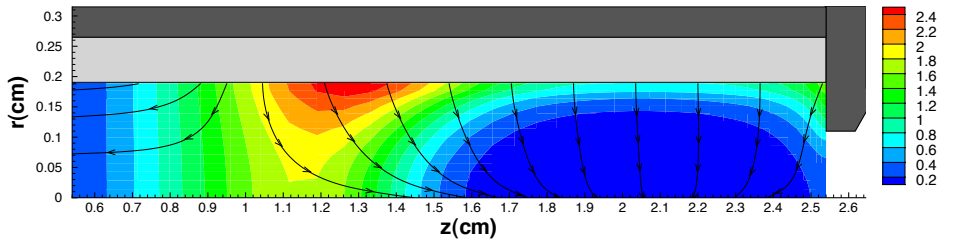

(a) Barium neutral density, n_{Ba} (10^{16} m^{-3}), and Ba streamlines.

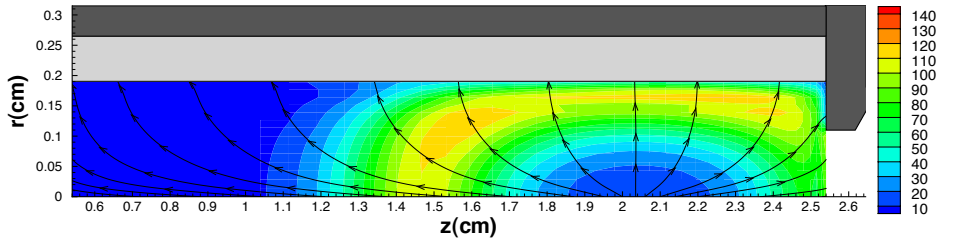

(b) Barium ion density, n_{Ba^+} (10^{14} m^{-3}), and Ba$^+$ streamlines.

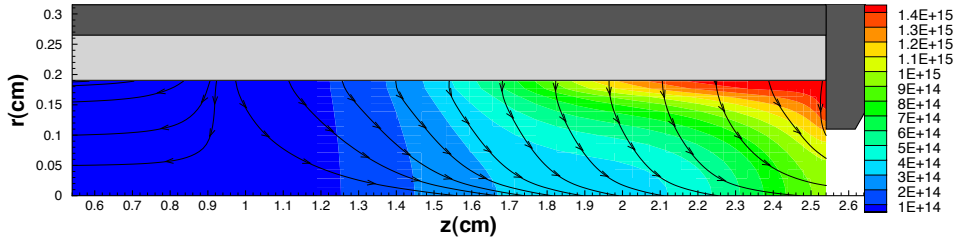

(c) Barium oxide neutral density, n_{BaO} (m^{-3}), and BaO streamlines.

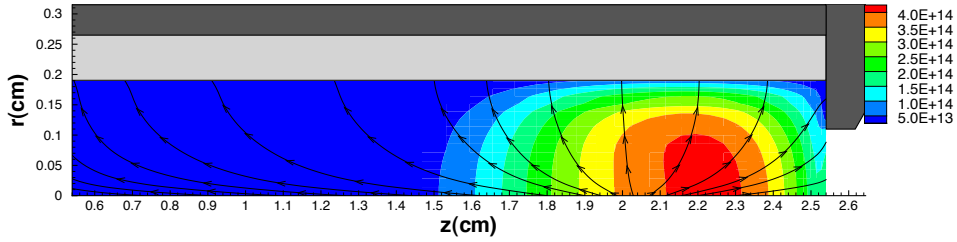

(d) Barium oxide ion density, n_{BaO^+} (m^{-3}), and BaO$^+$ streamlines.

Figure 3.6.1: Ba and BaO solution for oxygen poisoning of 100 ppm with nonabsorbing boundary conditions. $J_D = 15$ A, $\dot{m}_{Xe} = 3.7$ sccm.

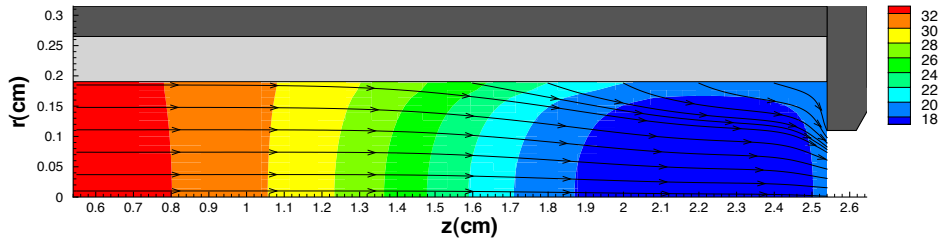

(a) Molecular oxygen neutral density, n_{O_2} (10^{16} m^{-3}), and O_2 streamlines.

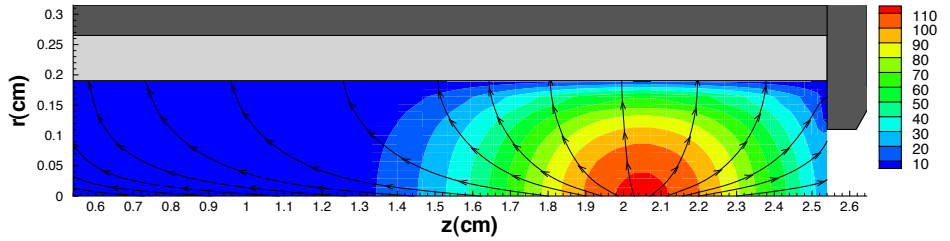

(b) Molecular oxygen ion density, $n_{O_2^+}$ (10^{14} m^{-3}), and O_2^+ streamlines.

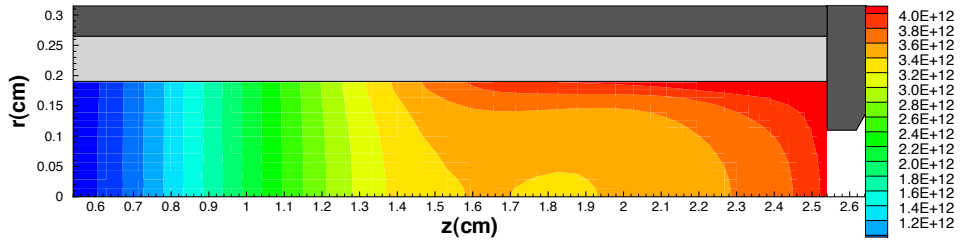

(c) Atomic oxygen neutral density, n_O (m^{-3}).

Figure 3.6.2: Oxygen solution for oxygen poisoning of 100 ppm with nonabsorbing boundary conditions. $J_D = 15$ A, $\dot{m}_{Xe} = 3.7$ sccm.

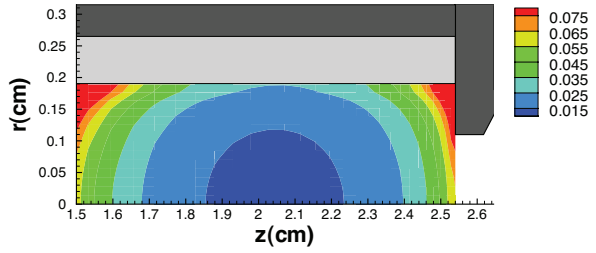

Figure 3.6.3: O_2 ionization mean free path, λ_{mfp} (m), for the 15 A case.

Figure 3.6.2c shows the density contours for atomic oxygen. The number density for O is about five orders of magnitude lower than the number density for O_2. Since dissociation of molecular oxygen was neglected in this model, the only way to generate atomic oxygen is via reactions between barium and oxygen as discussed in §3.4.5.

The number density of each minor species in the plasma is plotted as a function of axial distance along the emitter surface in Fig. 3.6.4. In this case, in which no species are permitted to accumulate on the surface, the oxygen fills the discharge and reaches an equilibrium value that is relatively constant throughout the computational region. The densities of all other minor species are small compared with the O_2 neutral density, which is about four orders of magnitude lower than the Xe neutral density and an order of magnitude larger than the Ba neutral density.

The terms in the expression for momentum conservation given in Eq. (3.3.17) are plotted in Fig. 3.6.5 along the axis of symmetry, i.e., for $r = 0$. In the solution for neutral O_2 and O shown in Figs. 3.6.5a and 3.6.5c, the xenon neutral drag and the pressure gradient are the two dominant terms throughout much of the discharge. The convective acceleration term dominates at the orifice where the velocities increase, but is small everywhere else in the discharge. In the O_2 solution, the electron drag becomes important as we approach the orifice. In the solution for O_2^+ shown in Fig. 3.6.5b, the two dominant terms are the electric field term and the xenon ion drag, and the convective acceleration term is much smaller than the other terms.

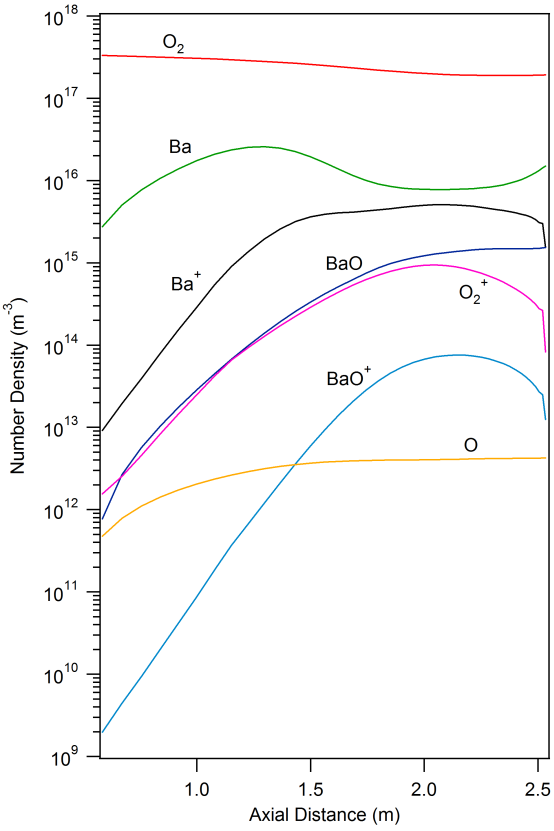

Figure 3.6.4: Number density as a function of axial distance near the emitter surface.

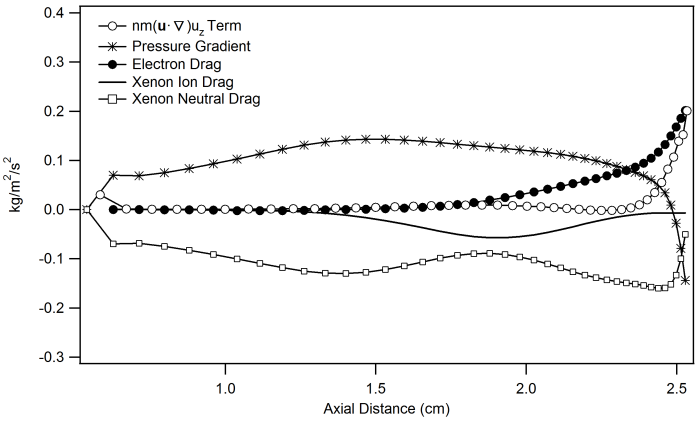

(a) O_2 momentum equation: nonabsorbing case.

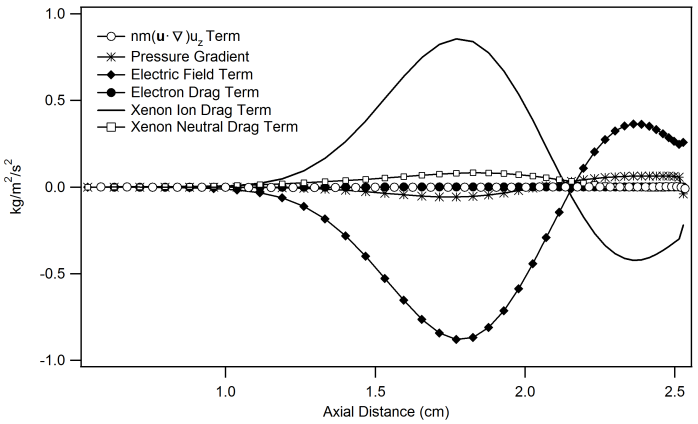

(b) O_2^+ momentum equation: nonabsorbing case.

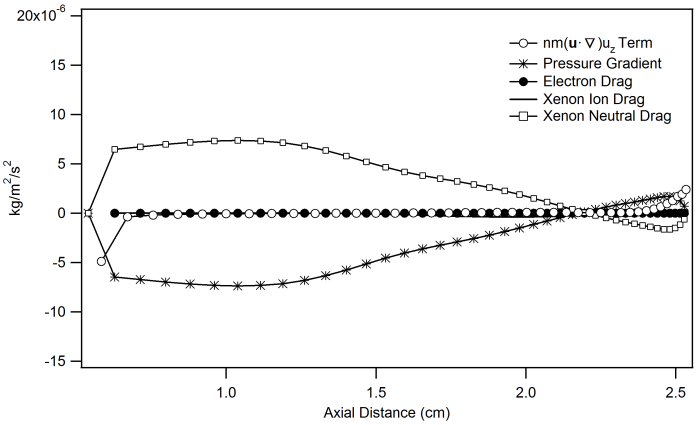

(c) O momentum equation: nonabsorbing case.

Figure 3.6.5: Comparison of the terms in the momentum equation given in Eq. (3.3.17) along the axis of symmetry asssuming nonabsorbing boundary conditions at the emitter surface.

3.6.2 Case B: Emitter Surface is Perfectly Absorbing

The results of the transport model for the case where perfectly absorbing boundary conditions are imposed at the emitter surface are presented here. The boundary conditions for the upstream inlet, orifice plate, orifice entrance, and centerline are the same in this case as those presented in the nonabsorbing case. Equations (3.6.11)–(3.6.14) and Eqs. (3.6.17)—(3.6.28) apply for these surfaces. The emitter surface is no longer assumed to be in steady state, and any oxygen that strikes the surface is allowed to accumulate on the surface without bound. Oxygen ions leave the plasma control volume and strike the emitter surface at the Bohm velocity. The ions are completely absorbed by the surface, and none are released back into the plasma. Therefore, the net ion fluxes at the emitter surface boundary are the same as those given in Eqs. (3.6.15) and (3.6.16).

Oxygen neutrals are assumed to leave the plasma control volume and strike the emitter surface at the thermal velocity. The neutrals are completely absorbed by the surface, and therefore, the net neutral fluxes at the emitter surface boundary are

$$\mathbf{\Gamma}_O = \frac{n_O}{4}\left(\frac{8kT_h}{\pi m_O}\right)^{1/2}\hat{\mathbf{r}}, \tag{3.6.29}$$

$$\mathbf{\Gamma}_{O_2} = \frac{n_{O_2}}{4}\left(\frac{8kT_h}{\pi m_{O_2}}\right)^{1/2}\hat{\mathbf{r}}. \tag{3.6.30}$$

Case B results. The solution to the transport model with 100 ppm of oxygen poisoning is shown in Figs. 3.6.6 and 3.6.7. The ion and neutral density contours for barium and barium oxide are shown in Fig. 3.6.6 and are unchanged from the results presented in §3.6.1 and §3.5.

O_2 density contours and streamlines are shown in Fig. 3.6.7a. The oxygen enters the domain through the upstream inlet and is pushed downstream by the xenon neutral gas flow. The radial gradient in the density creates a diffusion flux that transports the oxygen toward the emitter surface where it is absorbed. Along the length of the emitter, the O_2 densities vary by four orders of magnitude. This steep axial density gradient results because the upstream end of the insert acts like an oxygen getter, i.e., perfect absorber. The O_2 neutral flux to the surface is very high at the upstream end and rapidly drops off with distance as shown in Fig. 3.6.8. O_2 ion fluxes to the surface are at least two orders of magnitude lower than the O_2 neutral fluxes.

O_2^+ density contours and streamlines are shown in Fig. 3.6.7b. Recall from Fig. 3.6.3 that the oxygen ionization mean free path is lowest in the region between $z = 1.9$ and 2.2 cm. However, since O_2 neutral densities are so low there not much ionization takes place, thus moving the high ion density region further upstream. To illustrate this, Fig. 3.6.9 compares the ionization frequency, number densities, and ion generation rate along the centerline of the computational region.

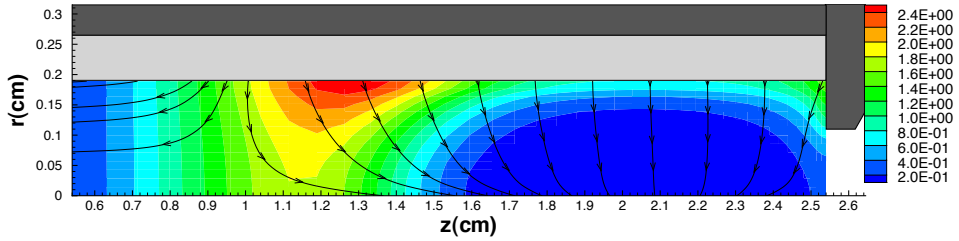

(a) Barium neutral density, n_{Ba} (10^{16} m^{-3}), and Ba streamlines.

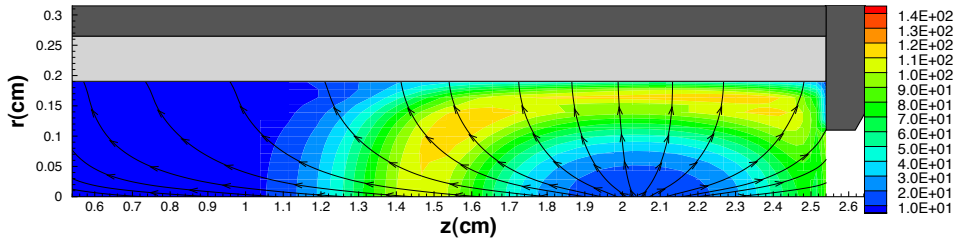

(b) Barium ion density, n_{Ba^+} (10^{14} m^{-3}), and Ba$^+$ streamlines.

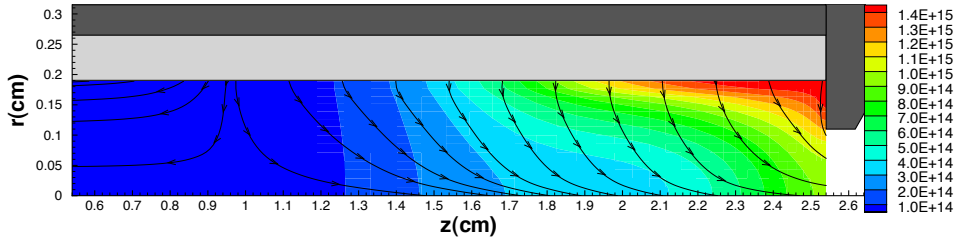

(c) Barium oxide neutral density, n_{BaO} (m^{-3}), and BaO streamlines.

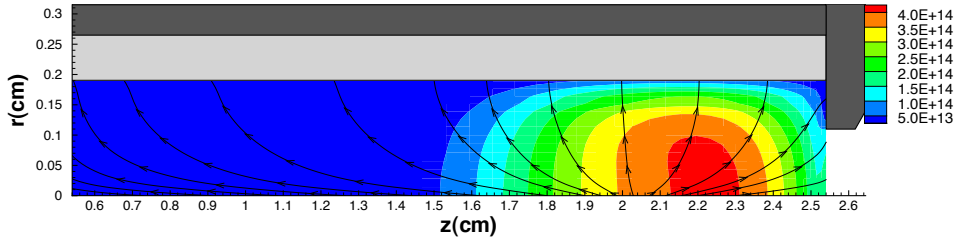

(d) Barium oxide ion density, n_{BaO^+} (m^{-3}), and BaO$^+$ streamlines.

Figure 3.6.6: Ba and BaO solution for oxygen poisoning of 100 ppm with absorbing boundary conditions. $J_D = 15$ A, $\dot{m}_{Xe} = 3.7$ sccm.

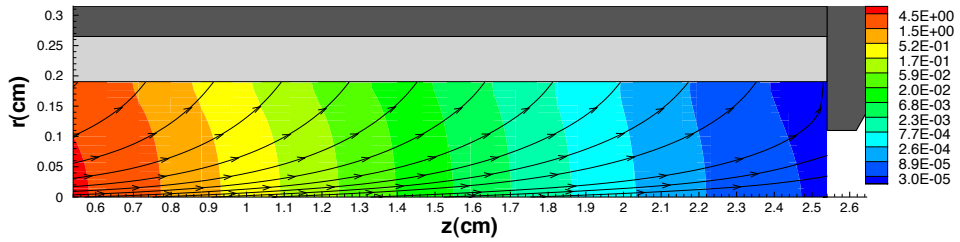

(a) Molecular oxygen neutral density, n_{O_2} (10^{16} m^{-3}), and O_2 streamlines.

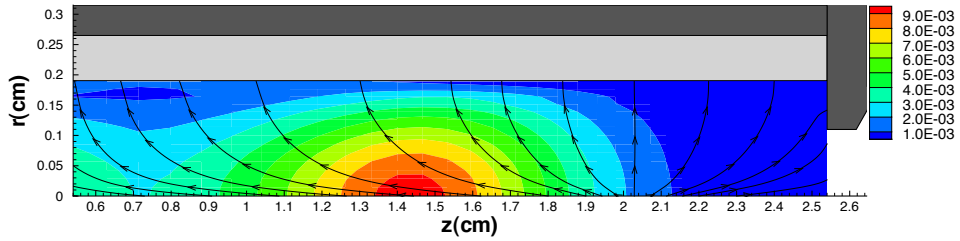

(b) Molecular oxygen ion density, $n_{O_2^+}$ (10^{14} m^{-3}), and O_2^+ streamlines.

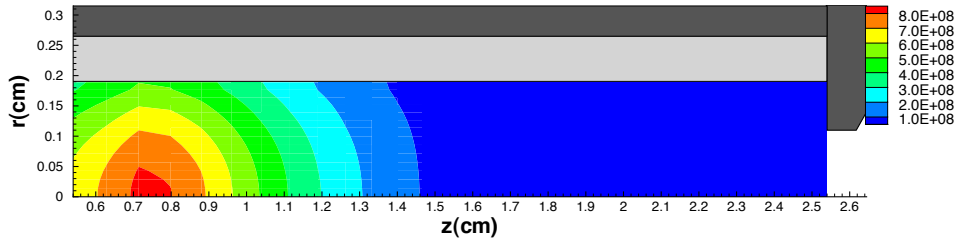

(c) Atomic oxygen neutral density, n_O (m^{-3}).

Figure 3.6.7: Oxygen solution for oxygen poisoning of 100 ppm with absorbing boundary conditions. $J_D = 15$ A, $\dot{m}_{Xe} = 3.7$ sccm.

The O_2 ionization frequency is calculated using $\nu_{iz} = n_e \kappa_{29}$, where n_e and T_h are extracted from the xenon plasma solution. The ion generation rate was calculated by taking the product of the the ionization frequency and the O_2 density. The values are scaled by their maximum value to provide a better visual comparison of the parameters. The O_2 density is plotted on a log scale on the right axis. The results show that most of the ions are generated in the region between $z = 1.3$ and 1.6 cm, accounting for the high density of O_2^+ there.

Figure 3.6.7c shows the density contours for atomic oxygen. Since dissociation of molecular oxygen was neglected in this model, the only way to generate atomic oxygen is via reactions between barium and oxygen as discussed in §3.4.5. Consequently, the highest density of O is near the inlet where the O_2 number density is highest.

The number density of each minor species in the plasma is plotted as a function of axial distance along the emitter surface in Fig. 3.6.10. In this case, oxygen is constantly absorbed by the upstream

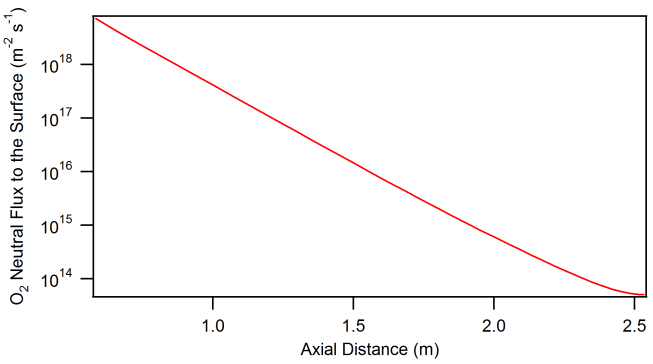

Figure 3.6.8: Plot of the O_2 neutral flux to the emitter surface along the length of the cathode.

portion of the emitter. This prevents oxygen from completely filling the discharge chamber as we saw previously in the nonabsorbing case. There is a strong gradient in the O_2 number density along the length of the emitter, and the densities of O and O_2^+ also drop with axial distance. The barium species are most dominant in the cathode for this case.

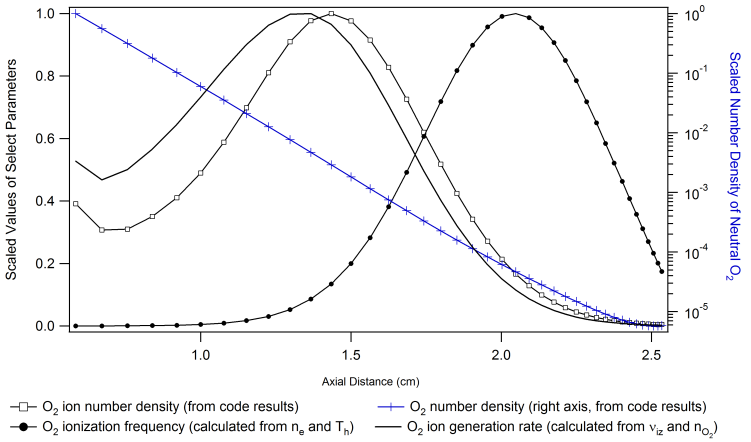

Figure 3.6.9: Plot of scaled values of oxygen density, ionization frequency, and ionization generation rate.

The terms in the expression for momentum conservation are plotted in Fig. 3.6.11 along the axis of symmetry, i.e., for $r = 0$. In the solution for neutral O_2 and O shown in Figs. 3.6.11a and 3.6.11c, the xenon neutral drag and the pressure gradient are the two dominant terms throughout much of the discharge. These terms are most dominant at the upstream end as this is where the oxygen densities are highest. In the solution for O_2^+ shown in Fig. 3.6.11b, the two dominant terms are the electric field term and the xenon ion drag. Xenon neutral drag is important upstream because of charge exchange collisions. The convective acceleration term is small everywhere for all three solutions.

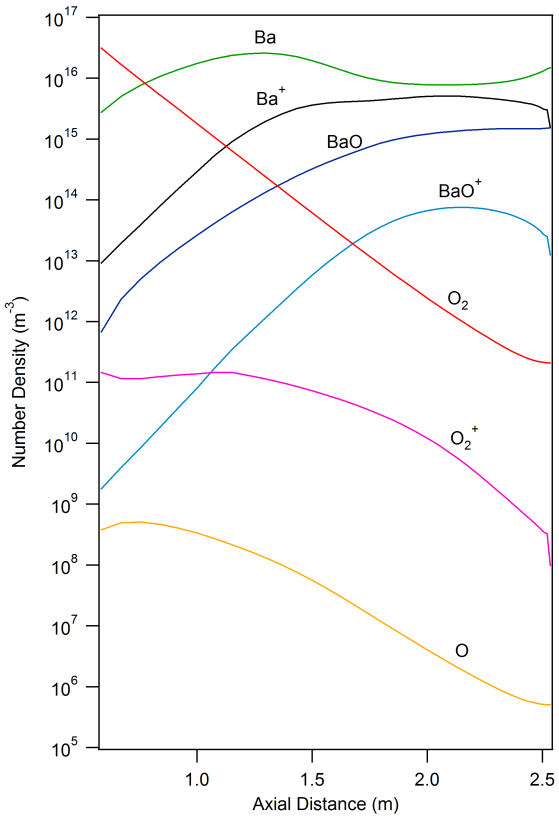

Figure 3.6.10: Number density as a function of axial distance near the emitter surface.

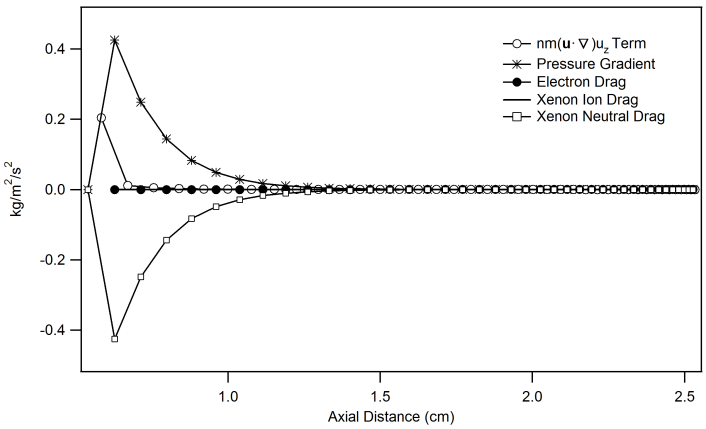

(a) O_2 momentum equation: perfectly absorbing case.

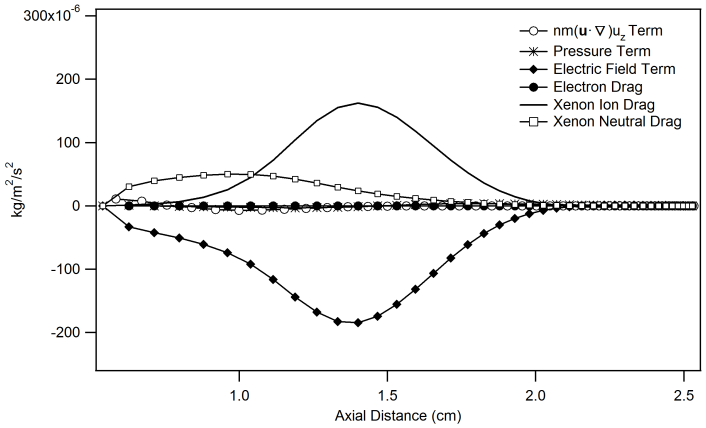

(b) O_2^+ momentum equation: perfectly absorbing case.

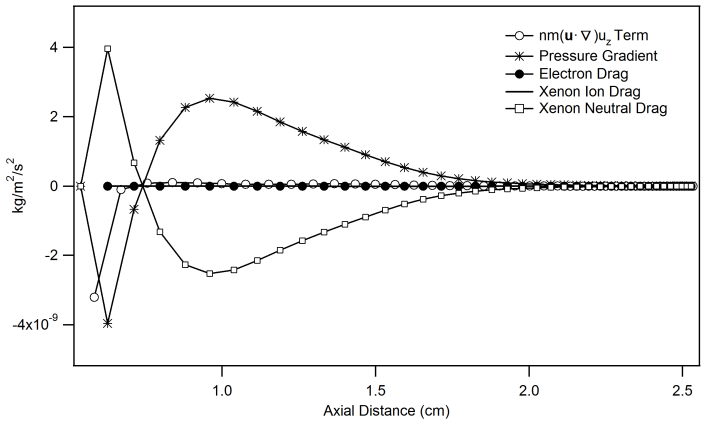

(c) O momentum equation: perfectly absorbing case.

Figure 3.6.11: Comparison of the terms in the momentum equation given in Eq. (3.3.17) along the axis of symmetry asssuming perfectly absorbing boundary conditions at the emitter surface.

3.7 Conclusions

The results presented here show the dynamics of barium and oxygen species in the xenon plasma as described by the conservation equations. Ba and BaO move through the emitter pores and escape into the plasma where they are ionized and transported back to the surface via the electric field. As a result of its low ionization potential, barium is readily ionized in the emission zone, and very few barium neutrals escape through the orifice. Through this process, barium is replenished to the emitter surface through the gas phase. BaO is not as effectively recycled since its ionization rates are higher and a non-negligible amount of BaO is allowed to escape through the orifice.

During poisoning, oxygen was allowed to enter the plasma discharge through the upstream inlet. The dominant ionization process for O_2 molecules was resonant charge exchange with Xe^+. The oxygen was also allowed to interact with Ba to form BaO; however, since the reactant concentrations were small, very little barium oxide was formed as a result of such chemical reactions. Dissociation of O_2 was not considered as the bond energy of molecular oxygen is high and dissociation cross sections are low. Therefore, atomic oxygen is generated only during reactions between O_2 and Ba, and consequently, the O number densities are very small.

In order to understand the transport of oxygen species in the cathode, two bounding cases were explored. The first case assumed no oxygen accumulation on the emitter surface. This boundary condition gives a uniform O_2 neutral density at the prescribed concentration throughout the entire domain. Not much of the neutral O_2 population is lost to ionization as the O_2^+ density is more than two orders of magnitude lower than the O_2 density. This result is significant as it shows that oxygen is not effectively recycled in the plasma. All neutrals that escape ionization exit the cathode through the orifice. The model also shows that the oxygen flux to the surface is not diffusion limited.

The second type of boundary condition for oxygen assumed the emitter to be a perfectly absorbing surface. This case is representative of what would occur early on in oxygen poisoning. The results give a steep gradient in the O_2 density with axial distance as a result of significant oxygen gettering upstream. Although the temperatures and plasma densities are highest in the emission zone, the O_2 density is so low there that not much ionization takes place and the region of maximum O_2^+ density occurs further upstream. The results show that the pressure gradient is balanced by the xenon drag in the neutral species momentum equation, and the electric field term is balanced by the ion drag in the ion species momentum equation.

The results of these two bounding cases aid in understanding the dynamics of oxygen poisoning in the plasma discharge. In reality, the boundary conditions at the emitter surface will evolve in time beginning with a perfectly absorbing surface to a saturated state in which no further oxygen accumulation can occur. In order to better understand oxygen poisoning in these cathodes, a detailed analysis of the emitter surface is necessary and is the focus of the next chapter.

Bibliography

[1] J. Polk, I. Mikellides, and I. Katz, "Dynamics of barium flow in hollow cathode plasmas," in *JANNAF MSS/LPS/SPS Meeting*, Orlando, FL, 2008.

[2] J. Polk, I. Mikellides, A. Capece, and I. Katz, "Barium depletion in hollow cathode emitters," in *45th AIAA Joint Propulsion Conference*, Denver, CO, 2009, AIAA-2009-5197.

[3] J. Polk, I. Mikellides, I. Katz, and A. Capece, "Tungsten and barium transport in the internal plasma of hollow cathodes," *J. Appl. Phys.*, vol. 105, p. 113301, 2009.

[4] I. Mikellides, I. Katz, D. Goebel, and J. Polk, "Hollow cathode theory and experiment. II. A two-dimensional theoretical model of the emitter region," *J. Appl. Phys.*, vol. 98, p. 113303, 2005.

[5] I. Mikellides, February 2012, Jet Propusion Laboratory.

[6] I. Mikellides, I. Katz, and D. Goebel, "Numerical simulation of the hollow cathode discharge plasma dynamics," in *29th International Electric Propulsion Conference*, Princeton, NJ, 2005, IEPC-2005-200.

[7] E. McDaniel, *Collision Phenomena in Ionized Gases.* John Wiley & Sons, 1964.

[8] H. Shimamori and Y. Hatano, "Thermal electron attachment to O_2 in the presence of various compounds as studied by a microwave cavity technique combined with pulse radiolysis," *Chem. Phys.*, vol. 21, no. 2, pp. 187–201, 1977.

[9] W. G. Vincenti and C. H. Kruger, *Introduction to Physical Gas Dynamics.* John Wiley & Sons, 1965.

[10] R. G. Jahn, *Physics of Electric Propulsion.* Dover Publications, 2006.

[11] O. Kashireninov, V. Kuznetsov, and G. Manelis, "Kinetics of alkaline-earth atoms reactions with molecular oxygen," *AIAA J.*, vol. 15, no. 7, pp. 1035–1037, 1977.

[12] K. Itikawa and A. Ichimura, "Cross sections for collisions of electrons and photons with atomic oxygen," *J. Phys. Chem. Ref. Data*, vol. 19, no. 3, pp. 637–651, 1990.

[13] K. Itikawa, "Cross sections for electron collisions with oxygen molecules," *J. Phys. Chem. Ref. Data*, vol. 38, no. 1, pp. 1–20, 2009.

[14] D. V. Fursa and I. Bray, "Calculation of electron scattering from the ground state of barium," *Phys. Rev. A*, vol. 59, no. 1, pp. 282–294, 1999.

[15] J. Huba, "NRL plasma formulary," Beam Physics Branch, Plasma Physics Division, Naval Research Laboratory, Washington, DC 20375.

[16] B. Poling, J. Prausnitz, and J. O'Connell, *The Properties of Gases and Liquids*, 5th ed. McGraw-Hill, 2001.

[17] K. Annamalai and I. K. Puri, *Advanced Thermodynamics Engineering*. CRC Press, 2002.

[18] T. G. Walker, K. D. Bonin, and W. Happer, "Modulation technique for measuring diffusion coefficients of Ba in noble gases," *J. Chem. Phys.*, vol. 87, no. 1, pp. 660–663, 1987.

[19] S. Kwon, J. Hwang, H. Lee, and W. R. Lee, "Interactive CO_2 adsorption on the BaO (100) surface: A density functional theory (DFT) study," *Bull. Korean Chem. Soc.*, vol. 31, no. 8, pp. 2219–2222, 2010.

[20] S. Batsanov, "Van der Waals radii of the elements," *Inorganic Materials*, vol. 37, no. 9, pp. 871–885, 2001.

[21] C. W. Carter and R. M. Sweet, *Macromolecular Crystallography, Volume 374, Part 4*. Gulf Professional Publishing, 2003.

[22] A. Fridman, *Plasma Chemistry*. Cambridge University Press, 2008.

[23] M. Lieberman and A. Lichtenberg, *Principles of Plasma Discharges and Materials Processing*. John Wiley & Sons, 1994.

[24] T. Su and M. T. Bowers, "Ion-polar molecule collisions: The effect of ion size on ion-polar molecule rate constants; The parameterization of the average-dipole-orientation theory," *Inter. J. Mass Spec. and Ion Phys.*, vol. 12, pp. 347–356, 1973.

[25] C. Bamford and C. Tipper, Eds., *Comprehensive Chemical Kinetics: Selected Elementary Reactions*. Elsevier Science Publishing Co., 1976.

[26] "NIST chemistry webbook," 2011, retrieved Jan 2012. [Online]. Available: http://webbook.nist.gov/chemistry

[27] D. Lide, *CRC Handbook of Chemistry and Physics*, 85th ed. CRC Press, 2004.

[28] R. Rejoub, B. Lindsay, and R. Stebbings, "Determination of the absolute partial and total cross sections for electron-impact ionization of the rare gases," *Phys. Rev. A*, vol. 65, p. 042713, 2002.

[29] J. Dettmann and F. Karstensen, "Absolute ionisation functions for electron impact with barium," *J. Phys. B: At. Mol. Phys.*, vol. 15, pp. 287–300, 1982.

[30] J. Hastie, D. Bonnell, and P. Schenck, "Development and application of very high temperature mass spectrometry. Vapor pressure determinations over liquid refractories," *Pure Appl. Chem.*, vol. 72, no. 11, pp. 2111–2126, 2000.

[31] J. Hastie, "A predictive ionization cross-section model for inorganic molecules," NISTIR 6768, 2001.

[32] W. Thompson, M. Shah, and H. Gilbody, "Single and double ionization of atomic oxygen by electron impact," *J. Phys. B: At. Mol. Opt. Phys.*, vol. 28, pp. 1321–1330, 1995.

[33] D. Rapp and P. Englander-Golden, "Total cross sections for ionization and attachment in gases by electron impact. I. Positive ionization," *J. Chem. Phys.*, vol. 43, p. 1464, 1965.

[34] R. F. Stebbings, B. R. Turner, and A. C. H. Smith, "Charge transfer in oxygen, nitrogen, and nitric oxide," *J. Chem. Phys.*, vol. 38, no. 9, pp. 2277–2279, 1963.

[35] D. Rapp and W. E. Francis, "Charge exchange between gaseous ions and atoms," *J. Chem. Phys.*, vol. 37, no. 11, pp. 2631–2645, 1962.

[36] J. S. Miller, S. H. Pullins, D. J. Levandier, Y. hui Chiu, and R. A. Dressler, "Xenon charge exchange cross sections for electrostatic thruster models," *J. Appl. Phys.*, vol. 91, no. 3, pp. 984–991, 2002.

[37] N. Kobayashi, "Low energy ion-neutral reactions. VI. $Ar^+ + Ar$, $N_2^+ + N_2$, $O_2^+ + O_2$, $CO^+ + CO$," *J. Phys. Soc. Japan*, vol. 38, no. 2, pp. 519–523, 1975.

[38] E. Murad, "The reactions of Ba^+ ions with O_2 and H_2O," *J. Chem. Phys.*, vol. 77, pp. 2057–2060, 1982.

[39] W. Tsang and R. Hampson, "Chemical kinetic data base for combustion chemistry. Part I. methane and related compounds," *J. Phys. Chem. Ref. Data*, vol. 15, 1986.

[40] K. Schofield, "The bond dissociation energies of group IIA diatomic oxides," *Chem. Rev.*, vol. 67, no. 6, pp. 707–715, 1967.

[41] J. Roquais, F. Poret, R. le Doze, J. Ricaud, A. Monterrin, and A. Steinbrunn, "Barium depletion study on impregnated cathodes and lifetime prediction," *Appl. Surf. Sci.*, vol. 215, pp. 5–17, 2003.

[42] A. Shih, J. Yater, and C. Hor, "Ba and BaO on W and on Sc_2O_3 coated W," *Appl. Surf. Sci.*, vol. 242, pp. 35–54, 2005.

[43] E. Rittner, W. Rutledge, and R. Ahlert, "On the mechanism of operation of the barium aluminate impregnated cathode," *J. Appl. Phys.*, vol. 28, no. 12, pp. 1468–1473, 1957.

[44] R. Forman, "Surface studies of barium and barium oxide on tungsten and its application to understanding the mechanism of operation of an impregnated tungsten cathode," *J. Appl. Phys.*, vol. 47, p. 5272, 1976.

Chapter 4

Surface Kinetics of Monolayer Oxygen Poisoning

4.1 Introduction

The goal of this chapter is to investigate the physical processes responsible for cathode degradation during oxygen poisoning and develop a reaction kinetics model for the emitter surface that can be coupled with the transport model. The experimental results presented in §2.3 show that the cathode temperature increases during oxygen poisoning, indicating a change in the surface state. The cathode exhibits rapid poisoning and recovery for different discharge currents. The cathode response is explained using a time-dependent model of the adsorption/desorption processes of oxygen and barium on the tungsten surface. The background information for the basis of this model is presented in §4.2 and the theoretical framework is discussed in §4.4. Further experimental work was completed at different cathode operating conditions to determine the physics governing oxygen adsorption/desorption and the corresponding rate coefficients and desorption energies. These results are presented in §4.5. Finally, a discussion of how the reaction kinetics model is coupled with the transport model is presented in §4.9.

4.2 Background

A significant amount of data exists in the literature on how the work function of a transition metal varies with coverage of an alkali metal [1]. Various substrate systems have been studied including, but not limited to Ba/W [2–4], Ba/Mo [5], Ba/Ag [6], Cs/Nb [7], and Ba/Nb [7]. The data show that as the transition metal surface is covered with either an alkali metal or an alkaline earth metal, the work function steadily decreases until it reaches a minimum, ϕ_m, at a coverage less than a monolayer. Above this coverage level, the work function will increase and approach a value equal to the work function of the bulk alkali metal [1]. A typical curve showing how the work function varies

with coverage is shown in Fig. 4.2.1 for Ba/W [4].

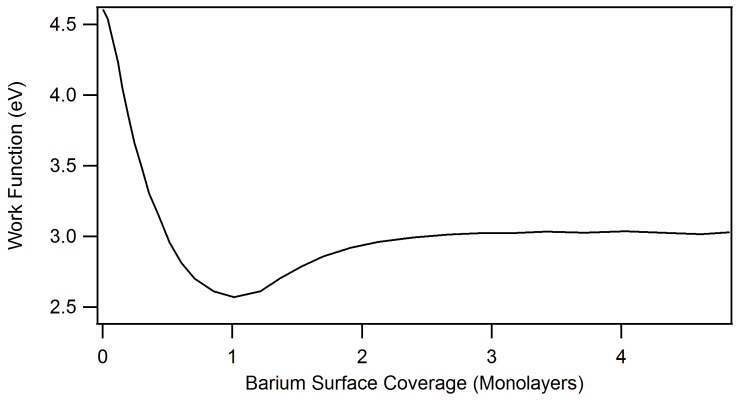

Figure 4.2.1: The variation in the work function with barium coverage for a W(001) surface [4].

Gurney [8] explained this phenomenon by positing that the valence electrons in the electropositive adatoms shift toward the metal substrate, creating a dipole with an axis perpendicular to the surface. The electric field generated by the dipole reduces the potential barrier necessary for electron extraction [1]. At low coverages, the change in the work function is nearly linear and can be modeled by the following equation for non-interacting dipoles [1, 2]

$$\Delta\phi = \pm\mu_D\theta N_0/\epsilon_0, \tag{4.2.1}$$

where μ_D is the magnitude of the dipole perpendicular to the surface, θ is the surface coverage, N_0 is the density of sites available for adsorption, and ϵ_0 is the permittivity of free space. A negative sign is applied to Eq. (4.2.1) for positively outward pointing dipoles. At high coverages, the slope of $\Delta\phi$ versus θ is no longer linear as lateral interactions between the adatoms cause depolarization [1]. A detailed model of the change in work function that accounts for depolarization effects is presented by Gyftopolous and Levine [9].

Several studies have been done to understand how coadsorption of oxygen and electropositive atoms onto a transition metal surface affects the work function and surface structure [2,4,6,7,10–12]. Papageorgopoulos and Chen studied the adsorption of oxygen on a cesium-covered tungsten (100) surface [10]. They observed that oxygen dissociatively adsorbs onto the cesium layer and then migrates under the cesium and bonds directly to the tungsten substrate [10]. This place exchange process likely occurs because of the small size of oxygen relative to cesium and because the Cs/W binding energy is lower than the O/W binding energy, making the latter configuration the most energetically favorable [10].

Lamartine, Czarnecki, and Haas studied the adsorption of oxgen onto a barium-covered polycrystalline tungsten surface [2]. A plot of the variation in work function with oxygen exposure is shown

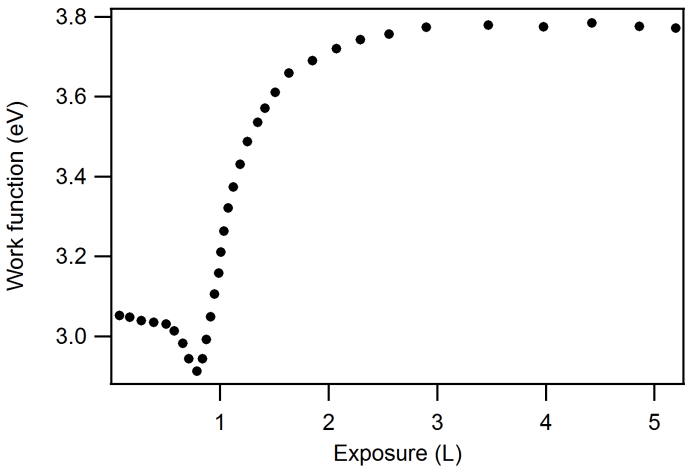

Figure 4.2.2: Variation in the work function with oxygen exposure of a Ba/W surface with $\theta_{Ba} = 1.10$.

in Fig. 4.2.2 for tungsten with a barium coverage of $\theta_{Ba} = 1.10$. The oxygen exposure is expressed in units of Langmuirs, where 1 L = 1×10^{-6} Torr-s. The work function initially decreases to a minimum value then sharply increases before leveling off. The initial lowering of the work function at oxygen exposures less than 1 L is evidence of the place exchange process discussed above in which oxygen penetrates the barium layer and bonds directly to the tungsten. If the oxygen was adsorbed on top of the barium, an increase in the work function would be observed. This is not the case, however.

Lamartine et al. [2] noted that for cesium adsorbed onto various surfaces, the value of the minimum work function decreased as the substrate work function increased. The O/W surface has a higher work function than bare tungsten because the electronegativity of oxygen creates a negatively outward pointing dipole. Lamartine et al. [2] explain that when barium is adsorbed onto the O/W surface, a stronger dipole occurs between the Ba adatoms and the substrate as a result of the increased work function of the substrate, and therefore, the minimum work function is reduced, i.e., ϕ_{min} for Ba/O/W is lower than ϕ_{min} for Ba/W.

Once the oxygen layer under the barium becomes saturated, the place exchange process ceases and the oxygen then adsorbs on top of the barium. This process is observed in Fig. 4.2.2 as a sharp increase in the work function. Behavior similar to that shown in Fig. 4.2.2 has been observed in several other systems including O adsorption on Cs/W surfaces [10], coadsorption of O and Ba on Re(0001) [11], and coadsorption of O and Ba on Ag [6]. Forman [13] also notes that the Ba/O/W multilayer occurs with barium on top of the oxygen regardless of the order of adsorption.

An advantage of the Ba/O/W multilayer system for cathode operation is that the barium atoms are more strongly bound to the oxygen-covered tungsten surface than they are to the bare tungsten

substrate. Forman [13] determined that the desorption energy of barium from the the Ba/O/W surface is 4.8 eV, which is approximately 1 eV higher than the binding energy of barium on tungsten.

4.3 Adsorption/Desorption Kinetics of Barium on the Cathode Emitter Surface

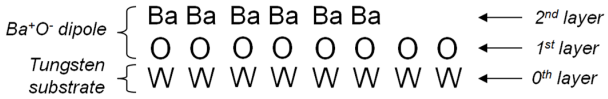

Figure 4.3.1: Cathode emitter surface configuration showing the $Ba^{+}O^{-}$ dipole on top of the tungsten substrate.

A simple conceptual model for the emitter surface consists of three monolayers as shown in Fig. 4.3.1. The tungsten substrate is designated as the zeroth layer, and is assumed to be covered with a complete oxygen monolayer (designated as the first layer). The oxygen atoms that populate this layer reach the surface via adsorption of BaO through the gas phase and BaO diffusion through the pores and along the surface. The BaO molecules that reach the surface form a complete monolayer on top of the tungsten substrate. A BaO monolayer is defined such that barium atoms occupy half of the available sites and the oxygen atoms occupy the other half [14]. Barium oxide begins to dissociate on the surface at temperatures near 1150 K [15]. The free barium produced during this reaction subsequently desorbs, creating an oxygen-rich surface. Barium oxide is replenished to the surface, and the process of bond breaking and barium evaporation continues until a complete oxygen monolayer is formed.

The activation energy required to remove oxygen from the bare tungsten substrate is 6.38 eV [16]. Based on reaction rates published elsewhere [16] for thermal desorption of oxygen from a bare tungsten surface, a timescale of approximately 10^9 s is required to clean the tungsten at typical cathode operating temperatures (∼1400 K). Since the oxygen is tightly bonded to the bare tungsten surface, this model assumes an oxygen surface coverage of unity for the first layer.

The second layer is comprised of barium atoms. Barium supply mechanisms include adsorption of Ba and BaO from the gas and diffusion through the pores from the emitter reservoir. Removal mechanisms may include thermal desorption and xenon ion sputtering. The time rate of change of the surface coverage of atomic barium in the second layer can be written as

$$\frac{d\theta_{Ba}}{dt} = \frac{1}{N_0}\left[\Gamma_{ad,Ba} + \Gamma_{ad,Ba^+} - \Gamma_{d,Ba}\right] \tag{4.3.1}$$

$$= \frac{1}{N_0}\left[s_0\left(1-\theta_{Ba}\right)\left(\Gamma_{Ba} + \Gamma_{Ba^+}\right) - \Gamma_{d,Ba}\right]. \tag{4.3.2}$$

Langmuir adsorption kinetics is assumed such that the sticking coefficient is proportional to the

fraction of open adsorption sites, $s_0\,(1-\theta_{Ba})$, where θ_{Ba} is the barium surface coverage and s_0 is the sticking coefficient at zero coverage and is assumed to be unity.

It is assumed that barium adsorption from the gas phase onto the first oxygen layer replenishes the surface faster than surface diffusion and Knudsen flow through the pores from the barium reservoir. Barium adsorption fluxes were determined from the barium transport model described in §3.5 and are of the order 10^{18} $\mathrm{m^{-2}s^{-1}}$. An upper bound for the diffusion flux to the surface can be obtained by assuming that no barium atoms escape from the pores into the gas phase. The barium diffusion flux is calculated via Eq. (3.5.22) to be a factor of at least 34 times less than the flux of barium to the surface through the gas phase. Therefore, the contribution from diffusion through the tungsten pores is neglected and the surface coverage of barium is maintained via transport through the gas phase. $\Gamma_{Ba} = n_{Ba}\bar{c}_{Ba}/4$ is the flux of neutral barium atoms impinging on the surface at the mean thermal velocity, $\bar{c}_{Ba} = (8kT_p/\pi m_{Ba})^{1/2}$; $\Gamma_{Ba^+} = n_{Ba^+}v_{Bohm,Ba}$ is the flux of barium ions entering the cathode sheath at the Bohm velocity, $v_{Bohm,Ba} = (kT_e/m_{Ba})^{1/2}$; $\Gamma_{d,Ba}$ is the flux of barium desorbing from the surface.

The density of surface sites available for adsorption is represented by N_0. Note that Fig. 4.3.1 is a very simplistic view of the surface as the atomic radii of barium, oxygen, and tungsten are 215, 60, and 135 pm, respectively [17]. Since the atomic radius of Ba is approximately 1.6 times larger than W, the surface density of barium is 40% of the surface density of tungsten. Gyftopoulos [9] reports the surface density of W(110) as 14.1×10^{18} $\mathrm{m^{-2}}$, and therefore, we use the value of 5.6×10^{18} $\mathrm{m^{-2}}$ for the surface density of barium. Note that the barium monolayer density can vary between 4×10^{18} $\mathrm{m^{-2}}$ for a Ba(100) surface and 5.6×10^{18} $\mathrm{m^{-2}}$ for a Ba(110) surface [18].

In vacuum cathodes, the barium desorption process is largely thermal. However, in the presence of a plasma, ion sputtering and electron-stimulated desorption may play a large role. Sputter desorption occurs when an atom is ejected from a surface following bombardment by energetic particles. The amount of energy transferred during such a binary collision is given by

$$E_t = E_i\gamma, \tag{4.3.3}$$

where E_t is the energy transferred during the collision, E_i is the energy of the projectile, and

$$\gamma = \frac{4m_1m_2}{(m_1+m_2)^2}. \tag{4.3.4}$$

The masses of the projectile and target atom are m_1 and m_2, respectively. In order for desorption to occur, the energy transferred to the target atom must exceed the surface binding energy, E_B, and therefore,

$$E_i > \frac{E_B}{\gamma}. \tag{4.3.5}$$

Equation (4.3.5) does not take into account the energy loss due to other collisions these species may suffer, and therefore, E_B/γ can only be considered as the absolute lower bound for sputtering [19]. Eckstein [19] notes that for large values of m_2/m_1, the sputtering threshold energy, E_{th}, approaches E_B/γ. For $m_2/m_1 \leq 1$, several collisions are required for the momentum reversal of the incident ion, which causes E_{th} to increase beyond E_B/γ [19]. Since the mass ratio of barium and xenon is near unity, we can expect the threshold energy to be larger than that predicted by Eq. (4.3.5).

Bohdansky et al. [20] propose that the threshold energy for sputtering can be determined by

$$E_{th} = 8E_B \left(\frac{m_1}{m_2}\right)^{5/2} \tag{4.3.6}$$

for $m_1/m_2 > 0.3$. The sputtering threshold energy for xenon ion bombardment of barium atoms with a desorption energy of 4.8 eV is calculated from Eq. (4.3.6) to be 34.3 eV. This value is more than two times larger than the sheath potentials in the cathode, which may be as high as 15 V, and therefore, xenon ion sputtering of barium will be neglected.

Doerner et al. [21] studied barium removal from an impregnated tungsten cathode in the presence of xenon ions. The authors propose that energetic ions may liberate barium atoms from the lattice structure so that they are bound to the surface at a lower binding energy, allowing them to desorb at a higher rate. The results show that the plasma-enhanced desorption process occurs for ion energies greater than 15 eV, and therefore, this process will not be included here.

Ageev et al. [22] studied electron-stimulated desorption of barium from a tungsten surface covered with a monolayer of oxygen and determined that a threshold energy of 25 eV is required for electrons to remove barium. Typical electron temperatures in the cathode discharge plasma are around 2 eV and the sheath potential can be as high as 15 V. At such low temperatures, Maxwell-Boltzmann statistics predicts a vanishingly small number of electrons that possess energies capable of overcoming the sheath potential and desorbing barium atoms. The process of electron-stimulated desorption is therefore neglected.

According to work completed by Forman [23], thermal desorption of barium is described by the following equation:

$$\Gamma_{d,Ba} = N_0 A_{Ba} \theta_{Ba}^5 e^{-E_{Ba}e/kT}. \tag{4.3.7}$$

The values of the pre-exponential factor and desorption energy were determined to be $A_{Ba} = 2.12 \times 10^6$ s^{-1} and $E_{Ba} = 2.06$ eV, respectively, based on experiments at 1000 and 1100 K [23]. The barium adatoms strongly interact with each other, causing an apparent reduction in the surface binding energy that is linear with θ. In Forman's relation given above, the θ^5 dependence accounts for the effect of these adatom interactions, while keeping the value of E_{Ba} constant. Therefore, it is important to note that the value, $E_{Ba} = 2.06$ eV, is not the actual value of the surface binding energy of Ba on O and can be better thought of as a fitting parameter to Eq. (4.3.7). Forman

determined the value of the surface binding energy in a separate work as 4.8 eV [13]. Data at typical cathode operating temperatures near 1400 K could not be obtained in Forman's desorption experiments as the initial desorption rates were too rapid [23]. The barium desorption model given in Eq.(4.3.7) was extrapolated out to higher temperatures and has been verified by Forman at 1373 K to within an order of magnitude [23].

Equation (4.3.2) can now be written as

$$\frac{d\theta_{Ba}}{dt} = \frac{1}{N_0}\left[s_0\left(1-\theta_{Ba}\right)\left(\frac{n_{Ba}}{4}\sqrt{\frac{8kT_p}{\pi m_{Ba}}} + n_{Ba^+}\sqrt{\frac{kT_e}{m_{Ba}}}\right)\right] - A_{Ba}\theta_{Ba}^5 e^{-E_{Ba}e/kT}. \tag{4.3.8}$$

A plot of the equilibrium barium coverage on the emitter surface is shown in Fig. 4.3.2 as a function of axial distance along the cathode. These values were calculated by setting Eq. (4.3.8) to zero and solving for the coverage. The densities and temperatures along the emitter surface were taken from the results of the transport model presented in §3.5. The barium coverage is approximately $\theta_{Ba} = 0.9$, which coincides with the minimum in the work function curve shown previously in Fig. 4.2.1. The maximum in the coverage occurs where the barium ions are being redeposited on the surface. The minimum at $z = 2$ cm coincides with the emission zone where barium evaporation rates are higher as a result of higher surface temperatures.

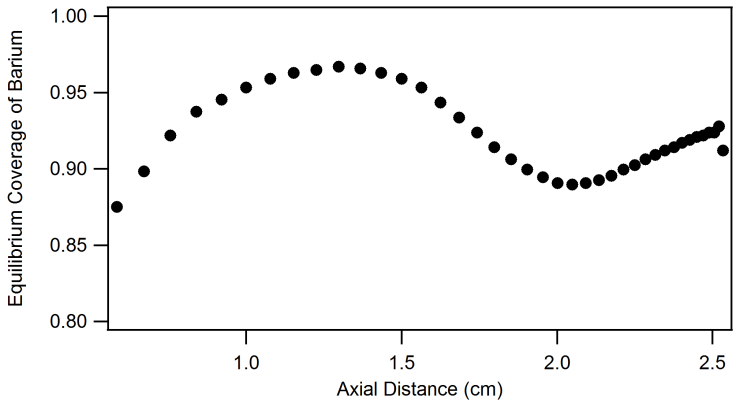

Figure 4.3.2: Variation in barium coverage over the length of the emitter surface.

4.4 Theoretical Framework of an Adsorption/Desorption Kinetics Model for Oxygen Poisoning

If oxygen is present in the discharge, it can compete with barium for adsorption onto sites in the second layer and can also adsorb on top of the barium creating a third layer, which we refer to as the poisoning layer. A schematic diagram of this surface configuration is shown in Fig. 4.4.1. Since the

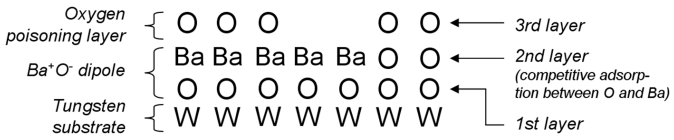

Figure 4.4.1: Cathode emitter surface configuration with excess oxygen. Oxygen on top of the barium layer will modify the electron emission properties.

barium and oxygen compete for sites in the second layer, the fraction of available sites for barium adsorption is now also a function of oxygen coverage. A modification to the sticking factor in Eq. (4.3.8) for the time rate of change of barium coverage must be made and can be written as

$$s = s_0 \left(1 - \theta_{Ba} - \theta_O\right), \tag{4.4.1}$$

where θ_O is the oxygen coverage in the second layer. The full equation for barium kinetics, accounting for competitive adsorption with oxygen is

$$\frac{d\theta_{Ba}}{dt} = \frac{1}{N_0}\left[s_0\left(1 - \theta_{Ba} - \theta_O\right)\left(\frac{n_{Ba}}{4}\sqrt{\frac{8kT_p}{\pi m_{Ba}}} + n_{Ba^+}\sqrt{\frac{kT_e}{m_{Ba}}}\right)\right] - A_{Ba}\theta_{Ba}^5 e^{-E_{Ba}e/kT}. \tag{4.4.2}$$

A relation similar to Eq.(4.3.8) can be written for the oxygen surface coverage in the second layer:

$$\frac{d\theta_O}{dt} = \frac{1}{N_0}\left[\Gamma_{ad,O_2} - \Gamma_{d,O_2} - \Gamma_{d,O}\right] \tag{4.4.3}$$

$$= \frac{1}{N_0}\left[s_0\left(1 - \theta_{Ba} - \theta_O\right)^2 \Gamma_{O_2} - \Gamma_{d,O_2} - \Gamma_{d,O}\right]. \tag{4.4.4}$$

The flux of O, O^+, and O_2^+ may be neglected as the number densities of these species are several orders of magnitude lower than neutal O_2. Molecular oxygen in the gas phase is assumed to dissociatively adsorb onto two surface sites, and the sticking factor is written as [16]

$$s = s_0(1 - \theta_{Ba} - \theta_O)^2. \tag{4.4.5}$$

Experimental data support a high sticking coefficient [16], and therefore, this model assumes $s_0 = 1$. The oxygen flux to the surface can be expressed as $\Gamma_O = \nu P_{O_2}$, where $\nu = (2\pi m_{O_2} kT_p)^{-1/2}$ is the Hertz-Knudsen rate per unit pressure at which molecular oxygen strikes the surface, and P_{O_2} is the partial pressure of oxygen present in the gas flow [16].

The oxygen atoms on the surface can evaporate as atomic oxygen, recombine and evaporate as molecular oxygen, or form tungsten oxides [16]. Only thermal desorption of atomic and molecular oxygen are considered here. The two main oxygen desorption processes are described in the equations

given below:

$$2O^* \rightarrow 2S^* + O_2(g), \tag{4.4.6}$$

$$O^* \rightarrow S^* + O(g), \tag{4.4.7}$$

where O^* indicates an oxygen adatom and S^* indicates an open surface site [16]. The total oxygen desorption flux can be expressed by the following relation:

$$\Gamma_d = \theta_O^2 A_{O_2} e^{-E_{O_2} e/kT} + \theta_O A_O e^{-E_O e/kT}, \tag{4.4.8}$$

where the first and second terms in Eq. (4.4.8) correspond to the reactions given in Eqs. (4.4.6) and (4.4.7), respectively. The exponent in the first term accounts for associative desorption of O_2 from two surface sites. The second term is the contribution to the flux of the desorption of atomic oxygen. Based on experiments conducted over temperatures ranging from 1400 to 3150 K, Schissel and Trulson have determined the pre-exponential factors and desorption energies to be: $A_{O_2} = 5 \times 10^{32}$ m^{-2}·s^{-1}, $A_O = 1.2 \times 10^{33}$ m^{-2}·s^{-1}, $E_{O_2} = 3.86$ eV, and $E_O = 4.94$ eV [16].

For collisions between Xe^+ and O, only 38.7% of the energy is transferred as calculated from Eq. (4.3.3), and therefore, ion energies of at least 12.8 eV are required for desorption of O. The actual threshold energy is likely much higher because of the energy losses these species incur during other collisions [19]. Equation (4.3.6) predicts a threshold energy of over 1 keV for Xe^+ sputtering of O. Although this is probably a gross overestimation, it does indicate that Xe^+ sputtering is improbable. With maximum sheath potentials of ∼15 eV in the cathode discharge plasma, we conclude that sputtering of oxygen from the second layer will be insignificant. Equation (4.4.4) can be expressed as

$$\frac{d\theta_O}{dt} = \frac{1}{N_0}\left[s_0 \left(1 - \theta_{Ba} - \theta_O\right)^2 \frac{P_{O_2}}{\sqrt{2\pi m_{O_2} k T_p}} - \theta_O^2 A_{O_2} e^{-E_{O_2} e/kT} - \theta_O A_O e^{-E_O e/kT}\right]. \tag{4.4.9}$$

The third layer described by the model consists of oxygen atoms that adsorb on top of the barium layer, altering the barium oxide dipole and effectively poisoning the cathode [15]. The build-up of multiple barium layers is not considered here as this configuration has been shown to be unstable at normal cathode operating temperatures [23]. Barium layers on top of the first are weakly bound and rapidly desorb.

Molecular oxygen strikes the barium surface and is initially physisorbed in a weakly-bound state called a precursor. Once the O_2 molecule is on the surface, it can desorb, migrate over the surface, or dissociate and chemisorb onto the surface as atomic oxygen [24]. The time rate of change of the

coverage of this O_2 precursor state is given by [25]

$$\frac{d\theta^*}{dt} = s_0 \frac{\Gamma_{O_2}}{N_0/2} - \theta^* k_{d^*} - k_a \theta^* (1-\theta_p)^2, \tag{4.4.10}$$

where θ^* is the coverage of the O_2 precursor, s_0 is the sticking coefficient at $\theta^* = 0$, k_{d^*} is the desorption rate of the physisorbed O_2, θ_p is the coverage of chemisorbed atomic oxygen, and k_a is the rate of chemisorption. There is an activation energy for the chemisorption process, and the rate is given by

$$k_a = Ae^{eE_a/kT}, \tag{4.4.11}$$

where E_a is the activation energy. German and Efremenko [26] determined the activation energies of dissociative oxygen adsorption onto Rh (111), Ag (111), Ag (110), and Au (111) to be 0.035, 0.551, 0.781, and 1.85 eV, respectively. The value of the activation energy for dissociative oxygen adsorption onto a Ba/O/W surface is unknown, but a range of values similar to those given above for other metals may be used for this system. Note that it is the chemisorbed O that disturbs the Ba^+O^- dipole and is responsible for poisoning. The time rate of change of the coverage of chemisorbed atomic oxygen is given by [25]

$$\frac{d\theta_p}{dt} = k_a \theta^* (1-\theta_p)^2 - \theta_p^2 k_d. \tag{4.4.12}$$

The O_2 precursor and the chemisorbed O may desorb thermally and via xenon ion sputtering. The low bond energy of the precursor state makes it more susceptible to sputter desorption than the more strongly bound chemisorbed state. Thermal desorption is an activated process and the rate constant is of the form given in Eq. (4.4.11). The rate constant for sputter desorption is proportional to the xenon ion flux and the cross section for xenon sputtering of oxygen. A discussion of some experiments performed with this cathode to understand the reaction kinetics of oxygen poisoning will be presented in the following section.

4.5 Experimental Characterization of the Rate Processes during Poisoning and Recovery

Since direct measurements of the oxygen coverage cannot be made of the emitter surface during cathode operation, we use surface temperature measurements to infer the surface state, as will be discussed in §4.6. A series of experiments were performed at a discharge current of 10 A and a xenon flow rate of 2.5 sccm using the same experimental set up as that described in Chapter 2. Oxygen was introduced at a concentration of 100 ppm for a specified amount of time during which the temperature was monitored. Following the exposure, the cathode was allowed to recover to

its initial unpoisoned temperature. This experiment was repeated three times at increasing oxygen exposures as shown in Fig. 4.5.1. A summary of the experimental conditions is presented in Table 4.1.

Table 4.1: Experimental Conditions

Case No.	Exposure (min)	OP $T_{\max}$ (K)	Emitter $T_{\max}$ (K)
1	15	1101	1348
2	30	1107	1354
3	60	1114	1364

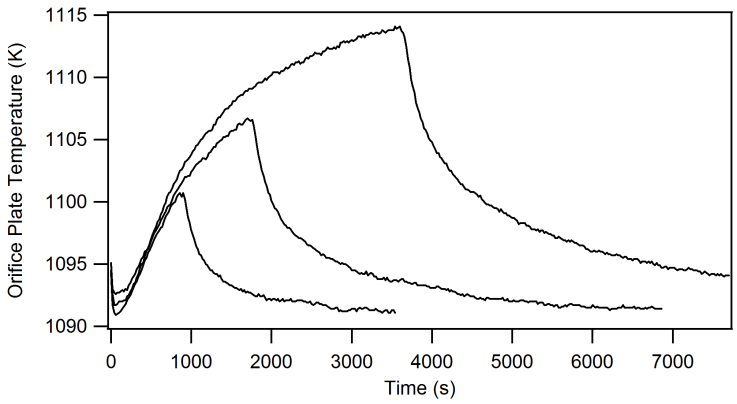

Figure 4.5.1: Orifice plate temperature measurements for the 10 A, 2.5 sccm case at 100 ppm of oxygen poisoning.

Note that Fig. 4.5.1 shows a plot of the orifice plate temperature, which was measured by the thermocouples and recorded once per second. The temperatures increase during oxygen exposure and then decay once the oxygen flow is turned off. Figure 4.5.2 shows the temperature profiles taken before and during poisoning. Note that the shape of the curve is relatively unchanged during poisoning, and the profile is offset by an amount, ΔT, from the unpoisoned profile.

Figure 4.5.3 shows a plot of the emitter temperature at $z = 2.37$ cm (measured by the fiber optic probe) versus the orifice plate temperature (measured by the thermocouples) during this poisoning experiment. The two temperatures vary linearly with each other and the slope is near unity. Using the curve fit given in Fig. 4.5.3, the emitter temperature can be plotted with time as shown in Fig. 4.5.4.

When oxygen is introduced into the discharge plasma, it adsorbs on top of the barium surface and reduces the electron emission. Since the cathode is operated in current-controlled mode, the controller responds to the drop in emission current by increasing the discharge potential. The change in discharge potential during poisoning for these experiments is shown in Fig. 4.5.5.

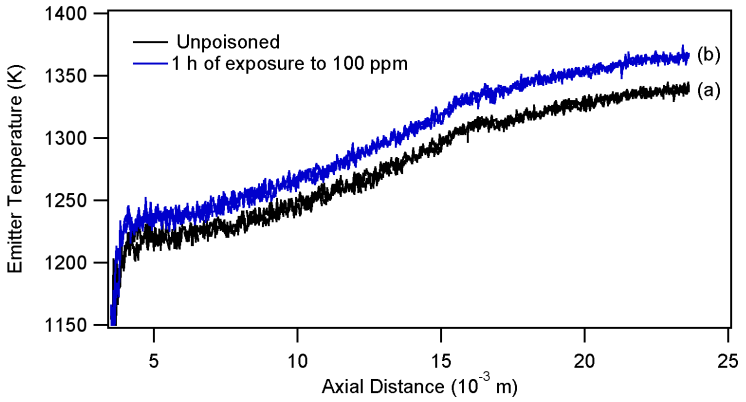

Figure 4.5.2: Temperature profiles of the emitter surface at 10 A, 2.5 sccm. Curve (a) is a plot of the emitter temperature prior to poisoning. Curve (b) is a plot of the emitter temperature following 100 ppm of oxygen exposure for 1 hour.

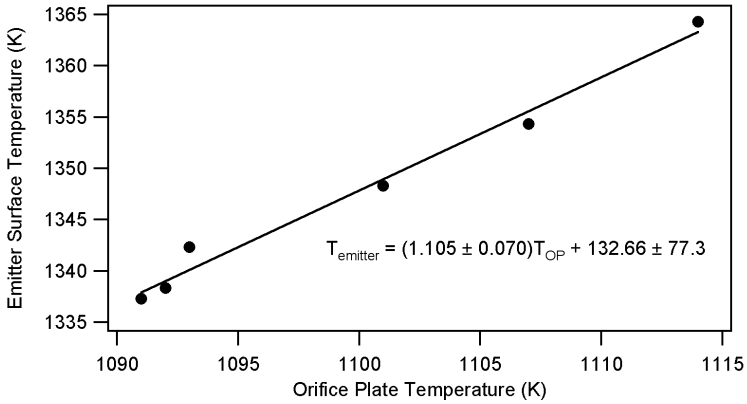

Figure 4.5.3: The emitter temperature at $z = 2.37$ cm is linearly correlated with the orifice plate temperature.

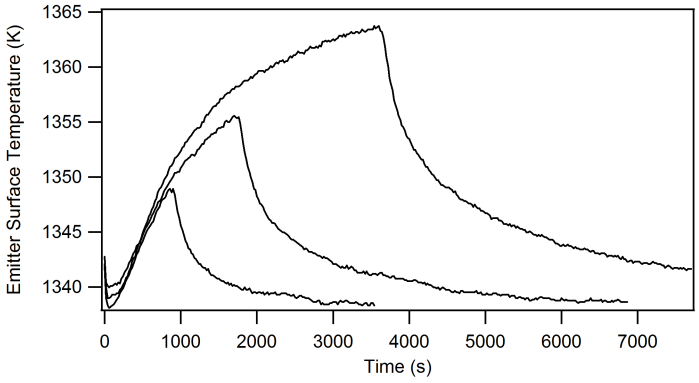

Figure 4.5.4: Emitter temperature measurements for the 10 A, 2.5 sccm using the orifice plate data and the curve fit in Fig. 4.5.3

Knowing that the total current must remain constant, we can use the measurements of the emitter temperature and discharge potential to determine how the emission current density changes during poisoning. We can then relate the change in emission current density to a change in the surface work function and from there, determine oxygen surface coverage. These calculations will be presented in the next section.

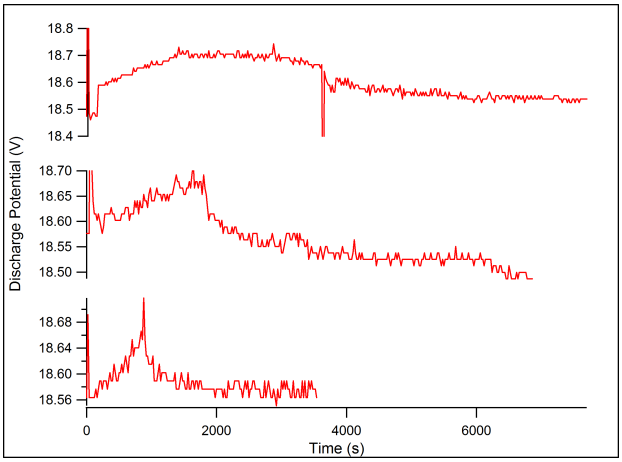

Figure 4.5.5: Variation in discharge potential during oxygen poisoning.

4.6 Understanding the Surface State from Emitter Temperature Measurements

The fundamental quantity of interest in poisoning is the oxygen surface coverage. Therefore, the goal of the calculation in this section is to infer the surface coverage using indirect measurements. An increase in the oxygen surface coverage will increase the surface work function, which results in either a change in the surface temperature (when current density is held constant) or a change in the emission current density (when temperature is held constant). Neither parameter is held fixed in this cathode, however, as it is the total current that is controlled. A discussion of the total current will be presented first, followed by a discussion of cathode heating to help illuminate why an increase in temperature is observed during poisoning. Once we understand how the emission current density changes during oxygen exposure, we can use this parameter along with the temperature measurements to extract the oxygen surface coverage.

4.6.1 Contributions to the Total Current in Hollow Cathodes

The total current, J, produced by the emitter is defined as

$$J = \int_S \mathbf{j} \cdot \mathrm{d}\mathbf{A} = 2\pi r \int_0^L \mathbf{j}(z) \cdot \mathrm{d}z \, \hat{\mathbf{r}}, \tag{4.6.1}$$

where r is the inner radius of the insert and L is the length of the emitter. The net current density, $\mathbf{j}$, is the sum of the ion current density, j_i, reverse electron current density, j_{rev}, and emitted electron current density, j_e.

$$\begin{aligned} \mathbf{j} = \mathbf{j}_{\mathrm{net}} = & \quad \mathbf{j}_i + \mathbf{j}_{\mathrm{rev}} + \mathbf{j}_e \\ = & \quad (j_i - j_{\mathrm{rev}} + j_e)\, \hat{\mathbf{r}} \end{aligned} \tag{4.6.2}$$

The ion current density is given by $j_i = n_i q v_i$, where n_i is the ion density at the sheath edge. Ions are accelerated toward the emitter walls at the Bohm velocity, given by $v_B = (kT_e/m_i)^{1/2}$, as a result of potential gradients that develop near the surface in order to equalize the rate at which electrons and ions strike the surface [27]. These regions of potential gradients are called sheaths, and they are typically a few Debye lengths in thickness [27]. The Debye length, which is given by $\lambda_D = \left(\epsilon_0 kT_e/n_e q^2\right)^{1/2}$, is the length over which charges are shielded [27]. The electron density near the sheath edge is $n_e e^{-1/2}$, where n_e is the plasma density in the bulk plasma [28]. The ion current density can therefore be written as

$$j_i = 0.606\, n_e q \left(\frac{kT_e}{m_i}\right)^{1/2}. \tag{4.6.3}$$

The reverse electron current is comprised of electrons with sufficient energy to overcome the sheath potential barrier at the wall and is given by the following relation:

$$j_{\mathrm{rev}} = \frac{1}{4} n_e q \left(\frac{8eT_e}{\pi m_e}\right)^{1/2} e^{-\phi_{\mathrm{sheath}}/T_e}. \tag{4.6.4}$$

The electron current density, j_e, produced during cathode operation is a function of the emitter surface temperature, T, and the work function, ϕ, as described by the Richardson-Dushman equation:

$$j_e = \beta T^2 e^{-e\phi/kT}, \tag{4.6.5}$$

where β is a theoretical constant defined as $\beta \equiv \dfrac{4\pi m_e q k^2}{h^3}$ [29]. The emission current density is calculated in the xenon plasma model using Eq. (4.6.5). The work function, ϕ, for a 4:1:1 tungsten

cathode is calculated as a function of temperature using

$$\phi = 1.41 + 5.0 \times 10^{-4} T, \tag{4.6.6}$$

where ϕ is in electron-volts and T is in Kelvin [30, 31]. In the presence of an electric field, the effective work function of the surface is reduced due to the Schottky effect, in which the applied field reduces the potential barrier that the electrons must overcome during emission [32]. The effective work function of the surface is then given as $\phi_{\text{eff}} = \phi_0 - \phi_s$, where the Schottky potential is

$$\phi_s = \left(\frac{e\varepsilon}{4\pi\epsilon_0} \right)^{1/2}, \tag{4.6.7}$$

and ε is the electric field [32]. The current density for a given surface accounting for the Schottky effect can now be expressed as

$$j_e = \beta T^2 e^{-e(\phi_0 - \phi_s)/kT}, \tag{4.6.8}$$

where ϕ_0 is given by Eq. (4.6.6).

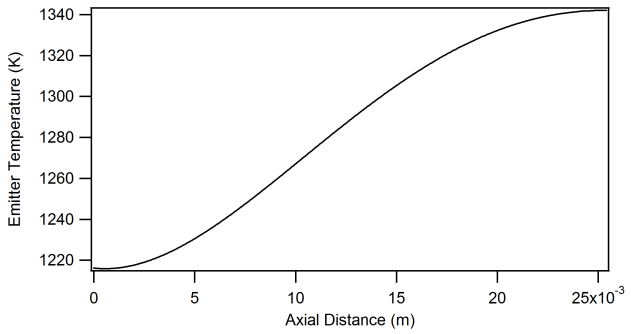

(a) Temperature profile during normal operation at 10 A.

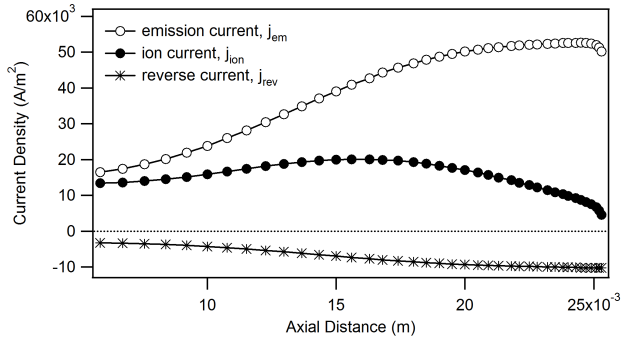

(b) Current density profiles during normal operation at 10 A.

Figure 4.6.1: Temperature and current density profiles for a discharge current of 10 A and a xenon flow rate of 2.5 sccm [33].

The ion and reverse electron current densities depend on the plasma density, electron temperature, and sheath potential along the wall. These parameters were calculated from the xenon plasma

modeled developed by Mikellides et al. [33]. The emission current density was calculated via Eq. (4.6.8) given a temperature profile obtained experimentally at the operating condition of interest. Plots of the temperature profile and current densities during normal cathode operation at 10 A of discharge current and a xenon flow rate of 2.5 sccm are shown in Fig. 4.6.1.

In the experimental results presented in the previous section, the discharge potential increases by up to 0.2 V during the oxygen exposure. Assuming that changes in the discharge potential are solely due to changes in the sheath potential and that T_e and n_e remain constant, this increase in discharge potential causes a maximum reduction in the reverse electron current density of approximately 8%. If we continue the assumption that T_e and n_e are constant, then the ion current density, which is small compared with the other terms in Eq. (4.6.2), is also constant. Therefore, the emission current density must decrease by the same amount as the reverse electron current density in order to satisfy the constant-current constraint.

4.6.2 Hollow Cathode Heating

The goal of this section is to provide insight on the mechanisms that cause the increase in the observed temperature during oxygen poisoning. The heating and cooling of the emitter surface occur via particle bombardment and electron emission, respectively. Katz et al. [34] developed a thermal model for the hollow cathode, which is summarized here. Katz et al. [34] assume that the heat flux to the emitter is

$$\dot{q} = -j_e\phi_{\text{wf}} + j_{\text{rev}}(2T_e + \phi_{\text{wf}}) + j_i\left(\phi_{\text{sheath}} + 0.5T_e + \Phi - \phi_{\text{wf}}\right). \tag{4.6.9}$$

The rate at which emitted electrons cool the surface is proportional to the work function, whereas the reverse electrons heat the surface at a rate proportional to the sum of the work function and the average electron kinetic energy, $2T_e$ [34]. Ions impinging on the surface heat the emitter by the sum of their kinetic energy and ionization potential, and they cool the emitter by the work function as they remove electrons from the surface during recombination [34]. By estimating the changes to each of the three terms in Eq. (4.6.9) during poisoning, we can determine the dominant mechanism(s) for the temperature increase.

Table 4.2 lists the plasma parameters pre- and post-poisoning at $z = 2.37$ cm for case 3 (see Table 4.1 and Fig. 4.5.1). The values of the parameters listed for the unpoisoned case were calculated using the xenon plasma model developed by Mikellides et al. [33]. The plasma density and electron temperature were assumed to be constant during oxygen exposure, and thus, the ion current was also constant. It was assumed the change in sheath potential after 1 h of oxygen exposure was equivalent to the change in discharge potential. The reverse current after 1 h of oxygen exposure was calculated from Eq. (4.6.4), and the emission current was calculated from Eq. (4.6.2). Finally,

the work function was calculated using the calculated emission current density and the emitter temperature.

Table 4.2: Plasma Parameters for Case 3

	n_e (m^{-3})	T_e (eV)	ϕ_s (eV)	ϕ_{wf} (eV)	j_e (A/m^2)	j_{rev} (A/m^2)	j_i (A/m^2)
Unpoisoned	8.07×10^{19}	2.39	13.9	2.0257	52600	10100	10400
Poisoned[a]	8.07×10^{19}	2.39	14.1	2.0642	52250	9289	10400

[a]Values of n_e, T_e and j_i are assumed to be constant during poisoning.

From these results it is clear that after oxygen exposure for 1 h, the emission current drops slightly from its unpoisoned value while the work function increases. The resulting effect is that the cooling provided by the emitted electrons, given by term 1 in Eq. (4.6.9), increases by approximately 1.2%. As the sheath voltage increases, the reverse electron current density decreases and the cathode experiences less electron heating. Therefore, the heat flux from electron bombardment, given by term 2 in Eq. (4.6.9), drops by approximately 7.5% due the increase in sheath potential.

This simple analysis shows that the first two terms in Eq. (4.6.9) will contribute to a drop in emitter temperature during poisoning. The third term will increase slightly as a result of the increase in sheath potential; however, it is not enough to account for the reduction in heat flux of the first two terms. This result is clearly incorrect as a marked temperature increase is observed each time the cathode is exposed to oxygen. In order for the cathode to even maintain a constant heat flux to the emitter, the ion current must increase by approximately 1.8% of its initial unpoisoned value. It is clear, therefore, that the ion current must increase during poisoning in order to produce the observed temperature rises. This conclusion makes physical sense because increases in the sheath potential should accelerate ions toward the wall, thereby increasing the ion current. We could better determine the effects of oxygen poisoning on the plasma parameters if the transport model could be incorporated with the plasma model so the two are solved self-consistently. Although the merger of these two models is outside the scope of this work, it may be something to consider for the future.

4.6.3 Oxygen Surface Coverage Calculations

The offset in emission current density during poisoning is calculated from Eqs. (4.6.1) and (4.6.2) for a total discharge current of 10 A using measurements of the discharge potential and the emitter temperature. An effective work function is then calculated from the emission current density (assuming the Schottky potential remains constant) and is compared with the work function of the pre-poisoned surface. A plot of the change in work function is shown in Fig. 4.6.2 at $z = 2.37$ cm. Note that small increases in the work function on the order of 10^{-2} eV are calculated for these

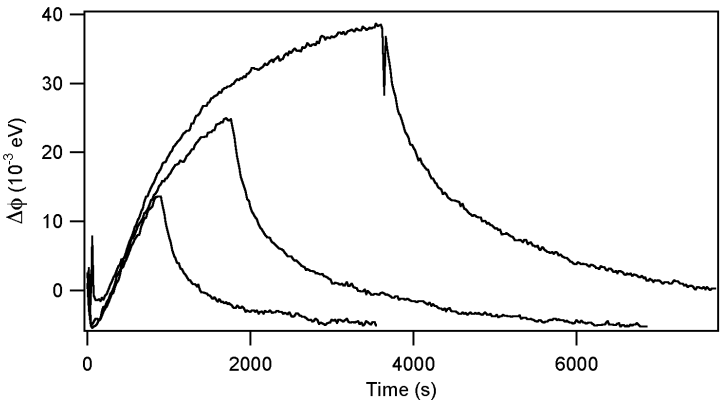

Figure 4.6.2: Change in the work function of the emitter surface during poisoning.

experiments.

We can relate the increase in work function to the oxygen coverage on top of the barium layer using the data from Lamartine et al. [2] in Fig. 4.2.2. Although the data presented in Fig. 4.2.2 is for $\theta_{Ba} = 1.10$, Lamartine et al. observe the same trends for coverages near to or greater than a monolayer, whereas oxygen adsorption onto a tungsten surface with $\theta_{Ba} = 0.48$ did not produce a decrease in the work function [2]. The barium coverage calculated in §4.3 varies from 0.85 to 0.96. Additionally, Haas et al. report that for a vacuum cathode operating at a surface temperature of 1350 K, the barium surface coverage on top of the oxygen monolayer is approximately $\theta_{Ba} = 0.9$ [35].

Before we can apply Lamartine's data to our problem, we must convert the data in Fig. 4.2.2 from units of oxygen exposure to surface coverage. The time rate of change of oxygen coverage for their experiment can be described as follows, assuming Langmuir adsorption kinetics onto two sites:

$$\frac{d\theta}{dt} = s_0(1-\theta)^2 \frac{1}{N_0} \frac{P_{O_2}}{(2\pi mkT)^{1/2}}. \tag{4.6.10}$$

Note that their experiment takes place at low temperatures where desorption is negligible. The solution to Eq. (4.6.10) is

$$\theta(t) = \frac{s_0 P_{O_2} t}{s_0 P_{O_2} t + N_0 (2\pi mkT)^{1/2}}, \tag{4.6.11}$$

where $T = 300$ K, $N_0 = 5.6 \times 10^{18}$ m^{-2}, and s_0 is assumed to be unity. The exposure is equal to $P_{O_2}t$, and therefore, we can use Eq. (4.6.11) and the data in Fig. 4.2.2 to relate the change in work function to the oxygen coverage. We assume that prior to cathode poisoning we are already operating at the minimum of the curve presented in Fig. 4.2.2, where the barium is on top of a complete oxygen monolayer. Therefore, we set theta to zero at this location and reference the change in the work function to the value at the minimum. A plot of the change in work function with oxygen coverage is presented in Fig. 4.6.3.

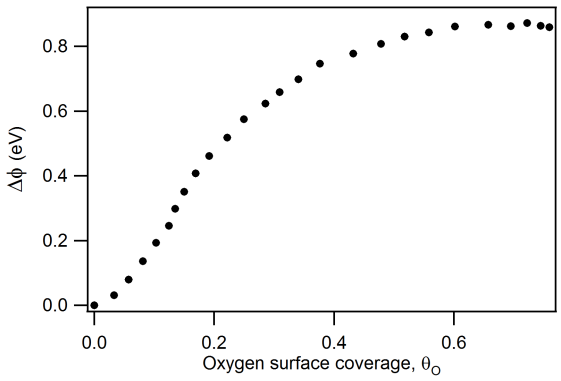

Figure 4.6.3: Change in the work function with oxygen coverage on top of the barium layer [2].

Using Fig. 4.6.3, we can convert the data shown in Fig. 4.6.2 from $\Delta\phi$ versus time to θ_p versus time. Plots of the oxygen surface coverage for each of the three cases at 10 A are shown in Fig. 4.6.4. The coverages in this experiment are very small and are on the order of $\theta = 10^{-2}$. Additionally, the transients for both the uptake and decay portions of the curves shown in Fig. 4.6.4 are very long. For oxygen concentrations of 100 ppm, thermal velocities on the order of 10^3 m/s, a sticking coefficient near unity, and a surface density of 5.6×10^{18} sites/m^2, the surface should fill up with oxygen on the order of 1 s. However, the curves show it takes thousands of seconds for the surface to reach a coverage of only 3%. The transport model presented in Chapter 3 does not reveal any process that would limit the oxygen flux to the surface. If the long delay in poisoning is caused by a fast desorption process, the coverage would approach equilibrium quickly and we would observe a sharp drop in the oxygen coverage once the oxygen flow valve is closed. The uptake and decay are prolonged, however. These results indicate that some mechanism is limiting adsorption of atomic oxygen onto the surface in the poisoning state. The following sections are devoted to understanding the observed phenomena.

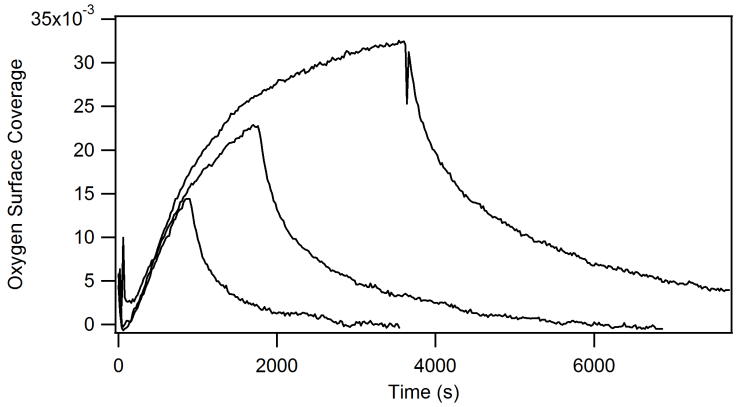

Figure 4.6.4: Plot of oxygen surface coverage on the emitter surface.

4.7 Empirical Analysis of Reaction Rates during Oxygen Poisoning and Recovery

4.7.1 Adsorption Kinetics

Figure 4.7.1 shows the oxygen uptake curve for case 3. The data can be fit to a single exponential with a time constant of $\tau = 1079.5 \pm 13.1$ s over the entire range of θ plotted. The long time constant indicates the existence of some mechanism limiting the adsorption of oxygen onto the surface. This phenomenon is not observed in vacuum cathodes as they poison quickly when exposed to oxygen. The hypothesis presented here is that xenon ions sputter the O_2 precursor at a faster rate than dissociative chemisorption. The precursor state will then reach a low O_2 equilibrium coverage quickly (on the order of 1 s). Recall from Eq. (4.4.12) that the adsorption rate of atomic oxygen is $k_a\theta^*(1-\theta_p)^2$. Therefore, it is evident that small values of θ^* reduce the rate of adsorption of atomic oxygen in the poisoning state and slow down the poisoning process.

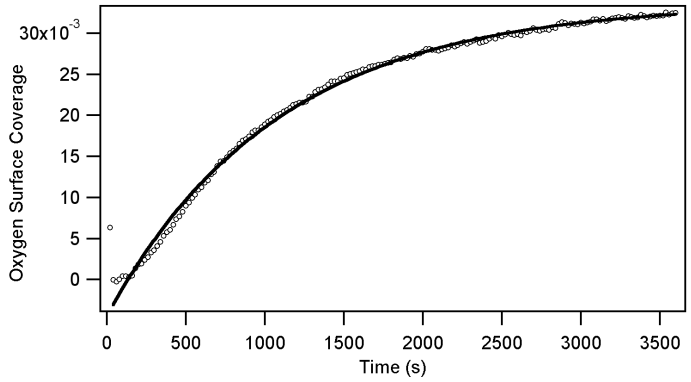

Figure 4.7.1: Single exponential fit to the oxygen coverage data during poisoning.

Equations (4.4.10) and (4.4.12) were solved simultaneously and the resulting values of θ_p are plotted and compared with the data as shown in Fig. 4.7.2. The form of the sputter desorption rate is

$$k_{d^*} = \frac{Y\Gamma_{Xe^+}}{(N_0/2)}, \tag{4.7.1}$$

where Y is the sputter yield and represents the number of particles ejected from the surface per ion. This value is unknown for O_2 sputtering from a Ba/O/W surface, but was taken to be 0.1. The rate constants for dissociative adsorption of oxygen on the Ba/O/W surface are unknown, but an activation energy of 1.36 eV was used here, which is within the range presented by German and Efremenko [26]. The rate constants for desorption of atomic O from the Ba/O/W surface are also unknown, but a rate equal to 10^{-2} s^{-1} fits the data. The desorption process will be explored further in the following section.

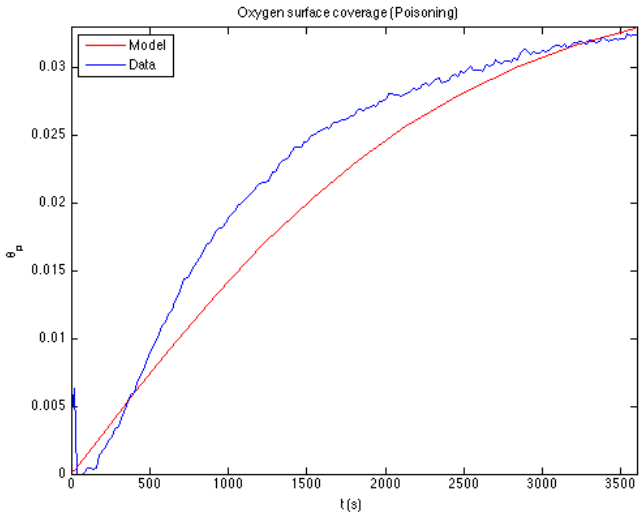

Figure 4.7.2: Results of the kinetics model compared with the experimental data.

This model appears to explain the long transients and low equilibrium coverage of oxygen in the poisoning layer. However, fundamental atomic data on the major processes is needed to validate this hypothesis. The dominant processes include dissociative adsorption of oxygen, sputtering of the O_2 precursor, and desorption of atomic oxygen.

An alternate explanation for the long transients and low coverages observed is that the oxygen number density in the xenon plasma is low because of oxygen gettering upstream of the cathode. If significant oxygen gettering occurs, the time constant for filling the plasma control volume will be prolonged and the oxygen number density will increase as

$$n = n_0 \left(1 - e^{-t/\tau}\right). \tag{4.7.2}$$

We may assume simple adsorption/desorption kinetics since the oxygen surface coverage is much less than unity:

$$\frac{d\theta}{dt} = \frac{1}{N_0}\left(\Gamma_a - \theta\Gamma_d\right). \tag{4.7.3}$$

Substituting $\Gamma_a = n\bar{c}/4 = n_0\left(1 - e^{-t/\tau}\right)\bar{c}/4$ into Eq. (4.7.3) and solving for $\theta(t)$ gives

$$\theta(t) = \frac{n_0\bar{c}}{4\Gamma_d(\Gamma_d\tau - N_0)}\left(N_0 e^{-\Gamma_d t/N_0} + \Gamma_d\tau\left(1 - e^{-t/\tau}\right) - N_0\right). \tag{4.7.4}$$

This equation is fit to the data given in Fig. 4.7.1 and yields $\Gamma_d = 6.042\times10^{15} \pm 1.05\times10^{14}$ m$^{-2}\cdot$s^{-1}, $n_0\bar{c}/4 = 1.982\times10^{14} \pm 2.89\times10^{12}$ m$^{-2}\cdot$s^{-1}, and $\tau = 206 \pm 8.17$ s. The results show that the oxygen number density saturates at approximately 6×10^{11} m^{-3}. This phenomenon will be addressed in the following section.

4.7.2 Thermal Desorption

The decay portions of the coverage versus time curves shown in Fig. 4.6.4 are best fit to double exponentials with time constants that differ by an order of magnitude. Figure 4.7.3 shows a plot of θ during cathode recovery following an oxygen exposure event.

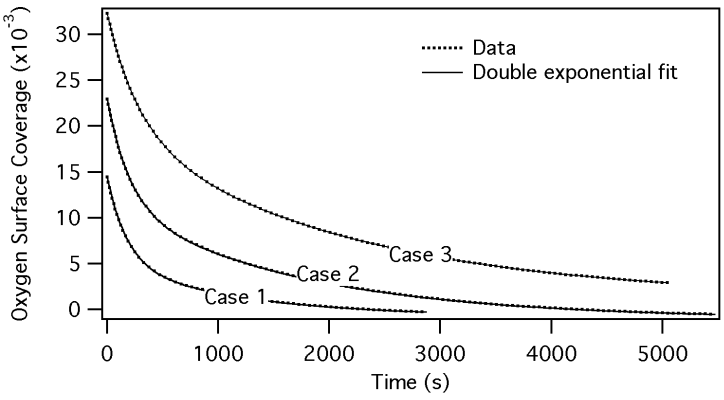

Figure 4.7.3: Plots of θ decay following oxygen exposure. The decays are best fit to double exponentials.

The double exponential fit seems to indicate that there are two main processes governing desorption of the oxygen from the barium surface. If there is significant oxygen gettering upstream, this oxygen may desorb from the surface and enter the gas phase after the oxygen flow valve is closed. This means that oxygen adsorption can still occur even though the oxygen flow is turned off, and the time constant for emptying oxygen from the plasma control volume will increase. The oxygen number density will decay as

$$n = n_0 e^{-t/\tau}. \tag{4.7.5}$$

Substituting $\Gamma_a = n\bar{c}/4 = n_0 \exp(-t/\tau)\bar{c}/4$ into Eq. (4.7.3) and solving for $\theta(t)$ gives

$$\theta(t) = e^{-\Gamma_d t/N_0}\left(\theta_0 + \frac{n_0\bar{c}}{4}\frac{\tau}{\Gamma_d\tau - N_0}\left(e^{(\Gamma_d\tau - N_0)t/\tau N_0} - 1\right)\right), \tag{4.7.6}$$

where $\theta(0) = \theta_0$. This equation is fit to the data given in Fig. 4.7.3. The values of each of the fit parameters are presented in Table 4.3.

The time constant for emptying the volume increases from case 1 to case 3 as given in Table 4.3. This is consistent with oxygen getting upstream as case 3 had the longest oxygen exposure, which allowed for more oxygen to adsorb on the upstream surfaces. This increases the oxygen emptying time as more oxygen is desorbed and released into the gas phase. The adsorption flux is similar to that determined in §4.7.1; however, the desorption rate is between 3 and 8 times higher. It is unclear what would cause this discrepancy in the values.

Table 4.3: Decay Fit Parameters

	Γ_a ($m^{-2}{\cdot}s^{-1}$)	Γ_d ($m^{-2}{\cdot}s^{-1}$)	Emptying time (s)
Case 1	$2.371 \times 10^{14} \pm 1.51 \times 10^{13}$	$4.037 \times 10^{16} \pm 1.40 \times 10^{15}$	663.03 ± 12.8
Case 2	$4.175 \times 10^{14} \pm 2.78 \times 10^{13}$	$3.519 \times 10^{16} \pm 1.65 \times 10^{15}$	1203.4 ± 21.0
Case 3	$2.371 \times 10^{14} \pm 3.52 \times 10^{12}$	$1.737 \times 10^{16} \pm 1.54 \times 10^{14}$	2592.6 ± 11.0

Haas et al. [35] adsorbed 10 L of O_2 onto an activated vacuum cathode surface and then heated the surface to 1180 K and allowed the oxygen to thermally desorb. At $t = 0$, the surface coverage of oxygen on top of the barium was unity. After 40 s the surface coverage was reduced to 0.6, and after 320 s the surface coverage was 0.3 [35]. Assuming second order desorption kinetics since the oxygen coverage is unity, the time-dependent change in θ is

$$\frac{d\theta}{dt} = -\frac{1}{N_0}\theta^2\Gamma_d. \tag{4.7.7}$$

The solution to this equation is

$$\theta(t) = \frac{\theta_0 N_0}{\theta_0 \Gamma_d t - N_0}, \tag{4.7.8}$$

where $\theta_0 = 1$. This equation is fit to the data given by Haas et al. [35] and yields a desorption flux of $\Gamma_d = 6.856 \times 10^{16} \pm 2.13 \times 10^{16}$, which corresponds to a desorption rate of 1.22×10^{-2} s^{-1}. There is a large error in this data as only three points were given for the surface coverage of oxygen during desorption; however, it can help be used to provide a check on our results. This value is comparable to those given in Table 4.3 and agrees well with the value used in the precursor model presented in §4.7.1. These results indicate that recovery following poisoning is largely the result of thermal desorption.

The thermal desorption flux is expressed as

$$\Gamma_d = N_0 A e^{-eE_b/kT}, \tag{4.7.9}$$

where A is a rate constant in s^{-1}, E_b is the surface binding energy in eV, and T is the surface temperature in K. Equation (4.7.9) is plotted in the form of A versus binding energy for the upper and lower bounds on the desorption flux calculated here. In general, the value of A can vary from 1×10^4 s^{-1} to 1×10^{23} s^{-1} [36]. The bond energy of the barium oxide molecule is 5.42 eV [37]. This provides an upper bound for the surface binding energy of O on Ba.

Horgan and Dalins studied oxygen adsorption onto stainless steel 304 and found that oxygen rapidly adsorbs on the surface at room temperature [38]. The total area of the stainless steel tubing

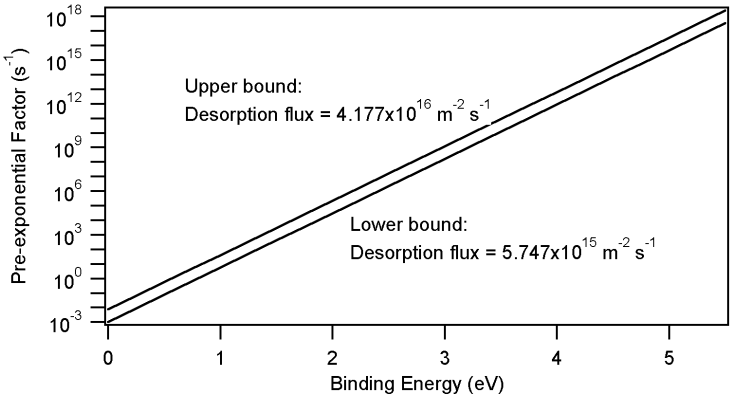

Figure 4.7.4: Plot showing how the pre-exponential factor varies with binding energy given the upper and lower bounds for the desorption flux calculated in this work.

in which the oxygen flows prior to reaching the cathode inlet is approximately 1×10^{-2} m^2. Assuming a surface density of 10^{18} sites/m^2, the stainless steel surfaces can hold on the order of 10^{16} oxygen molecules. If we assume that the flux of oxygen molecules at the entrance to the stainless steel tubing is 100 ppm of the xenon as prescribed by the experiment, then approximately 10^{13} molecules/s flow enter the tubing. Under these conditions, the stainless steel surfaces would fill up with oxygen in approximately 10^3 s.

This seems to agree with the data; however, long duration poisoning tests in which the cathode was exposed to oxygen for 500 h show the same slow transients [39]. It is unlikely that the stainless steel can getter oxygen for such a long period of time. The slow recovery times observed following an oxygen poisoning event indicate that oxygen remains in the plasma control volume for tens of minutes after the oxygen flow valve is closed. It is unclear why this occurs, and it is important to note that oxygen is not recycled in the gas in the same way that barium is recycled. This phenomenon may be the result of oxygen being released into the gas phase from an adsorbed state further upstream. The desorbed oxygen moves towards the orifice and readsorbs onto the downstream surfaces.

4.7.3 Effect of Ion Bombardment on Desorption

The goal of this section is to determine the dominant mechanism for desorption of atomic oxygen from the poisoning layer. The two main mechanisms considered are ion sputtering and thermal desorption. Bohdansky et al. [20] give an empirically derived relation for the sputter yield:

$$Y = 6.4 \times 10^{-3} m_2 \gamma^{5/3} E_i^{1/4} \left(1 - \frac{E_{th}}{E_i}\right)^{7/2}, \tag{4.7.10}$$

where Y is the yield in units of atoms desorbed per ion, m_2 is the mass of the target atom in amu, E_i is the ion bombardment energy, and E_{th} is the sputtering threshold energy as given in Eq.

(4.3.6). The yield equation given above was determined using empirical data for light ions such as helium [20], although it can be scaled for xenon ions by multiplying the equation by the ratio of the cross-sectional areas, r_{Xe}^2/r_{He}^2, where $r_{Xe} = 2.16$ Å and $r_{He} = 1.40$ Å are the van der Waals radii [40]. The sputtering cross section is given by $\sigma_s = Y/N_0$, where N_0 is the number density of oxygen atoms on the surface. A plot of the sputtering cross section for Xe^+ removal of O is given in Fig. 4.7.5 assuming $N_0 = 5.6 \times 10^{18}$ m^{-2} and that $E_{th} \ll E_i$ in order to give an upper bound.

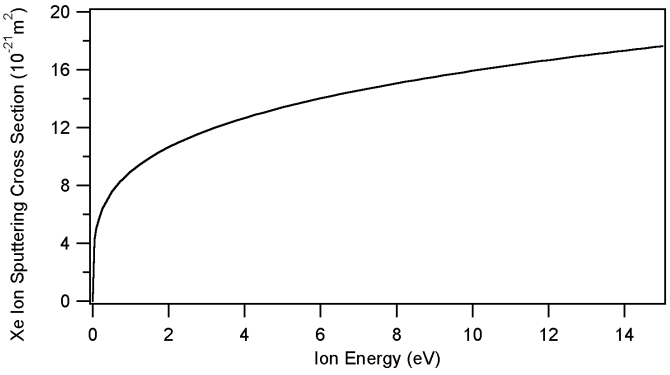

Figure 4.7.5: Cross section for xenon ion sputtering of oxygen.

The desorption flux due to sputtering is dependent on the xenon ion flux to the surface and can be expressed as

$$\Gamma_s = \sigma_s \Gamma_{Xe^+} N_0. \tag{4.7.11}$$

The ratio of the sputter removal rate to the thermal desorption rate can be determined by assuming a xenon ion flux of $\Gamma_{Xe^+} = 1 \times 10^{23}$ $m^{-2} \cdot s^{-1}$ calculated from the xenon plasma model, an ion energy of 15 eV, and a surface temperature of 1350 K. Figure 4.7.6 shows curves on which the sputter removal rate equals the thermal desorption rate, i.e., $\Gamma_S/\Gamma_{td} = 1$, on a plot of A versus E_b for different values of the sputtering threshold energy. These lines represent boundaries between regions where one process or the other dominates. Note that $E_{th} = E_b/\gamma$ is very conservative. The sputtering threshold energy proposed by Bohdansky et al. in Eq. (4.3.6) is so small that it does not appear on the graph. Sputtering dominates over thermal desorption for values of A and E_b that fall below these curves. The dashed lines in Fig. 4.7.6 represent the curves shown previously in Fig. 4.7.4.

The values of E_{th} used in Eq. (4.7.10) and in Fig. 4.7.6 are conservative, and therefore, sputtering may not be as important as thermal desorption for the temperatures and ion energies in these cathodes. Additionally, an ion energy of 15 eV was used in the preceding calculations, which is also a conservative estimate. In order to distinguish between the effects of sputter and thermal desorption, a final experiment was performed at the same emitter temperature, but different discharge currents. The results of this experiment will be discussed in the following section.

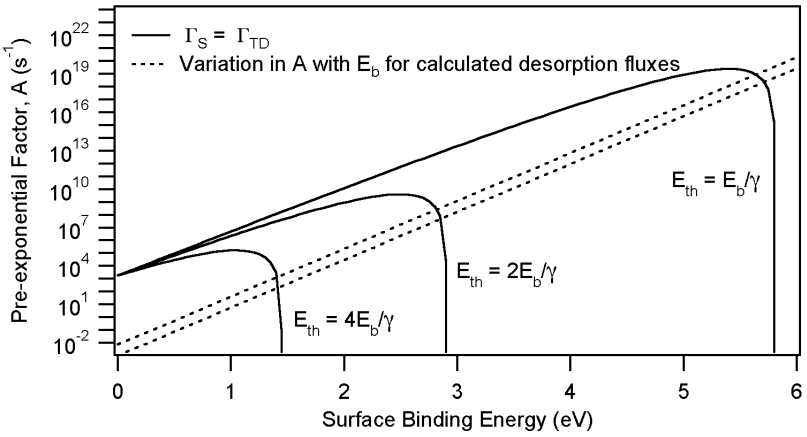

Figure 4.7.6: Curves of $\Gamma_s/\Gamma_{td} = 1$ on a plot of A versus E_b for different values of the sputtering threshold energy. The dashed lines represent the values of A and E_b that will yield the bounding values of the thermal desorption fluxes given in §4.7.1 and Table 4.3.

4.8 Separating the Effects of Ion Sputtering and Thermal Desorption via Experimentation at $J_D = 6$ and 10 A

The goal of this experiment is to understand how the plasma parameters affect cathode poisoning and recovery independent of temperature. In order to distinguish between the effects of temperature and the plasma properties, an external heater is used to match the emitter temperatures at two different discharge currents. In this experiment, the cathode was operated at 6 A of discharge current and a xenon flow rate of 2.5 sccm. Measurements of the emitter temperature were obtained at 6 A without the heater and are plotted as the bottom curve in Fig. 4.8.1. The cathode heater was then used to reproduce the normal operating temperatures of the 10 A case, but at 6 A of discharge current. The temperature profiles for the 6 and 10 A cases are shown in Fig. 4.8.1. Note that at lower discharge currents there is less particle bombardment of the surface and the normal operating temperatures are lower.

The use of the heater increased the emitter temperatures at 6 A by approximately 56 K. The heater current and potential needed to obtain this temperature increase were 5.8 A and 7.3 V, respectively. The increase in emitter temperature will increase the emission current density, and in order to maintain constant total current, the reverse electron current must also increase. This results in a drop in the sheath potential from its initial value without the heater, which we observe as a change in the discharge potential. During normal operation at 6 A without heater current, the discharge potential was constant at 18.65 V. Once the heater was turned, on the discharge potential dropped by 1.4 V.

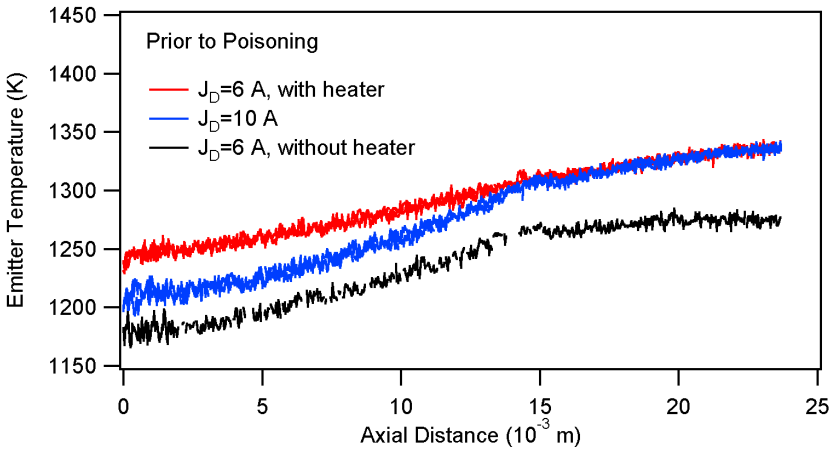

Figure 4.8.1: Temperature profiles of the cathode during operation at 6 A with heater and 10 A without heater.

Plasma simulations for the 6 A case do not currently exist for this cathode, but modeling of the 10 A case at two different temperatures can provide a qualitative understanding of how the plasma parameters change during active heating. Figure 4.8.2 shows plots of the sheath potential, electron temperature, and plasma density along the emitter surface calculated from the xenon plasma model for a low temperature case and a high temperature case [33]. The low temperature case is given by the temperature profile shown in Fig. 4.6.1a, and the high temperature case is the same profile offset by $^{+}25$ K. From these plots it is evident that the sheath potential is the parameter most sensitive to changes in the temperature. The electron temperature and plasma density also drop slightly. A reduction in the ion current will reduce xenon ion sputtering of the oxygen during poisoning. This helps to further distinguish between the plasma effects at 6 and 10 A.

Note from Fig. 4.8.1 that the temperatures for the 6 A case with heater match the 10 A case at axial distances greater than $z = 1.4$ cm, but diverge at axial locations upstream of this. The emission current for the 6 A case with heater is approximately 13.6% higher than the 10 A case as a result of the increased temperatures between $z = 0$ and $z = 1.4$ cm. This increase in emission current should further reduce the sheath potential.

The cathode was exposed to 100 ppm of oxygen for 15 minutes during operation at 6 A with heater current. The orifice plate and emitter temperatures were recorded during the exposure. Plots of the emitter temperature profiles are shown in Fig. 4.8.3. The shape of each temperature profile during poisoning remained the same as that prior to poisoning. The only difference between the profiles in Figs. 4.8.1 and 4.8.3 is a temperature offset. Plots of the orifice plate temperatures are shown in Fig. 4.8.4. The discharge potential at 6 A did not change during poisoning.

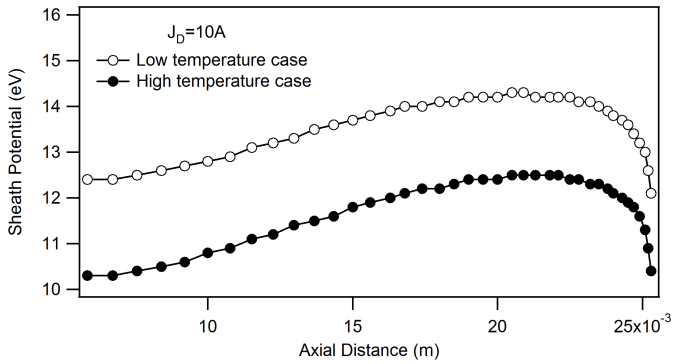

(a) Variation in sheath potential with distance.

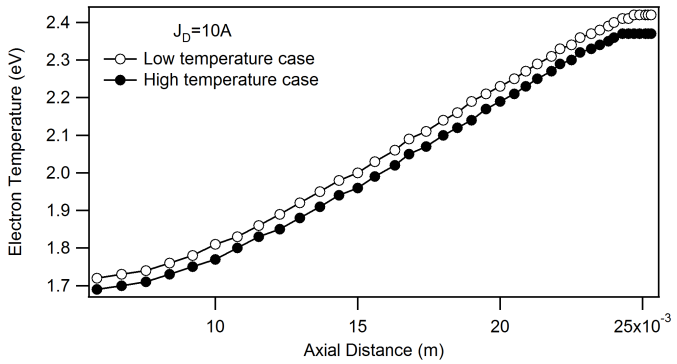

(b) Variation in electron temperature with distance.

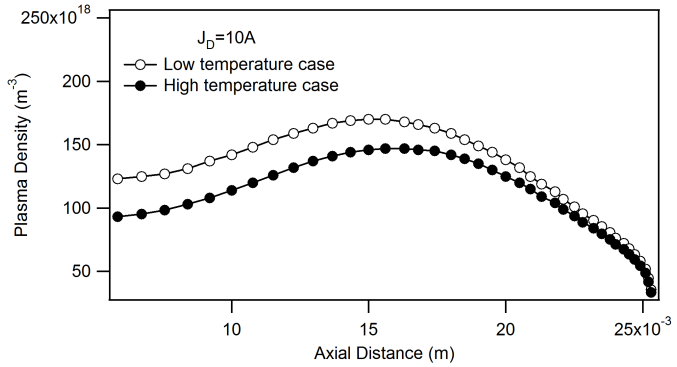

(c) Variation in plasma density with distance.

Figure 4.8.2: Plasma parameters along the emitter surface for 10 A, 2.5 sccm. The low temperature profile is given in Fig. 4.6.1a. The difference in temperature between the two cases is 25 K.

Recall from Figs. 2.4.1 and 4.5.3 that the emitter temperature varies linearly with the orifice plate temperature according to $T = a\zeta + b$, where ζ represents the orifice plate temperature and a and b are the fit parameters. The curves for the 6 and 10 A cases shown in Fig. 4.8.4 can be compared by scaling the emitter temperature by the difference between the initial and maximum temperatures:

$$\frac{T - T_0}{T_{\max} - T_0} = \frac{(a + \zeta b) - (a + \zeta_0 b)}{(a + \zeta_{\max} b) - (a + \zeta_0 b)} = \frac{\zeta - \zeta_0}{\zeta_{\max} - \zeta_0}, \tag{4.8.1}$$

where T_0 is the temperature prior to poisoning at $t = 0$ and T_{max} is the temperature reached at the crest of the poisoning curves at $t = 900$ s. It is necessary to perform this scaling because a reliable curve fit relating emitter temperature with orifice plate temperature could not be obtained for the 6 A case with heater, as only two measurements of the emitter temperature were taken during poisoning. The variation in the scaled temperature with time is shown in Fig. 4.8.5.

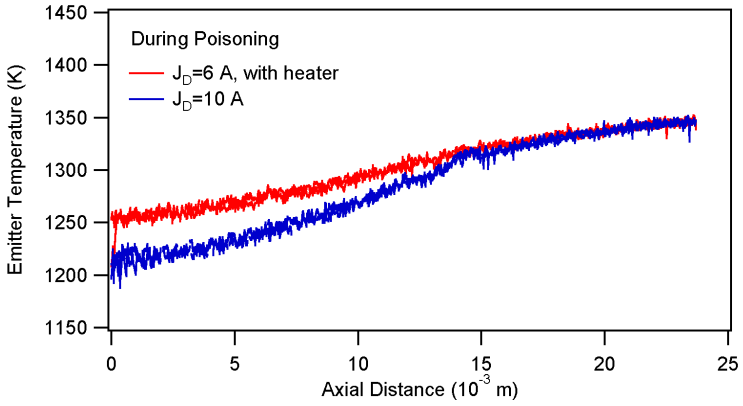

Figure 4.8.3: Temperature profiles of the cathode following 15 min of oxygen exposure at 100 ppm.

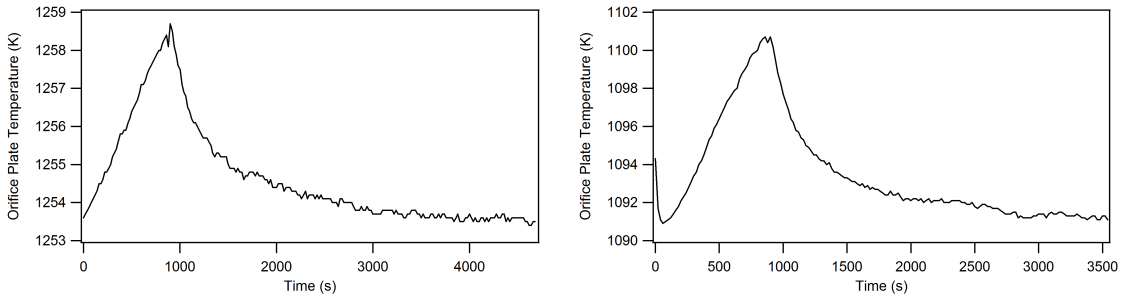

(a) Orifice plate temperatures for 6 A case with heater. (b) Orifice plate temperatures for 10 A case.

Figure 4.8.4: Change in orifice plate temperature during poisoning and recovery.

The two different cases appear to poison and recover at the same rate. Changes in the ion bombardment energy and flux between the 6 and 10 A cases may not have a significant effect on the sputtering of the O_2 precursor since the bond energy is so low. However, the results seem to indicate that desorption of atomic oxygen following the poisoning event is largely governed by thermal processes.

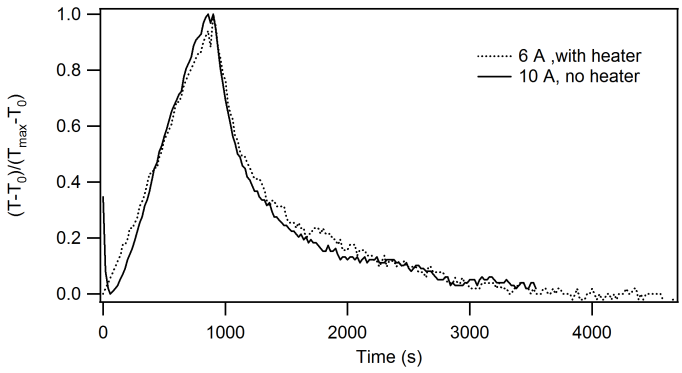

Figure 4.8.5: Plots of the emitter temperatures scaled by $(T_{\max} - T_0)$ for the 6 and 10 A cases.

4.9 Coupling the Reaction Kinetics Model with the Transport Model

Based on the work presented here thus far, it is clear that the surface state of the emitter changes with time and is influenced by the oxygen flux to the surface and the thermal desorption rate. Temperature, density, and particle flux are parameters extracted from the gas phase transport model, however, and these values are also informed by the prescribed boundary conditions. Consequently, it is important for the boundary conditions at the emitter surface to be allowed to change as the surface state evolves. The goal of this section is to use the reaction kinetics model and the results presented earlier in this chapter to write a set of time-dependent equations for the boundary conditions at the emitter surface. Recall that static boundary conditions were implemented in the transport model described in Chapter 3 and that very different gas solutions resulted for the two chosen cases.

In this revised version of the transport model, all boundary conditions presented in Chapter 3 hold except those at the emitter. This model was intially run with only Ba and BaO assuming no accumulation of either species on the surface. This was done prior to oxygen exposure in order to simulate the cathode conditions prior to oxygen poisoning as discussed in §3.5. Once this model came to equilibrium, the equilibrium barium coverage was calculated by setting Eq. (4.3.8) to zero and solving for θ_{Ba}. The results were presented previously in Fig. 4.3.2.

At the start of the oxygen exposure, θ_O and θ_p were set to zero and the values of $d\theta_O/dt$ and $d\theta_p/dt$ were calculated using Eqs. (4.4.9) and (4.4.12) assuming $\theta^* = 1$ and $k_a = \Gamma_{O_2}/N_0$. The net ion fluxes at the surface are the same as that given in Chapter 3 and are repeated here:

$$\mathbf{\Gamma}_i = n_i \left(\frac{kT_e}{m_i} \right)^{1/2} \hat{\mathbf{r}}. \tag{4.9.1}$$

Since the surface is no longer in steady state, the net flux of ions and neutrals to the surface

contributes to the accumulation of atoms on the surface. The emitter boundary can therefore be modeled as

$$\mathbf{\Gamma}_{Ba} = N_0 \frac{d\theta_{Ba}}{dt} - \mathbf{\Gamma}_{Ba^+} - \mathbf{\Gamma}_{s,Ba}, \tag{4.9.2}$$

$$\mathbf{\Gamma}_{O_2} = N_0 \left[\left(\frac{d\theta_O}{dt} \right)_{O_2} + \theta_{Ba} \left(\frac{d\theta_p}{dt} \right)_{O_2} \right] - \mathbf{\Gamma}_{O_2^+}, \tag{4.9.3}$$

where $(d\theta_O/dt)_{O_2}$ is the contribution to the change in oxygen coverage in the second layer due to O_2 and $(d\theta_p/dt)_{O_2}$ is the contribution to the change in oxygen coverage of the poisoning layer due to O_2. This means that $(d\theta_O/dt)_{O_2}$ and $(d\theta_p/dt)_{O_2}$ account only for dissociative adsorption and associative desorption, i.e., $O_2(g) + 2S^* \rightleftharpoons 2O^*$. A similar expression can be written for atomic oxygen

$$\mathbf{\Gamma}_O = N_0 \left[\left(\frac{d\theta_O}{dt} \right)_O + \theta_{Ba} \left(\frac{d\theta_p}{dt} \right)_O \right] - \mathbf{\Gamma}_{O^+}. \tag{4.9.4}$$

By using these relations, we can account for changes in the number densities depending on what is lost from or added to the gas phase. The direction of the neutral particle velocity vector was coded to coincide with the direction of the net neutral flux. The magnitude of the neutral particle velocity was assumed to be the thermal velocity. BaO adsorption and desorption from the surface was neglected in this model as the number densities were low.

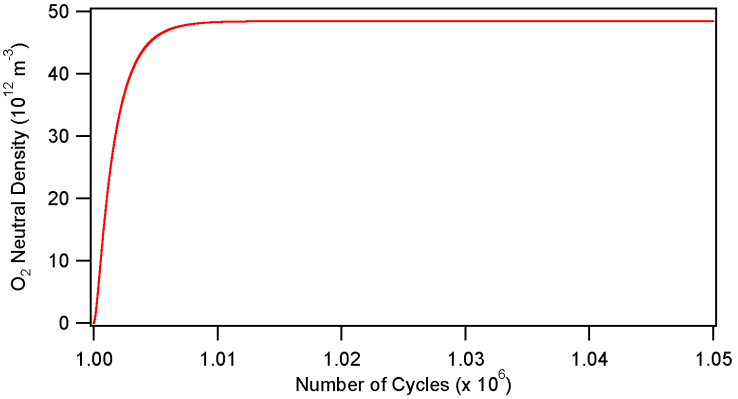

Figure 4.9.1: The neutral O_2 density increases strongly over the first 10^4 cycles then reaches equilibrium.

In order to save computing time, the surface coverage is not updated at each time step. This method is justified because the boundary conditions do not change much during the large transients in the number density. An example of this is shown in Fig. 4.9.1. The number density increases steeply over the first 10^4 cycles. The values of θ_O and θ_p are on the order of 10^{-7} during this

transient. The surface coverages were time marched using

$$\theta_{\text{new}} = \theta_{\text{old}} + \Delta t \frac{d\theta}{dt} \tag{4.9.5}$$

for a time step of $\Delta t = 5 \times 10^{-4}$ s. A total of 1×10^4 steps were used to evolved θ. It was then held fixed and the gas was allowed to adjust to these boundary conditions. This process was repeated for a predetermined amount of time.

A plot of the oxygen coverage in the poisoning layer is shown in Fig. 4.9.2 as a function of distance and time for 100 ppm of oxygen in the discharge. Only the emitter was modeled here, and the surface quickly saturates with oxygen in several seconds. The coverage profile starts out at $\theta_p = 0$ along the whole length of the emitter. At the start of oxygen poisoning there is a steep gradient in the oxygen number density with distance, and therefore, the upstream sites fill first. As these sites saturate, the gradient in oxygen number density decreases and surface sites further downstream begin to fill with oxygen. The coverage approaches unity and the entire length of the emitter surface becomes saturated with oxygen. The results presented here show the capability of the model and highlight how the surface fills with oxygen as it is fed into the plasma control volume through the upstream inlet.

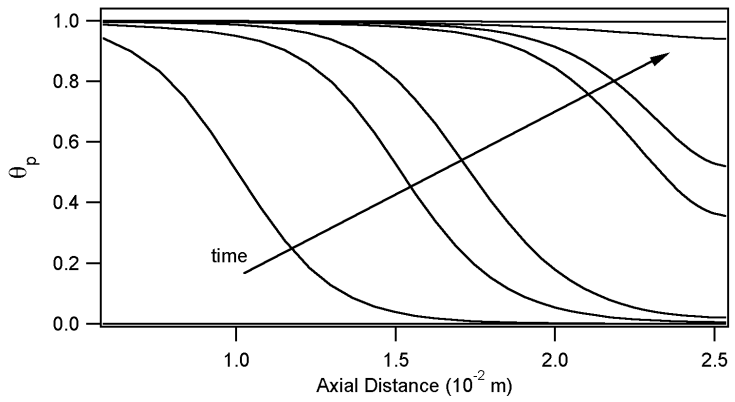

Figure 4.9.2: The evolution of oxygen coverage in the poisoning layer with time and distance. The results shown are for 100 ppm of O_2. It takes several seconds for the surface to become saturated.

4.10 Conclusions

The Ba/O/W surface has a low work function because the barium oxide dipole reduces the potential barrier for electron extraction. When oxygen is adsorbed on top of the Ba/O/W surface, the dipole is disturbed and the work function increases rapidly. Changes to the surface work function appear as changes in the emitter temperature and/or emission current density. Although the total current is

fixed during cathode experiments, it was shown that the emission current remains relatively constant, and therefore, the temperature adjusts to maintain the current density during poisoning.

Cathode heating occurs via particle bombardment, and since the reverse electron emission decreases during poisoning, the ion current density must increase in order to give the observed temperature rise. However, the ion current density is held fixed in our calculations as we do not have modeling results that allow it to vary during oxygen exposure. This highlights the need for the coupling of the plasma and transport models so that the plasma parameters can be calculated self-consistently.

Measurements of the emitter temperature were used to infer the surface state. The resulting oxygen poisoning coverages were small, and the rate of increase in the oxygen coverage was slow, indicating some rate-limiting process. A simple kinetics model showed that ion sputtering of the weakly bound O_2 precursor limits the poisoning rate if the sputter rate is fast compared with the dissociative chemisorption rate. The dominant processes at the surface are dissociative oxygen adsorption, sputtering of the O_2 precursor, and desorption of atomic oxygen in the poisoning layer. Further work must be completed to obtain fundamental atomic data on these processes in order to validate the model.

The decay in oxygen coverage is characterized by two processes. The fast process is thermal desorption; the slow process indicates that oxygen may remain in the cathode after the oxygen valve is closed. This could be the result of oxygen gettering upstream in the stainless steel tubes. This is a relevant and important conclusion as flight systems typically employ stainless steel feedlines, and further work must be done to understand this process.

The effects of ion sputtering and thermal desorption of atomic oxygen were separated by conducting experiments at two different discharge currents, giving different ion fluxes and bombardment energies. The operating temperatures of the two cases were matched using an external heater. The rate of desorption of atomic oxygen in the poisoning layer was the same in both cases, indicating that recovery following oxygen poisoning is governed by thermal processes.

The desorption energy of oxygen on barium was not determined here as there was not enough variation in the temperatures to accurately construct the necessary Langmuir isotherms; however, the desorption rate was determined to be consistent with data from Haas et al. [35] for vacuum cathodes. Model experiments can be conducted in the future to determine the binding energy.

The results of this analysis allowed us to construct a set of boundary conditions at the emitter surface that vary with time. This is significant in that it allows for the gas solution and the emitter surface state to be determined self-consistently.

Bibliography

[1] G. Rhead, "On the variation of work function with coverage for alkali-metal adsorption," *Surf. Sci.*, vol. 203, pp. L663–L671, 1988.

[2] B. Lamartine, J. Czarnecki, and T. Haas, "Coadsorption of Ba and O on polycrystalline W," *Appl. Surf. Sci.*, vol. 26, pp. 61–76, 1986.

[3] D. Gorodetsky and Y. Melnik, "Barium on (110) tungsten," *Surf. Sci.*, vol. 62, pp. 647–661, 1977.

[4] A. Lamouri, I. Krainsky, and W. Muller, "Electronic structure and work function study of a model dispenser cathode surface," *Surf. Interf. Anal.*, vol. 21, pp. 150–154, 1994.

[5] D. Gorodetsky, Y. Melnik, D. Proskurin, V. Skylar, V. Usenko, and A. Yas'ko, "Barium films on molybdenum(110): LEED and EELS study," *Surf. Sci.*, vol. 416, pp. 255–263, 1998.

[6] O. Teodoro, J. Los, and A. Moutinho, "Anomalous growth of Ba on Ag 111," *J. Vac. Sci. Technol. A*, vol. 20, no. 4, pp. 1379–1383, 2002.

[7] G. Magera and P. Davis, "Interaction of cesium and barium on partially oxygen covered Nb(110)," *J. Vac. Sci. Technol. A*, vol. 11, no. 4, pp. 2336–2341, 1993.

[8] R. Gurney, "Theory of electrical double layers in adsorbed films," *Phys. Rev.*, vol. 47, pp. 479–482, 1935.

[9] E. Gyftopoulos and J. Levine, "Work function variation of metals coated by metallic films," *J. Appl. Phys.*, vol. 33, pp. 67–73, 1962.

[10] C. Papageorgopoulos and J. Chen, "Coadsorption of electropositive and electronegative elements II. Cs and O_2 on W(100)," *Surf. Sci.*, vol. 39, pp. 313–332, 1973.

[11] D. Gorodetsky and A. Knysh, "The study of structure and work function on barium oxide films and the Ba-O double system on the (0001) face of rhenium II. Double Ba-O-Re (0001) system," *Surf. Sci.*, vol. 40, pp. 651–668, 1973.

[12] G. Pirug, G. Broden, and H. Bonzel, "Coadsorption of potassium and oxygen on Fe(110)," *Surf. Sci.*, vol. 94, pp. 323–338, 1980.

[13] R. Forman, "Correlation of electron emission with changes in the surface concentration of barium and oxygen on a tungsten surface," *Appl. of Surf. Sci.*, vol. 17, pp. 429–462, 1984.

[14] A. Shih, J. Yater, and C. Hor, "Ba and BaO on W and on Sc_2O_3 coated W," *Appl. Surf. Sci.*, vol. 242, pp. 35–54, 2005.

[15] G. Haas, R. Thomas, C. Marrian, and A. Shih, "Rapid turn-on of shelf-stored tubes: An update," *IEEE Transactions on Electron Devices*, vol. 38, no. 10, pp. 2244–2251, 1991.

[16] P. Schissel and O. Trulson, "Mass-spectrometric study of the oxidation of tungsten," *J. Chem. Phys.*, vol. 43, no. 2, pp. 737–743, 1965.

[17] J. Slater, "Atomic radii in crystals," *J. Chem. Phys.*, vol. 41, pp. 3199–3204, 1964.

[18] J. Gibson and R. Thomas, "Surface plasmon studies of oxidized Ba films," *Appl. Surf. Sci.*, vol. 16, pp. 163–180, 1983.

[19] R. Behrisch and W. Eckstein, Eds., *Sputtering by Particle Bombardment*. Springer, 2007.

[20] J. Bohdansky, J. Roth, and H. L. Bay, "An analytical formula and important parameters for low-energy ion sputtering," *J. Appl. Phys.*, vol. 51, no. 5, pp. 2861–2865, 1980.

[21] R. Doerner, G. Tynan, E. Oyerzabal, K. Taylor, D. Goebel, and I. Katz, "Plasma surface interaction studies for next-generation ion thrusters," in *40th AIAA Joint Propulsion Conference*, Fort Lauderdale, FL, 2004, AIAA-2004-4104.

[22] V. Ageev, Y. Kuznetsov, and N. Potekhina, "Electron-stimulated desorption of alkali metal and barium atoms from an oxidized tungsten surface," *Surf. Sci.*, vol. 367, pp. 113–127, 1996.

[23] R. Forman, "Surface studies of barium and barium oxide on tungsten and its application to understanding the mechanism of operation of an impregnated tungsten cathode," *J. Appl. Phys.*, vol. 47, p. 5272, 1976.

[24] A. Zangwill, *Physics at Surfaces*. Cambridge University Press, 1988.

[25] H. Kang and W. Weinberg, "Kinetic modeling of surface rate processes," *Surf. Sci.*, vol. 299, pp. 744–768, 1994.

[26] E. German and I. Efremenko, "Calculation of the activation energies of dissociative oxygen adsorption on the surfaces of rhodium (111), silver (111) and (110), and gold (111)," *J. Mol. Struc.*, vol. 711, pp. 159–165, 2004.

[27] J. Bittencourt, *Fundamentals of Plasma Physics*. Springer-Verlag New York, 2004.

[28] D. Goebel and I. Katz, *Fundamentals of Electric Propulsion: Ion and Hall Thrusters*. John Wiley & Sons, 2008.

[29] A. Da Rosa, *Fundamentals of Renewable Energy Processes*. Elsevier, 2009.

[30] I. Mikellides, I. Katz, D. Goebel, J. Polk, and K. Jameson, "Plasma processes inside dispenser hollow cathodes," *Phys. of Plasmas*, vol. 13, p. 063504, 2006.

[31] J. Cronin, "Modern dispenser cathodes," *Proc. IEEE*, vol. 128, no. 1, pp. 19–32, 1981.

[32] A. Kumar, *Introduction to Solid State Physics*. PHI Learning Private Limited, 2010.

[33] I. Mikellides, I. Katz, D. Goebel, and J. Polk, "Hollow cathode theory and experiment. II. A two-dimensional theoretical model of the emitter region," *J. Appl. Phys.*, vol. 98, p. 113303, 2005.

[34] I. Katz, I. Mikellides, J. Polk, D. Goebel, and S. Hornbeck, "Thermal model of the hollow cathode using numerically simulated plasma fluxes," *J. Prop. P.*, vol. 23, no. 3, pp. 522–527, 2007.

[35] G. Haas , R. Thomas, C. Marrian, and A. Shih, "Surface characterization of BaO on W, II. Impregnated cathodes," *Appl. Surf. Sci.*, vol. 40, pp. 277–286, 1989.

[36] A. Balogh, L. Ksanfomality, and R. von Steiger, Eds., *Mercury*. Springer Science+Business Media, BV, 2010.

[37] K. Schofield, "The bond dissociation energies of group IIA diatomic oxides," *Chem. Rev.*, vol. 67, no. 6, pp. 707–715, 1967.

[38] A. Horgan and I. Dalins, "Adsorption of hydrogen, carbon monoxide, and oxygen on vacuum degassed stainless steel 304 at 20°c," *J. Vac. Sci. Technol.*, vol. 10, no. 4, pp. 559–561, 1973.

[39] J. Polk, "Long and short term effects of oxygen exposure on hollow cathode operation," in *43rd AIAA Joint Propulsion Conference*, Cincinnati, OH, 2007, AIAA-2007-5191.

[40] A. Bondi, "van der Waals volumes and radii," *J. Phys. Chem.*, vol. 68, no. 3, pp. 441–451, 1964.

Chapter 5

Conclusions

The goal of this work was to understand how oxygen impurities in the xenon discharge plasma alter the emission properties and affect operation of a 4:1:1 BaO-CaO-Al_2O_3 hollow cathode. A significant amount of work has been done previously to understand the effects of oxygen poisoning on vacuum cathodes; however, the xenon plasma adds complexity and its role during cathode poisoning was not completely understood. This work represents the first detailed investigation of oxygen poisoning in plasma cathodes and a combination of experimentation and modeling was used to investigate this issue. The main conclusions of this work will be summarized and the recommendations for further work will be outlined here.

5.1 Summary of Major Results

When barium atoms are adsorbed on an oxygen-covered tungsten substrate, a barium oxide dipole (Ba^+O^-) is formed that reduces the work function to less than 2.1 eV. Oxygen that adsorbs on top of this Ba/O/W multilayer system disturbs the dipole and causes the work function to increase with oxygen coverage by as much as 0.8 eV. The increase in work function drives up the emitter temperature, which increases evaporation of the emission materials and reduces cathode life. Once the barium supply in the cathode interior is exhausted, the work function will be too high to sustain the required emission current and the cathode will fail. Therefore, it is crucial to maintain low temperatures in the cathode.

Experiments were performed on a 4:1:1 hollow cathode operated at various conditions and with oxygen impurities in the xenon flow. The emitter temperature was measured using a two-color pyrometer and was found to vary linearly with the orifice plate temperature measured once per second with two type B platinum-rhodium thermocouples. Poisoning was observed as an increase in temperature and occurred over a range of discharge currents between 6 and 12 A and for oxygen concentrations as low as 10 ppm. Once the cathode flow valve was closed, the temperatures decayed to their initial pre-poisoned values, indicating that the changes made to the surface state during

poisoning are not permanent.

A model describing the material transport in the plasma discharge was developed to predict the barium and oxygen fluxes to the emitter surface during cathode operation by solving the species continuity and momentum equations. Gas phase barium, oxygen, and tungsten species are found in small concentrations in the xenon plasma, and it is important to consider the transport of these minor species as they may deposit on the emitter surface and alter the electron emission properties. The flow of these particles in the discharge is governed by the conservation equations and interactions with the xenon plasma. Key physical interaction processes include collisions with electrons, xenon ions, and xenon neutrals resulting in momentum transfer, charge exchange, recombination, and ionization. The dominant ionization process for O_2 molecules was resonant charge exchange with xenon ions. The oxygen was also allowed to interact with barium atoms to form barium oxide; however, since the reactant concentrations were small, very little barium oxide was formed as a result of such chemical reactions.

The simulations showed that steep gradients in oxygen number density occur with axial distance early on in poisoning. Once the upstream surfaces saturate with oxygen, the gradient in oxygen number density decreases and surface sites further downstream begin to fill with oxygen. When the entire length of the emitter surface becomes saturated with oxygen so that no further accumulation can occur, the oxygen number density equilibrates at a uniform value consistent with the prescribed concentration. Not much of the neutral O_2 population is lost to ionization and oxygen is not recycled in the gas in the same way that barium is recycled. All neutrals that escape ionization exit the cathode through the orifice. Additionally, the model did not reveal any process that would limit the oxygen flux to the surface.

Further experiments were conducted to infer the surface state using the emitter temperature measurements. It was determined that less than 3% of the surface was covered with oxygen during poisoning and the time constant for poisoning was 10^3 s. The long transients in the uptake curve indicate some rate-limiting process. A simple kinetics model showed that ion sputtering of the weakly bound O_2 precursor limits the poisoning rate if the sputter rate is fast compared with the dissociative chemisorption rate. The dominant processes at the surface are dissociative oxygen adsorption, sputtering of the O_2 precursor, and desorption of atomic oxygen in the poisoning layer. Further work must be completed to obtain fundamental atomic data on these processes in order to validate the model.

The decay in oxygen coverage is characterized by two processes. The fast process is thermal desorption; the slow process indicates that oxygen may remain in the cathode after the oxygen valve is closed. This could be the result of oxygen gettering upstream in the stainless steel tubes. Previous studies have shown that oxygen rapidly adsorbs on stainless steel 304 at room temperature. The area of the stainless steel tubing used in the oxygen flow system is sufficient to absorb on the order

of 10^{16} oxygen molecules. Given the flux at the entrance to the tubing, the stainless steel surfaces would fill up with oxygen in approximately 10^3 s.

The slow recovery times observed following an oxygen poisoning event indicate that oxygen remains in the plasma control volume for tens of minutes after the oxygen flow valve is closed. This phenomenon is most likely the result of oxygen being released into the gas phase from an adsorbed state further upstream. The desorbed oxygen moves toward the orifice and readsorbs onto the downstream surfaces. This increases the residence time of oxygen in the cathode. Flight systems typically employ stainless steel feedlines, and thus, it may be important to consider this piece of the system in further experiments and models.

The experimental results also indicate that desorption of atomic oxygen on the emitter surface is dominated by thermal processes, and xenon ion sputtering is negligible in comparison because of the low ion energies in the cathode. Using the experimental results, a time-dependent model of the reaction kinetics of oxygen and barium at the tungsten surface was developed to describe the adsorption and desorption processes that occur at the emitter surface during poisoning.

The desorption energy of oxygen on barium was not determined here as there was not enough variation in the temperatures to accurately construct the necessary Langmuir isotherms; however, the desorption rate was determined to be consistent with data from experiments with vacuum cathodes. Model experiments can be conducted in the future to determine the binding energy.

The results of this analysis allowed us to construct a set of boundary conditions at the emitter surface that vary with time. This is significant in that it allows for the gas solution and the emitter surface state to be determind self-consistently.

5.2 Recommendations For Future Work

The development of the transport model was a significant achievement in understanding oxygen poisoning in cathodes; however, we could better determine the effects of oxygen contaminants on the plasma parameters if the transport model was merged with the xenon plasma model. Solving these two concurrently would allow for all parameters to be calculated self-consistently.

At present, the xenon plasma model calculates the work function using a simple temperature-dependent model; however, the work function actually varies with barium and oxygen coverage. Variability in the experiments is not captured by the xenon plasma model since the surface coverage and its effect on work function are not taken into account. Ideally, the plasma, transport, and reaction kinetics models would be solved concurrently so that changes to the plasma gas and the emitter surface constantly inform each other.

Other recommendations regarding the modeling effort include performing diagnostics on the transport model to work out the convergence issues so that more cathode operating conditions can

be simulated. It would also be interesting to simulate the 6 A case with heater to determine how different the plasma parameters are at this condition compared with the 10 A case. Tungsten oxide species can also be added to the transport model. This may be important as previous studies have shown tungsten oxide deposits on the emitter surface.

The focus of this work was on how short exposures to oxygen affect cathode operation; however, it would also be interesting to initiate a study into what occurs when oxygen is present in the plasma discharge for thousands of hours. The development of a thermochemistry model would help determine what compounds form over time and how they affect electron emission.

Recommendations regarding the experimental effort include performing simple experiments to construct an Arrhenius plot for the desorption of oxygen on barium using an activated hollow cathode in vacuum. Previous work on oxygen poisoning in vacuum cathodes has been done, but no data on the rate constant and desorption energy exist to the author's knowledge. Additionally, further work must be performed to determine the rate constants for dissociative oxygen chemisorption on a Ba/O/W surface and the yield for xenon ion sputtering of the O_2 precursor. Finally, further work to understand oxygen gettering on stainless steel is recommended. Adsorption and desorption experiments can be performed to describe the kinetics that occur in the feedlines before oxygen enters the plasma discharge. Future cathode experiments could include less stainless steel tubing, which may be achieved by extending the fused silica capillary tubes closer to the cathode inlet.

Appendix A

X-ray Photoelectron Spectroscopy of $BaWO_4$ and Ba_2CaWO_6

The goal of the work presented here was to conclusively determine the presence of $BaWO_4$ and Ba_2CaWO_6 in the cathode following oxygen exposure using x-ray photoelectron spectroscopy (XPS). XPS is a surface chemical analysis technique that determines elemental composition, chemical state, and electron configuration. XPS spectra are obtained by bombarding a sample with x-rays and measuring the kinetic energy of the emitted electrons. The kinetic energy then determines the binding energy, which can be used in conjunction with published tables to determine what chemical species are present. XPS reference spectra were first taken for $BaWO_4$ and Ba_2CaWO_6. The results of the XPS analysis on these two species, which are summarized here, show that it may be difficult to distinguish between these two species and other barium compounds.

X-ray photoelectron spectra were obtained for $BaWO_4$ and Ba_2CaWO_6 using an M-Probe XPS system with monochromatic Al Kα X-rays (1486.6 eV). The samples were analyzed under UHV at a base pressure of 10^{-9} Torr. The binding energies for the most intense barium (Ba $3d$), tungsten (W $4f$), calcium (Ca $2p$), and oxygen (O $1s$) lines were measured. Binding energies were calibrated by measuring the binding energy of a gold foil and setting the binding energy of the Au $4f_{7/2}$ line to 83.8 eV. The measured spectra for each tungstate sample were referenced to the C 1s line (284.6 eV).

The tungstate samples analyzed in this work are 99.9% purity powders of $BaWO_4$ and Ba_2CaWO_6 pressed into indium foil. The indium was etched in a solution of 10% HCl by volume for 5 minutes at room temperature in order to remove oxides from the surface. The indium was rinsed twice in 18 M$\Omega\cdot$cm deionized water and then rinsed with acetone. The samples were not electrically conductive, and therefore, charge compensation was necessary. Following the procedure presented by Vasquez, a low energy flood gun was used to eliminate charging effects, and a 90% transmitting mesh screen was mounted approximately 1.5 mm above the sample to improve electron optics [1].

Peak-fitting software (Igor Pro) was used to calculate the peak locations and areas from the high-

resolution data. The photoemission spectrum contains background noise, which occurs as a result of scattering events [2]. The peak-fitting software will fit a baseline to adjust for this background.

Table A.1: Peak Positions for $BaWO_4$ and Ba_2CaWO_6.

	$BaWO_4$		Ba_2CaWO_6	
Line	Peak Location (eV)	Peak Width (eV)	Peak Location (eV)	Peak Width (eV)
W $4f_{7/2}$	35.2	1.77	34.8	1.61
W $4f_{5/2}$	37.3	1.74	37.0	1.43
Ca $2p_{3/2}$	—	—	346.8	3.46
Ca $2p_{1/2}$	—	—	350.3	2.14
O $1s$	530.6	2.01	530.9	2.64
Ba $3d_{5/2}$	780.0	2.29	779.6	1.40
Ba $3d_{3/2}$	795.3	2.28	794.9	1.54

Element identification and electronic configuration can be determined by the location of the peak; however, it is important to note that peaks may be shifted due to surface charging or chemical bonding. The binding energy increases if a valence electron is withdrawn, and decreases if a valence electron is added. If the surface under analysis is an insulator, positive charge is generated by photoemission causing the peaks to shift to higher binding energies [3]. To determine the shift due to charging of the surface, a reference peak must first be identified. The reference peak to be used for this analysis is carbon 1s, which corresponds to a binding energy of 284.6 eV. Table A.1 lists the peak locations and full-width at half maximum for the W 4f, Ca 2p, O 1s, and Ba 3d spectral lines for $BaWO_4$ and Ba_2CaWO_6.

Barium $3d_{5/2}$ binding energies for the following common barium compounds are 779.2 eV for BaO, 779.2 eV for $Ba(OH)_2$, and 779.3 eV for $BaCO_3$ [1]. The Ba $3d_{5/2}$ binding energies for $BaWO_4$ and Ba_2CaWO_6 reported here are 780.0 eV and 779.6 eV, respectively. Since the Ba 3d binding energies shift very little, it would be difficult to distinguish between different barium compounds on the cathode surface. Additionally, W is in the same oxidation state (+6) for both $BaWO_4$ and Ba_2CaWO_6, and therefore, the W 4f binding energy will be similar for both species. It is also important to consider that since Ba and BaO react with the atmosphere, the surface state of the cathode may be different during analysis than it was following cathode operation under vacuum. Special sample preparation is needed to avoid charging during XPS analysis since the barium compounds are insulators. The current test facility does not have the capability to prepare and analyze the cathode surface in situ. These issues make conclusive identification of the barium species along the cathode emitter surface difficult to obtain.

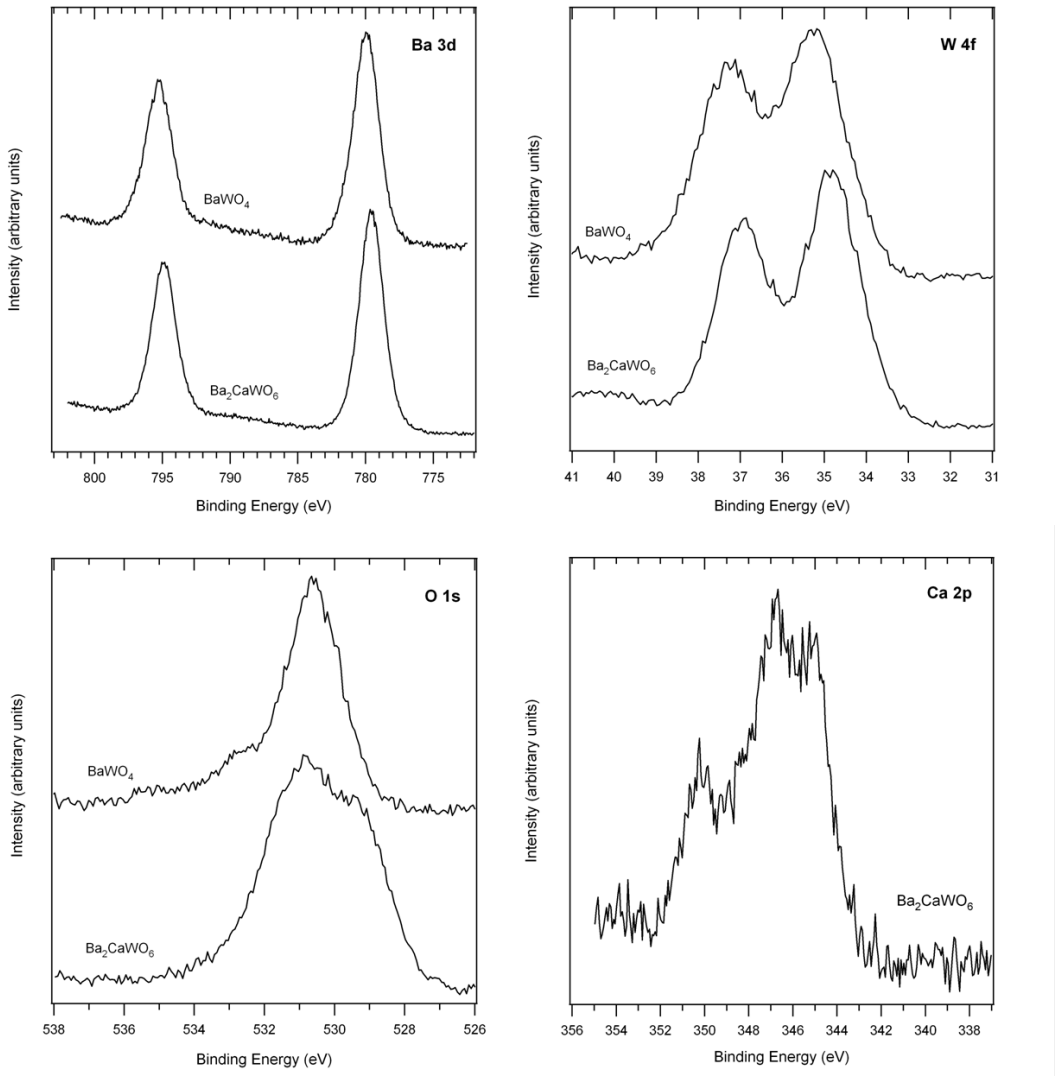

Figure A.0.1: XPS spectra for $BaWO_4$ and Ba_2CaWO_6.

Appendix B

Tungsten Oxide Formation in Cathodes with Excess Oxygen

Volatile tungsten oxide species are formed when a tungsten surface is exposed to oxygen at high temperatures and low pressures [4]. Transport and deposition of these volatile tungsten species have been observed in several extended hollow cathode tests [5–8]. Therefore, the focus of this section is on estimating the desorption rates of the volatile products formed during steady-state gas-solid reactions between tungsten and oxygen at typical cathode pressures and temperatures.

The approach used here is that presented by Batty and Stickney [4]. In their work, they calculate the desorption rates for the oxygen-tungsten system using a quasi-equilibrium approach and achieve good agreement with experimental results published by Schissel and Trulson [9]. The use of equilibrium thermodynamics is preferred over kinetic treatments as it greatly simplifies the analysis and the need to consider detailed kinetic models of the reaction mechanisms [4].

The eight equations considered here for gas-solid reactions between oxygen and tungsten are

$$\mathrm{W\ (s)} + \tfrac{1}{2}\,\mathrm{O_2\ (g)} \rightarrow \mathrm{WO\ (g)}, \tag{B.0.1}$$

$$\mathrm{W\ (s)} + \mathrm{O_2\ (g)} \rightarrow \mathrm{WO_2\ (g)}, \tag{B.0.2}$$

$$\mathrm{W\ (s)} + \tfrac{3}{2}\,\mathrm{O_2\ (g)} \rightarrow \mathrm{WO_3\ (g)}, \tag{B.0.3}$$

$$2\mathrm{W\ (s)} + 3\,\mathrm{O_2\ (g)} \rightarrow \mathrm{W_2O_6\ (g)}, \tag{B.0.4}$$

$$3\mathrm{W\ (s)} + 4\,\mathrm{O_2\ (g)} \rightarrow \mathrm{W_3O_8\ (g)}, \tag{B.0.5}$$

$$3\mathrm{W\ (s)} + \tfrac{9}{2}\,\mathrm{O_2\ (g)} \rightarrow \mathrm{W_3O_9\ (g)}, \tag{B.0.6}$$

$$4\mathrm{W\ (s)} + 6\,\mathrm{O_2\ (g)} \rightarrow \mathrm{W_4O_{12}\ (g)}, \tag{B.0.7}$$

$$\tfrac{1}{2}\,\mathrm{O_2\ (g)} \rightarrow \mathrm{O\ (g)}. \tag{B.0.8}$$

The equilibrium composition is calculated with the equilibrium constant, $K_p(T)$, defined as

$$K_p(T) \equiv \prod_i P_i^{(\nu_i'' - \nu_i')} = \exp[-\sum_i (\nu_i'' - \nu_i')\mu_i^\circ / RT], \tag{B.0.9}$$

where P_i is the partial pressure of species i at equilibrium, ν_i'' is the stoichiometric coefficient of the i^{th} product in the reaction, ν_i' is the stoichiometric coefficient of the i^{th} reactant in the reaction, and μ_i° is the partial chemical potential of species i at some reference state and is given by

$$\mu_i^\circ = [H_i(T) - H_i^\circ + \Delta H_{f_i}] - TS^\circ. \tag{B.0.10}$$

For tungsten oxide formation summarized by

$$x\text{W (s)} + \frac{y}{2}\,\text{O}_2\text{ (g)} \rightarrow \text{W}_x\text{O}_y\text{ (g)}, \tag{B.0.11}$$

the equilibrium constant for any given reaction can be written in terms of the partial pressures as

$$K_{p,W_xO_y} = P_{W_xO_y}\left(P_{O_2}\right)^{-y/2}. \tag{B.0.12}$$

Note that the pressure term for the solid is not included. Applying Eq. (B.0.12) to the reactions given in Eqs. (B.0.1)–(B.0.8) and noting that the total pressure is the sum of the partial pressures, i.e., $P = \sum P_i$, we obtain a set of 9 equations and 9 unknowns. This set of equations can be solved for the partial pressures of the equilibrium mixture given T, P, and K_p.

Consider a thin control volume near the emitter surface. A fraction of the oxygen molecules that leave the control volume and impinge on the surface will adsorb, equilibrate, and then react with the tungsten surface to produce volatile products. The molecules that do not equilibrate are reflected from the surface and return to the control volume. Volatile species formed on the emitter surface will desorb and enter the control volume.

The adsorption rate of species i onto a surface is given by the following equation from kinetic theory:

$$\Gamma_{a_i} = \zeta_i Z_i = \zeta_i P_i \left(2\pi M_i RT\right)^{-1/2}, \tag{B.0.13}$$

where Z_i is the rate at which species i collide with the surface, ζ_i is the fraction of collisions that result in adsorption, Γ_{a_i} is the adsorption rate (i.e., the rate at which molecules are equilibrated), P_i is the partial pressure of species i, and M_i is the molecular weight of species i.

To obtain an upper bound on the desorption rates, we assume that all collisions between oxygen molecules and the emitter surface result in adsorption and that all adsorbates equilibrate with the

surface. The flux of O_2 to the surface is taken to be equal to

$$\Gamma_{a,_{O_2}} = \frac{n_{O_2}\bar{c}_{O_2}}{4} = \frac{n_{O_2}}{4}\left(\frac{8kT}{\pi m_{O_2}}\right)^{1/2}, \tag{B.0.14}$$

where the oxygen number density is taken to be some fraction of the xenon neutral gas density and the gas temperature is assumed to be in thermal equilibrium with the emitter surface.

If we assume steady-state, then conservation of oxygen atoms yields the following equation in which the flux of oxygen atoms leaving the control volume must equal the flux of oxygen atoms entering the control volume:

$$\begin{aligned} 2\zeta_{O_2}\Gamma_{a,_{O_2}} = \sum_i y_i\Gamma_{d_i} &= \Gamma_{d,_O} + 2\Gamma_{d,_{O_2}} + \Gamma_{d,_{WO}} + 2\Gamma_{d,_{WO_2}} + 3\Gamma_{d,_{WO_3}} \\ &+ 6\Gamma_{d,_{W_2O_6}} + 8\Gamma_{d,_{W_3O_8}} + 9\Gamma_{d,_{W_3O_9}} + 12\Gamma_{d,_{W4O_{12}}}. \end{aligned} \tag{B.0.15}$$

Under steady-state conditions, adsorption is balanced by desorption so that

$$\Gamma_{d_i} = \Gamma_{a_i} = \zeta_i Z_i = \zeta_i P_i \left(2\pi M_i RT\right)^{-1/2}. \tag{B.0.16}$$

The equilibrium constant is calculated using Eq. (B.0.9) and thermodynamic data from the JANAF tables [10] for each of the eight reactions given in Eqs. (B.0.1)–(B.0.8). Equation (B.0.12) is then solved for the partial pressure of each species in terms of P_{O_2}. These expressions are combined with Eqs. (B.0.15) and (B.0.16) to determine P_{O_2}. Once P_{O_2} is known, then the partial pressures and desorption fluxes of all other species are calculated.

The desorption fluxes of each of the tungsten oxide species are given in Fig. B.0.1 for oxygen concentrations of 1 and 100 ppm and temperatures ranging between 1000 and 2000 K. The main evaporants at typical cathode surface temperatures between 1200 and 1400 K include O_2, W_2O_6, W_3O_8, and W_3O_9. However, the desorption rates of these species are at least three orders of magnitude lower than the barium supply flux from the emitter. As a result, the concentration of tungsten oxide species in the xenon discharge may be even smaller than those of Ba, BaO, and O_2.

In order to understand the transport of tungsten oxides in the cathode, the approach outlined in Chapter 3 could be implemented for these species. The ionization potentials for W_2O_6 and W_3O_9 are 12.2 and 12.0 eV, respectively [11]. These values are close to the ionization potential for xenon, and therefore, charge exchange processes may be important.

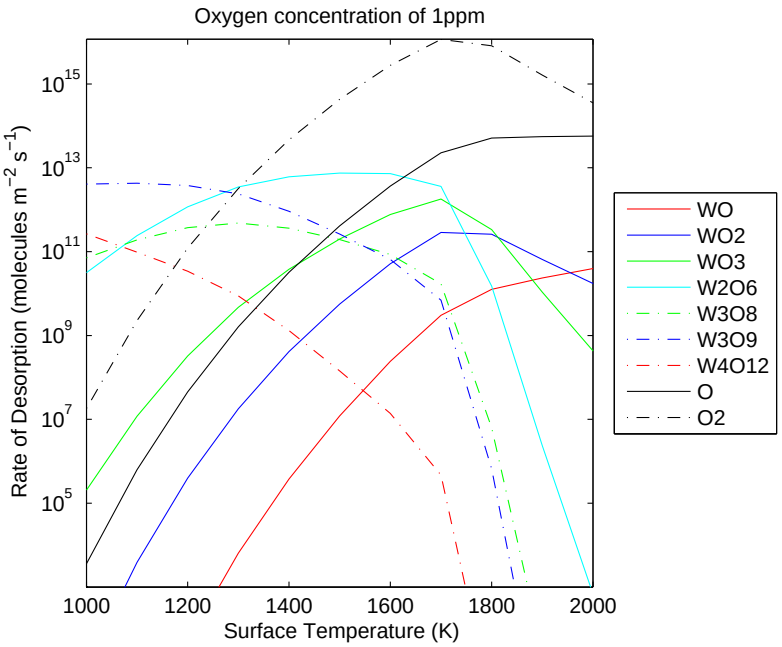

(a) The desorption of O_2, W_2O_6, W_3O_8, and W_3O_9 dominate between 1200 and 1400 K at an oxygen concentration of 1 ppm.

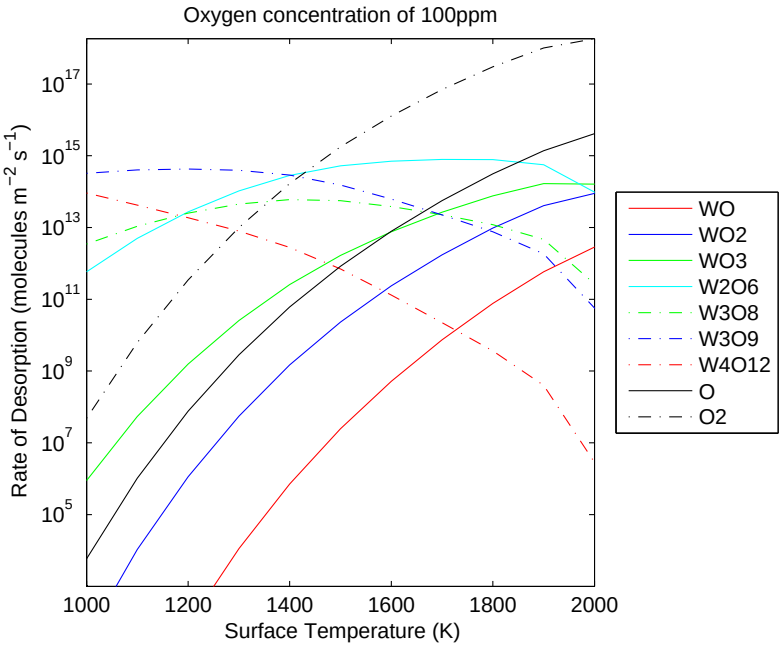

(b) The desorption of O_2, W_2O_6, W_3O_8, and W_3O_9 dominate between 1200 and 1400 K at an oxygen concentration of 1 ppm.

Figure B.0.1: Desorption rates of volatile tungsten oxide species.

Appendix C

Oxygen Flow System

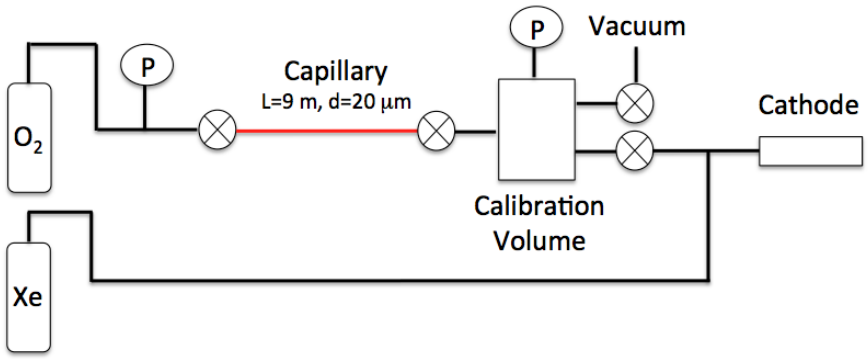

Figure C.0.1: Oxygen flow system.

The challenge of the oxygen flow system is that a very small amount of oxygen must be injected into the cathode at volumetric flow rates on the order of 10^{-4} standard cm^3/min. In order to accurately determine the oxygen flow rate into the cathode, the flow system shown in Fig. C.0.1 is employed. Oxygen flows through a fused silica capillary tube and into a calibration volume. The capillary is 9 m in length and 20 μm in diameter. The pressure upstream of the capillary can be varied, and the rate of pressure rise in the calibration volume is measured. From the ideal gas law assuming standard temperature:

$$PV|_1 = PV|_2, \tag{C.0.1}$$

where the subscript 1 refers to the conditions upstream of the calibration volume where the pressure and flow rate are constant, and 2 refers to the conditions in the calibration volume at standard temperature and pressure. After taking the time derivative of each side we obtain the standard volumetric flow rate:

$$\frac{dV_1}{dt} = \frac{V_2}{P_1}\frac{dP_2}{dt}, \tag{C.0.2}$$

where V_2 represents the calibration volume and is equal to 16 cm^3, P_1 is equal to the standard pressure of 1 atm, and dP_2/dt is the rate of pressure rise in the calibration volume. The flow rate, which is given in standard cubic centimeters per min (sccm), is the volumetric flow rate corrected to standard temperature and pressure. This parameter is equivalent to a molar flow rate, and therefore, we can determine the concentration of oxygen in the xenon flow by taking the ratio of the standard volumetric flow rates of oxygen and xenon. The oxygen concentration is adjusted by varying the pressure upstream of the capillary.

The flow rate is measured prior to each oxygen poisoning event via the process described above. The calibration volume is then evacuated by opening the valve to the vacuum chamber. At the start of poisoning, the vacuum valve is closed and the valve to the cathode is opened. At this time, some xenon is diverted away from the cathode and flows into the calibration volume because of the low pressure there. The oxygen must then diffuse through the stagnant xenon gas in order to reach the cathode. The characteristic time for diffusion of O_2 through Xe can be approximated as

$$\tau \sim \frac{L^2}{\pi^2 D}, \tag{C.0.3}$$

where L is the distance the oxygen must diffuse through the stagnant xenon gas to reach the cathode feedline and D is the diffusion coefficient given by

$$D = \frac{kT}{\mu\nu}, \tag{C.0.4}$$

where μ is the reduced mass and ν is the collision frequency given by reaction (15) in Table 3.1. For $T = 300$ K and a xenon pressure of 1 Torr, the time constant for diffusion of oxygen through the xenon is approximately 45 s.

Bibliography

[1] R. Vasquez, "X-ray photoelectron spectroscopy study of Sr and Ba compounds," *J. Elec. Spec. and Rel. Phen.*, vol. 50, pp. 217–240, 1991.

[2] J. Watts and J. Wolstenholme, *An Introduction to Surface Analysis by XPS and AES.* Wiley, 2003.

[3] R. Smart, S. McIntyre, M. Bancroft, and I. Bello, "X-ray photoelectron spectroscopy," Department of Physics and Materials Science, City University of Hong Kong, Surface ScienceWestern, UWO.

[4] J. Batty and R. Stickney, "Quasiequilibrium treatment of gas-solid reactions. I. Evaporation rates of volatile species formed in the reaction of O_2 with W, Mo, and C*," *J. Chem. Phys.*, vol. 51, no. 10, pp. 4475–4484, 1969.

[5] T. Verhey, "Microanalysis of extended-test xenon hollow cathodes," in *27th AIAA Joint Propulsion Conference*, Sacramento, CA, 1991, AIAA-91-2123.

[6] J. Polk, J. Anderson, J. Brophy, V. Rawlin, M. Patterson, and J. Sovey, "The results of an 8200 hour wear test of the NSTAR ion thruster," in *35th AIAA Joint Propulsion Conference*, Los Angeles, CA, 1999, AIAA-99-2446.

[7] A. Sengupta, "Destructive physical analysis of hollow cathodes from the Deep Space 1 flight spare ion engine 30,000 hr life test," in *29th International Electric Propulsion Conference*, Princeton, NJ, 2005, IEPC-2005-026.

[8] T. Sarver-Verhey, "Destructive evaluation of a xenon hollow cathode after a 28,000 hour life test," in *34rd AIAA Joint Propulsion Conference*, Cleveland, OH, 1998, AIAA-98-3482.

[9] P. Schissel and O. Trulson, "Mass-spectrometric study of the oxidation of tungsten," *J. Chem. Phys.*, vol. 43, no. 2, pp. 737–743, 1965.

[10] M. Chase, "JANAF thermochemical tables, 3rd ed." American Chemical Society, 1986.

[11] "NIST chemistry webbook," 2011, retrieved Jan 2012. [Online]. Available: http://webbook.nist.gov/chemistry